Sensitivity Enhancement of Optomechanical Measurements using Squeezed Light

Dissertation
zur Erlangung des Doktorgrades
an der Fakultät für Mathematik, Informatik und Naturwissenschaften
Fachbereich Physik
der Universität Hamburg

vorgelegt von
Lisa Marie Kleybolte

Hamburg

2019

Gutachter der Dissertation:	Prof. Dr. Roman Schnabel Prof. Dr. Henning Moritz
Zusammensetzung der Prüfungskomission:	Prof. Dr. Roman Schnabel Prof. Dr. Henning Moritz Prof. Dr. Oliver Gerberding Prof. Dr. Daniela Pfannkuche Prof. Dr. Ludwig Mathey
Vorsitzende der Prüfungskomission:	Prof. Dr. Daniela Pfannkuche
Vorsitzender des Fach-Promotionsausschusses PHYSIK:	Prof. Dr. Michael Potthoff
Leiter des Fachbereichs PHYSIK:	Prof. Dr. Wolfgang Hansen
Dekan der Fakultät MIN:	Prof. Dr. Heinrich Graener

Abstract

The quantum mechanical description of electromagnetic fields predicts fluctuations in their amplitude and phase quadrature, that underlay Heisenberg's uncertainty relation. When reflected by an object, the fields induce a radiation pressure force. The amplitude uncertainty causes fluctuations of this force, resulting in quantum radiation pressure noise. The standard quantum limit sets a lower bound for the sum of radiation pressure noise and shot noise, that will dominate the sensitivity of future gravitational-wave detectors. In optomechanics the radiation pressure noise is investigated. One fundamental goal is to undercut the standard quantum limit by applying squeezed states, that have a reduced variance in one quadrature and an amplified variance in the orthogonal. A shot noise reduction of 2.2 dB in an optomechanical table top experiment can be found in the literature.

In this work squeezed states were produced in a nonlinear crystal via degenerate parametric down-conversion. At a sideband frequency of 400 kHz a squeeze factor of (-8.7 ± 0.2) dB was measured. In a first experiment the setup was used to demonstrate how internal squeezing can improve the sensitivity of an interferometric measurement. An increase of the sensitivity-bandwidth product of 36 % was experimentally observed for an artificially generated signal.

This thesis further presents a cryogenic optomechanical experiment with a silicon nitride membrane as mechanical oscillator. The topology of a Michelson-Sagnac interferometer was chosen to realize a Michelson interferometer with the membrane as end mirror despite its low reflectivity. A contrast of the outcoming modes of 99.7 % was reached for temperatures down to 100 K. The signal at the dark fringe allowed a measurement with a shot-noise limited sensitivity for an input power of 50 μW.

After calibrating the measured spectra with the theoretical shot noise, the quality factors of the membrane $Q_{293} \approx 2.7 \cdot 10^5$ and $Q_{100} \approx 1.5 \cdot 10^6$ at 293 K and 100 K could be determined from the resulting displacement spectral density. By injecting externally produced squeezed states, the quantum shot noise in the presented experiment was reduced by (3.1 ± 0.2) dB, which corresponds to a factor of $\sqrt{2}$ in the linear displacement spectral density. For a radiation-pressure-noise limited sensitivity, the demonstrated application of squeezed states could allow to overcome the standard quantum limit in the future.

Kurzfassung

Aus der quantenmechanischen Beschreibung elektromagnetischer Felder folgen Fluktuationen in deren Amplituden- und Phasenquadratur, die der Heisenbergsche Unschärferelation unterliegen. Wenn die Felder von einem Objekt reflektiert werden, erzeugen sie eine Strahlungsdruckkraft. Die Fluktuationen dieser Kraft aufgrund der Amplitudenunschärfe verursachen das Quanten-Strahlungsdruckrauschen. Das Standardquantenlimit ist der Minimalwert für die Summe aus Strahlungsdruckrauschen und Schrotrauschen, der in Zukunft die Sensitivität von Gravitationswellendetektoren limitieren wird. In der Optomechanik wird das Strahlungsdruckrauschen erforscht. Ein fundamentales Ziel ist das Überwinden des Standardquantenlimits durch die Anwendung gequetschter Zustände, deren Varianz in einer Quadratur vermindert aber in der orthogonalen erhöht ist. In der Literatur findet man eine Schrotrauschreduktion von 2.2 dB in einem optomechanischem Tischaufbau.

In dieser Arbeit wurden gequetschte Zustände mithilfe der parametrischen Abkonversion in einem nichtlinearen Kristall generiert. Bei einer Seitenbandfrequenz von 400 kHz wurde ein Quetschfaktor von (-8.7 ± 0.2) dB gemessen. In einem ersten Experiment mit dem Aufbau wurde demonstriert, wie intern produzierte gequetschte Zustände die Sensitivität einer interferometrischen Messung verbessern können. Ein Anstieg des Sensitivität-Bandbreite-Produkts von 36 % wurde für ein künstlich generiertes Signal experimentell beobachtet.

Es wird weiterhin ein kryogenes optomechanisches Experiment mit einer Siliziumnitrid-Membran als mechanischer Oszillator präsentiert. Die Topologie des Michelson-Sagnac-Interferometers wurde gewählt um trotz ihrer geringen Reflektivität ein Michelson-Interferometer mit der Membran als Endspiegel zu realisieren. Für Temperaturen bis minimal 100 K konnte ein Kontrast der Moden im Ausgang von 99.7 % erreicht werden. Das Signal im dunklen Ausgang ermöglichte eine Messung mit einer vom Schrotrauschen limitierten Sensitivität für eine Eingangsleistung von 50 μW.

Nach der Kalibrierung der gemessenen Spektren mit dem theoretischen Schrotrauschen konnten die Gütefaktoren der Membran $Q_{293} \approx 2.7 \cdot 10^5$ und $Q_{100} \approx 1.5 \cdot 10^6$ bei 293 K und 100 K aus der resultierenden spektrale Dichte der Ortsänderung bestimmt werden. Durch die Injektion extern produzierter gequetschter Zustände wurde das Quantenschrotrauschen im präsentierten Experiment um (3.1 ± 0.2) dB gesenkt, was einem Faktor $\sqrt{2}$ in der linearen spektralen Rauschdichte entspricht. Für eine vom Strahlungsdruckrauschen limitierte Sensitivität könnte die demonstrierte Anwendung von gequetschten Zuständen in Zukunft eine Unterschreitung des Standardquantenlimits ermöglichen.

Contents

1 Introduction

Optomechanical coupling: The subject of optomechanics investigates the coupling between electromagnetic fields and mechanical oscillators due to the impulse transfer of photons. The quantization of light into photons was stated the first time by Albert Einstein in his explanation for the photoelectric effect [1]. Each photon of a light field with the frequency $\omega = 2\pi f$ has an energy of $E = \hbar\omega$ and a momentum $p = \hbar\frac{\omega}{c}$ with the reduced Planck's constant $\hbar$ [2] and the speed of light c. Because of the high speed of light, the impulse of a single photon usually does not affect a macroscopic mass in a measurable order of magnitude. However, for a high-power light beam with a power P the sum of photons produces an average force of $F = \frac{2P}{c}$ on a retro-reflecting mirror. Already Peter Lebedew stated in 1901 that the sunlight induces a pressure of 0.4 mg on a black surface of 1 m^2 or a pressure of 0.8 mg on a mirror of the same size. He presented the first experimental observation of an optomechanical force with a radiometer [3].

The described coupling causes two effects in optomechanical systems. The first is the dynamical radiation pressure force in optical cavities [4]. The force of the light on an end mirror of a cavity causes a displacement, which then influences the power of the light. The power variations result again in a change of the force. It occurs a coupling between the optical and mechanical degrees of freedom [5]. Such coupling allows for example the cooling of macroscopic objects to their ground state as demonstrated in [6]. The second effect is called *radiation pressure noise*. The phase's and amplitude's uncertainty of an electromagnetic field underlay Heisenberg's uncertainty relation [7]. The product of the variances of the corresponding operators of these observables can not go below a certain limit. Hence the precision of measuring both of them is finite. The *quantum shot noise* is caused by the phase uncertainty of the electromagnetic field and occurs during the detection of the light field on a photoelectric detector due to the fact, that the photons are uncorrelated. Therefore it is also called *photon counting noise*. The quantum radiation pressure noise is caused by the amplitude uncertainty and occurs when the electromagnetic field is reflected by movable objects. Due to the fluctuations of the acting force exerted by the photons, the deflection of the object varies, which causes a phase modulation [8]. Even for strong light fields, the optomechanical coupling is so small, that it only needs to be considered in the cases of low masses and high precision experiments.

Quantum radiation pressure noise in gravitational-wave detectors: The described effects are relevant for interferometric measurements, in particular for the detection of gravitational waves [9]. The existence of gravitational waves is a consequence of Albert Einstein's general relativity theory [10]. Gravitational-wave detectors as GEO600 [11], LIGO [12] and VIRGO [13] base on the concept of a Michelson interferometer to detect small changes in the arm lengths caused by disturbances in the curvature of space time. In the updated detectors as advanced LIGO the classical noise sources as seismic noise, technical laser noise and thermal noise will be reduced to such a low level, that the sensitivity in a broad frequency range in the audioband will be limited by the quantum noise [14][15], the sum of the shot noise and the radiation pressure noise. For advanced LIGO the radiation pressure noise will limit the sensitivity in the frequency range of 10 to 40 Hz [16].

The input power in an interferometer determines the ratio between shot noise and radiation pressure noise. By increasing the optical input power of an interferometer, the phase fluctuations can be decreased, however the amplitude fluctuations get enhanced. As a consequence there exists a frequency dependent optimum power to reach the minimum quantum noise in interferometric measurements. The resulting limitation of the sensitivity is called the *standard quantum limit*.

The application of squeezed Light: An alternative to a light power variation to enhance the sensitivity of gravitational-wave detectors is the application of nonclassical states. The fluctuations of a state in one quadrature can be lower than the fluctuations of a vacuum state as long as the fluctuations in the orthogonal quadrature are magnified such, that Heisenberg's uncertainty relation is still fulfilled [17]. These states are called *squeezed states*. They were observed the first time in 1985 [18] with a squeeze factor of 0.3 dB. Over the years the techniques for the generation and detection of squeezed light improved. The current record value for the squeeze factor of 15 dB was measured in 2016 [19].

The application of squeezed states to improve the sensitivity of interferometric measurements as for gravitational-wave detection has been theoretically regarded by Caves [20]. In this approach the states are produced by an external source and injected

through the output of the interferometer. This technique has been successfully applied in current gravitational-wave detectors. The enhancement of the sensitivity with squeezed states in GEO600 is described in [21]. The implementation of a squeezed-light source in LIGO resulted in the best broadband sensitivity to gravitational waves up to this point [22]. Alternative concepts using nonclassical states to improve the sensitivity of interferometric measurements with cavities are taking advantage of the white-light-cavity effect [23] or the internal production of squeezed states [24].

The Michelson-Sagnac interferometer as optomechanical experiment: Due to their scaling, gravitational-wave detectors are not suitable for in depth investigations of the radiation pressure. Therefore the field of optomechanics covers the fundamental research of the coupling between electromagnetic fields and mechanical oscillators. The first experiments by Braginsky, who measured the damping of an oscillator using microwave radiation [9], were followed by a variety of approaches using different mechanical oscillators as microtoroids [25], cantilevers [26], optomechanical crystals [27] or thin membranes [28][29][30]. Unlike the heavy masses of the optics in gravitational-wave detectors, these lighter devices with a wide range of mechanical quality factors and resonance frequencies provide the opportunity to operate interferometric experiments on a small scale. The experiences and results from the investigation of such optomechanical systems will allow to improve the measurement sensitivity of future gravitational-wave detectors further.

In this work an optomechanical experiment with the long term goal, to reach and overcome the mentioned standard quantum limit, is presented. Therefore initially a radiation-pressure-noise limited sensitivity of an interferometric measurement needs to be achieved. In [31] the Michelson-Sagnac Interferometer is proposed as a possible setup to reach the radiation pressure noise for an input power of 1 W at a temperature of 1 K. The principle bases on a Michelson interferometer whose arms are folded such, that they are reflected by the same end mirror from the two opposite sides. In this case a silicon nitride membrane is used as this end mirror of the interferometer, serving as mechanical oscillator. Due to its low reflectivity, a high percentage of the light is transmitted in both directions and forms a Sagnac mode at the output. Because of their high quality factors and low masses such membranes are good candidates to measure radiation pressure.

As in gravitational-wave detectors, also in optomechanics the application of squeezed states can improve the measurement's sensitivity. Recently the reduction of quantum shot noise by 2.2 dB with squeezed states has been demonstrated in a table top experiment with an optomechanical magnetometer [32]. Injecting squeezed states into the proposed Michelson-Sagnac interferometer, as done in this work, can improve the radiation-pressure-noise limited sensitivity in the future even further, which forms a crucial step towards beating the standard quantum limit for a broad frequency range.

Thesis structure: The main focus of the presented work is the optimization of an optomechanical table top experiment with a silicon nitride membrane as a mechanical oscillator. The chosen topology is a Michelson-Sagnac interferometer. To achieve a quantum-noise limited sensitivity, classical noise sources as thermal and laser amplitude noise must be suppressed. Therefore the laser noise was investigated and the setup was designed for low temperatures and cooled down with a cryostat.

The squeezed light for the experiment was generated via the process of degenerate parametric down-conversion in a nonlinear crystal and measured with a balanced homodyne detector. The source was built up, characterized and the produced states were injected into the interferometer to enhance the sensitivity by reducing the quantum shot noise.

The injection of externally produced squeezed states is not the only approach to use non classical states to enhance an interferometer's sensitivity. This thesis contains an excursus describing the demonstration of a different concept: The generation of squeezed states directly inside the resonator of an interferometer. Using this technique, the sensitivity-bandwidth product can be improved [24][33].

This thesis is structured as follows:

- **Chapter 2** covers the fundamental theoretical concepts of optomechanics and quantumoptics.

- In **chapter 3** the silicon nitride membrane as mechanical oscillator is regarded and the topology of the Michelson-Sagnac interferometer is introduced. An overview of the noise sources in the setup is given.

- The experimental production of non classical states is described in **chapter 4**. The nonlinear processes for the generation and the homodyne detector scheme for the measurement of squeezed light are explained, as well as the specific setup used in this work.

- **Chapter 5** presents the approach to use internally produced squeezed states to improve the sensitivity of cavity-enhanced interferometric measurements. The squeezed-light source was modified to demonstrate this alternative idea in contrast to injecting externally produced states.

- In **chapter 6** the experimental realization of the Michelson-Sagnac interferometer is described, including the challenges to build the setup for low temperatures, to achieve a high contrast of the outcoming modes and to implement the squeezed-light source.

- The performance of the experiment is presented in **chapter 7**. The executed measurements include the characterization of the silicon nitride membrane as mechanical oscillator, the detection of the squeezed states by the built source and the enhancement of the interferometer's sensitivity by injecting these states.

- **Chapter 8** shows the future improvements of the experiment, that will allow to reach the radiation pressure noise and the standard quantum limit. Besides some general upgrades, the setup of an active laser amplitude stabilization and the implementation of a signal recycling mirror is planned.

2 Theoretical Concepts of Optomechanics and Quantum Optics

The presented experimental work mainly consists of two parts. The first one is an interferometer with a harmonic oscillator to investigate its mechanical interaction with the electromagnetic field. The second one is a squeezed-light source to produce non-classical states that are used afterward to enhance the sensitivity of this interferometer. Hence this chapter describes the fundamental theoretical concepts of optomechanics and quantum optics [34] [35] [8] [17].

2.1 The Spectral Density

To analyze an observable x, it can be examined in the time domain $x(t)$ or in the frequency domain $x(\Omega)$. Under the condition that a function is square-integrable, the Fourier transformation

$$x(\Omega) = \int_{-\infty}^{\infty} x(t) e^{-i\Omega t}\, dt \tag{2.1}$$

is used for the transition from one description to the other. As the later presented measurements all result from random processes, the observables can not be written as an analytical function of t or Ω, but can only be described with probabilities p_i for a certain measurement outcome x_i. Therefore the expectation value of the measurement

$$\langle x(t) \rangle = \sum p_i x_i \tag{2.2}$$

is used. Its auto-correlation function

$$S_x(t, \tau) = \langle x(t) x(t+\tau) \rangle \ , \tag{2.3}$$

expresses how the measurement of x at time t is correlated to a copy of itself at time $t + \tau$. The corresponding Fourier transformation

$$S_x(\Omega) = \int_{-\infty}^{\infty} \langle x(t) x(t+\tau) \rangle\, e^{-i\Omega t}\, dt \tag{2.4}$$

is called the *spectral density*. As equation (2.4) is symmetric in such way that $|S_x(\Omega)|^2 = |S_x(-\Omega)|^2$, it is often more convenient to only consider positive frequencies. A factor of 2 is necessary for the scaling of this so called *single-sided spectral density*. Then the

back transformation with $S_x(t,0) = \Delta^2 x$ yields to

$$\left\langle x^2 \right\rangle = \int_0^\infty \frac{2}{2\pi} S_x^{\mathrm{ss}}(\Omega)\, d\Omega \ . \tag{2.5}$$

2.2 The Mechanical Oscillator

2.2.1 The Harmonic Oscillator Transfer Function

The starting point to describe a harmonic oscillator is Newton's second law for a position dependent storing force $F_{\mathrm{spring}} = -\kappa x(t)$ with the equation of movement $x(t)$ induced by an external force F_{ext} and a spring constant κ. The movement is damped by a force $F_{\mathrm{damp}}(x(t), \dot{x}(t))$. It applies

$$m\frac{d^2}{dt^2}x(t) + F_{\mathrm{damp}}(x(t), \dot{x}(t)) + \kappa x(t) = F_{\mathrm{ext}} \ . \tag{2.6}$$

In [35] it is shown how to solve the latter equation using Fourier transformation. When multiplied with $e^{-i\Omega}t$ and integrated from $t = -\infty$ to $t = \infty$, the differential equation (2.6) transforms to

$$\int_{-\infty}^{\infty} e^{-i\Omega t} \left(m\frac{d^2}{dt^2}x(t) + F_{\mathrm{damp}}(x(t), \dot{x}(t)) + m\Omega_0^2 x(t) \right)\, dt = \int_{-\infty}^{\infty} e^{-i\Omega t} F_{\mathrm{ext}}(t)\, dt \tag{2.7}$$

with the resonance frequency $\Omega_0^2 = \frac{\kappa}{m}$. Under the condition that $x(t = \pm\infty) = 0$, the Fourier transformation can be written as:

$$\dot{x}(\Omega) = \int_{-\infty}^{\infty} e^{-i\Omega t} \frac{d}{dt} x(t)\, dt \tag{2.8}$$

$$= \underbrace{[e^{-i\Omega t} x(t)]_{-\infty}^{\infty}}_{=0} - (-i\Omega) \underbrace{\int_{-\infty}^{\infty} e^{-i\Omega} x(t)\, dt}_{x(\Omega)} \ . \tag{2.9}$$

Inserting $(\frac{d}{d\Omega})^n x(\Omega) = (i\Omega)^n x(\Omega)$ in equation (2.6) leads to:

$$\left[-m\Omega^2 + i\frac{F_{\mathrm{damp}}(x(\Omega), \dot{x}(\Omega))}{i x(\Omega)} + m\Omega_0^2 \right] x(\Omega) = F_{\mathrm{ext}}(\Omega) \ . \tag{2.10}$$

To receive a solution for $x(\Omega)$ it is defined that:

$$\kappa_{\mathrm{damp}}(x(\Omega), \dot{x}(\Omega)) = \frac{F_{\mathrm{damp}}(x(\Omega), \dot{x}(\Omega))}{i x(\Omega)} \ . \tag{2.11}$$

It follows:

$$x(\Omega) = \left[\frac{1}{m\Omega_0^2} \frac{1 - \frac{\Omega^2}{\Omega_0^2} - i\frac{\kappa_{\text{damp}}}{m\Omega_0^2}}{(1 - \frac{\Omega^2}{\Omega_0^2})^2 + (\frac{\kappa_{\text{damp}}}{m\Omega_0^2})^2} \right] F_{\text{ext}}(\Omega) \tag{2.12}$$

$$= H(\Omega) F_{\text{ext}}(\Omega) \ . \tag{2.13}$$

Here $H(\Omega)$ stands for the complex oscillator transfer function with $\arg[H(\Omega)] = \phi(\Omega)$ describing the phase difference between the excitation of the oscillator and its reaction.

Assuming that $\kappa_{\text{damp}} \neq 0$, there are two damping mechanisms to consider. The viscous damping is caused by residual gas in the surrounding of the oscillator and therefore dependent on the velocity $\dot{x}(t)$ [36]. In this case the damping force is:

$$F_{\text{damp,vis}} = -\gamma m \dot{x}(t) \tag{2.14}$$

with the damping coefficient γ. It applies $\kappa_{\text{damp}}(\Omega) = \gamma m \Omega$. The internal losses of the oscillator cause the second damping mechanism, the structural damping. One assumes a repulsively acting internal force

$$F_{\text{damp,str}} = -\kappa(1 + i\phi(\Omega))x(\Omega) \ . \tag{2.15}$$

According to [37] the function $\phi(\Omega)$ is approximately flat for a large range of frequencies, hence for simplicity it is assumed to be constant.

2.2.2 The Mechanical Quality Factor

The energy dissipation of a mechanical oscillator is quantified with the quality factor Q. It determines the time t, that the energy of an oscillator needs to drop down to a fraction of $1/e$ of the initial energy value E_0:

$$E(t) = E_0 e^{-\frac{\Omega_0 t}{Q}} \ . \tag{2.16}$$

For the viscous and structural damping, the quality factors Q_{vis} and Q_{str} are given by:

$$Q_{\text{vis}} = \frac{\Omega_0}{\gamma} \ , \tag{2.17}$$

$$Q_{\text{str}} = \frac{1}{\phi} \ . \tag{2.18}$$

For the harmonic oscillator these yield to the corresponding transfer functions:

$$H_{\mathrm{vis}} = \frac{1}{m\Omega_0^2} \frac{1}{(1-\frac{\Omega^2}{\Omega_0^2}) + i\frac{1}{Q_{\mathrm{vis}}}\frac{\Omega}{\Omega_0}} \ , \tag{2.19}$$

$$H_{\mathrm{str}} = \frac{1}{m\Omega_0^2} \frac{1}{(1-\frac{\Omega^2}{\Omega_0^2}) + i\frac{1}{Q_{\mathrm{str}}}} \tag{2.20}$$

with the real parts

$$\Re H_{\mathrm{vis}} = \frac{1}{m\Omega_0^2} \frac{1}{\sqrt{(1-\frac{\Omega^2}{\Omega_0^2})^2 + (\frac{1}{Q_{\mathrm{vis}}}\frac{\Omega}{\Omega_0})^2}} \ , \tag{2.21}$$

$$\Re H_{\mathrm{str}} = \frac{1}{m\Omega_0^2} \frac{1}{\sqrt{(1-\frac{\Omega^2}{\Omega_0^2})^2 + (\frac{1}{Q_{\mathrm{str}}})^2}} \ . \tag{2.22}$$

In the case of several damping mechanisms acting on the oscillator, the sources add up and it applies:

$$\frac{1}{Q_{\mathrm{total}}} = \sum_i \frac{1}{Q_i} \ . \tag{2.23}$$

An alternative definition of the mechanical quality factor is [37]:

$$Q = \frac{|H(\Omega_0)|}{|H(0)|} \tag{2.24}$$

$$= \frac{\Omega_0}{\Delta\Omega} \tag{2.25}$$

with $\Delta\Omega = 2\pi \cdot \mathrm{FWHM}$ being the angular full width half maximum width. Its value and therefore also the quality factor can be determined from an oscillator's transfer function as it is illustrated in figure 2.1.

2.3 Fundamentals in Quantum Optics

2.3.1 The Quantization of the Electrical Field

In the experimental part of this framework the quantum noise of interferometric measurements is investigated. To explain its cause the quantum mechanical character of electromagnetic fields needs to be considered. The expressions for a single mode field with frequency ω in a standing wave cavity propagating in z- and polarized in x

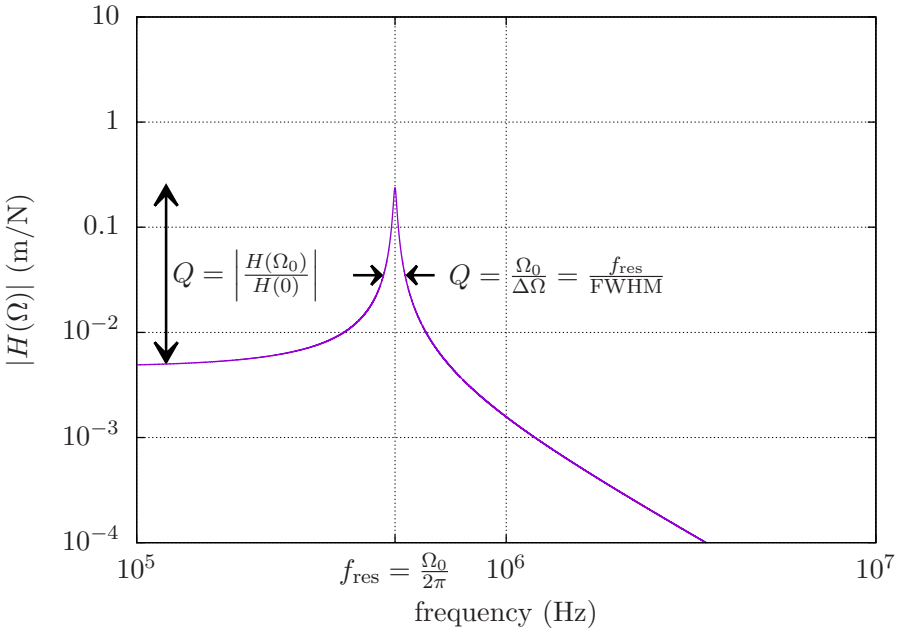

Figure 2.1: Transfer function of a harmonic oscillator: The used parameters in this theoretical curve illustrating equation (2.21) are a quality factor of $Q = 50$, a mass of $m = 20\,\mathrm{ng}$ and a resonance frequency of $f_{\mathrm{res}} = 500\,\mathrm{kHz}$. The quality factor given by the relation in equation (2.25) can be determined as the ratio between the peak height and the initial value or between the resonance frequency $f_{\mathrm{res}} = \frac{\Omega_0}{2\pi}$ and the full width half maximum $\mathrm{FWHM} = \frac{\Delta\Omega}{2\pi}$.

direction follow directly from the Maxwell equations. The electrical field is

$$E_x(z,t) = \sqrt{\frac{2\omega^2}{V\epsilon_0}} q(t) \sin(kz) \tag{2.26}$$

and the magnetic field is

$$B_y(z,t) = \frac{\mu_0\epsilon_0}{k} \sqrt{\frac{2\omega^2}{V\epsilon_0}} p(t) \cos(kz) \tag{2.27}$$

with ϵ_0 being the vacuum permittivity, μ_0 being the vacuum permeability, V being the effective quantization volume and k being the wave number. The variable $q(t)$ describes the canonical position and its derivative $p(t) = \dot{q}(t)$ the momentum. Replacing the operators $\hat{E}$ and $\hat{B}$ by the operator equivalents $\hat{q}$ and $\hat{p}$, the Hamiltonian becomes

$$\hat{H} = \frac{1}{2}(\hat{p}^2 + \omega^2\hat{q}^2) \ . \tag{2.28}$$

In the next step, the non Hermitian *annihilation operator* $\hat{a}$ and *creation operator* $\hat{a}^\dagger$ are introduced, such that

$$\hat{a}_\omega = \frac{1}{\sqrt{2\hbar\omega}}(\omega\hat{q} + i\hat{p}) \ , \tag{2.29}$$

$$\hat{a}^\dagger_\omega = \frac{1}{\sqrt{2\hbar\omega}}(\omega\hat{q} - i\hat{p}) \tag{2.30}$$

with

$$[\hat{a}_\omega, \hat{a}^\dagger_\omega] = 1 \tag{2.31}$$

with the reduced Planck's constant $\hbar$. Applied on the state of an electromagnetic field, the annihilation operator lowers the photon number by one, the creation operator increases it by one. The Hamiltonian then transforms to

$$\hat{H} = \hbar\omega(\hat{a}^\dagger_\omega\hat{a}_\omega + \frac{1}{2}) = \hbar\omega(\hat{n} + \frac{1}{2}) \tag{2.32}$$

with photon number operator

$$\hat{n} = \hat{a}^\dagger_\omega\hat{a}_\omega \ . \tag{2.33}$$

By applying the operator $\hat{a}_\omega^\dagger$ on the ground state $|0\rangle$ repeatedly, any state $|n\rangle$ can be created. The such created states are called *Fock states* [38]:

$$|n\rangle = \frac{(\hat{a}_\omega^\dagger)^n}{\sqrt{n!}} |0\rangle \ . \tag{2.34}$$

2.3.2 Quantum Fluctuations

The fluctuations of an electric field are described by its variance

$$\Delta E_x^2 = \left\langle \Delta^2 \hat{E}_x(z,t) \right\rangle \tag{2.35}$$

$$= \left\langle \hat{E}_x^2(z,t) \right\rangle - \left\langle \hat{E}_x(z,t) \right\rangle^2 . \tag{2.36}$$

For a Fock state $|n\rangle$ this results in:

$$\Delta E_x^2 = \sqrt{2} E_0 \sin(kz) \sqrt{n + \frac{1}{2}} \tag{2.37}$$

with the amplitude of the electric field E_0. From equation (2.37) follows that even for a vacuum state with $n = 0$, it applies $\Delta E_x^2 > 0$. These fluctuations are called the *vacuum fluctuations* [39][17].

2.3.3 The Definition of the Quadrature Operators

With the previously introduced annihilation and creation operators the quadrature operators for an electromagnetic field with frequency ω are defined as:

$$\hat{X}_\omega = \frac{1}{2}(\hat{a}_\omega + \hat{a}_\omega^\dagger) \ , \tag{2.38}$$

$$\hat{Y}_\omega = \frac{1}{2i}(\hat{a}_\omega - \hat{a}_\omega^\dagger) \ , \tag{2.39}$$

such that

$$[\hat{X}_\omega, \hat{Y}_\omega] = \frac{i}{2} \ . \tag{2.40}$$

$\hat{X}_\omega$ describes the amplitude of the light, $\hat{Y}_\omega$ its phase.

2.3.4 The Description of Squeezed States

Accordingly the Hamiltonian for the amplitude and phase quadrature operators is:

$$\hat{H}_\omega = \hbar\omega(\hat{X}_\omega^2 + \hat{Y}_\omega^2) \tag{2.41}$$

such that it applies $\Delta^2\hat{X}_\omega = \Delta^2\hat{Y}_\omega = \frac{1}{4}$ for the ground state with $\langle\hat{n}\rangle = 0$. The presented equations correspond to the ones of a harmonic oscillator and thus are fundamental to describe the wave character of photons and to transfer from classical optics to quantum optics. Whereas the phase quadrature is well defined as zero in classical physics, it has an uncertainty unequal to zero around its expectation value in quantum physics.

In interferometry signals at modulation frequencies Ω_i much lower than the angular light frequency ω are targeted to be measured. Therefore the current given by a photodetector in the output is decomposed into intervals of width $\Delta\Omega$ measuring the signals in $\Omega_i \pm \frac{\Delta\Omega}{2}$. For each of these intervals, there exists a pair of non commuting operators, that describe the signal and noise carried by the light at these frequencies. The spectrum of the Fourier components is the so called *window function* and the modulation of the electric field in the corresponding interval is the so called *modulation mode*. The modulation modes at a frequency Ω are described by the sum of the the carrier frequency ω of the light beam, the lower sideband with $\omega - \Omega$ and the upper sideband with $\omega + \Omega$ [8][40].

To describe the modulation modes, the short forms $\hat{X} := \hat{X}_{\Omega,\Delta\Omega}$ and $\hat{Y} := \hat{Y}_{\Omega,\Delta\Omega}$ will be used from this point. Usually these operator pairs are time independent concerning quantum noise, but time dependent concerning signals like a gravitational wave measured by an interferometer. For these new operator pairs, the Hamiltonian of the modulation mode reads [8]:

$$\hat{H} = \hbar\Omega(\hat{a}^\dagger\hat{a} + \frac{1}{2}) = \hbar\Omega(\hat{X} + \hat{Y}) \ . \tag{2.42}$$

$\hat{a}$ and $\hat{a}^+$ are the annihilation and creation operators for the modulation mode with the commutator $[\hat{a}, \hat{a}^\dagger] = 1$. $\hat{X}$ is called the *amplitude quadrature* and $\hat{Y}$ is called the *phase quadrature*. As for the corresponding operators for the light mode, it also applies for the modulation mode:

$$\hat{a} = \hat{X} + i\hat{Y} \ , \tag{2.43}$$

$$\hat{a}^\dagger = \hat{X} - i\hat{Y} \tag{2.44}$$

and

$$[\hat{X}, \hat{Y}] = \frac{i}{2} \ . \tag{2.45}$$

For two operators $\hat{A}$ and $\hat{B}$ the product of their variances is fundamentally limited by

$$\left\langle \Delta^2 \hat{A} \right\rangle \left\langle \Delta^2 \hat{B} \right\rangle \geq \frac{1}{4} \left| \left\langle [\hat{A}, \hat{B}] \right\rangle \right|^2 , \tag{2.46}$$

which is the so called Heisenberg uncertainty relation [7][17]. Applied on the quadrature operators $\hat{X}$ and $\hat{Y}$ this limit calculates as

$$\left\langle \Delta^2 \hat{X} \right\rangle \left\langle \Delta^2 \hat{Y} \right\rangle \geq \frac{1}{16} . \tag{2.47}$$

For the ground state it applies

$$\left\langle \Delta^2 \hat{X}_{\text{vac}} \right\rangle = \frac{1}{4} = \left\langle \Delta^2 \hat{Y}_{\text{vac}} \right\rangle . \tag{2.48}$$

But also states with uneven $\Delta^2\hat{X}$ and $\Delta^2\hat{Y}$ exist. According to [41] a state is called *squeezed* if the variance in one quadrature is below $\frac{1}{4}$. This does not only apply for $\hat{X}$ or $\hat{Y}$, but for any arbitrary quadrature

$$\hat{X}_\theta = \hat{X} \cos(\theta) + \hat{Y} \sin(\theta) , \tag{2.49}$$

such that

$$\left\langle \Delta^2 \hat{X}_\theta \right\rangle < \frac{1}{4} . \tag{2.50}$$

Then θ is called the *squeeze angle*. As the Heisenberg uncertainty relation given in equation (2.47) has to stay fulfilled for a squeezed state, the variance of the orthogonal quadrature will always be increased or *antisqueezed*. Figure 2.3.4 illustrates the shape of the quantum noise for a vacuum state, a state with squeezed amplitude quadrature, a state with squeezed phase quadrature and a state squeezed for an arbitrary angle θ. The factor ξ, by which the variance is reduced in comparison to the vacuum state, is called the *squeeze factor* and usually given as a value on the dB scale. The conversion is [8]

$$P_{\text{dB}} = -10 \cdot \log_{10} \left(\frac{\Delta^2 \hat{X}_\theta}{\Delta^2 \hat{X}_{\text{vac}}} \right) . \tag{2.51}$$

A different description is given by the *squeeze parameter* r with:

$$e^{-2r} = \frac{\Delta^2 \hat{X}_\theta}{\Delta^2 \hat{X}_{\text{vac}}} . \tag{2.52}$$

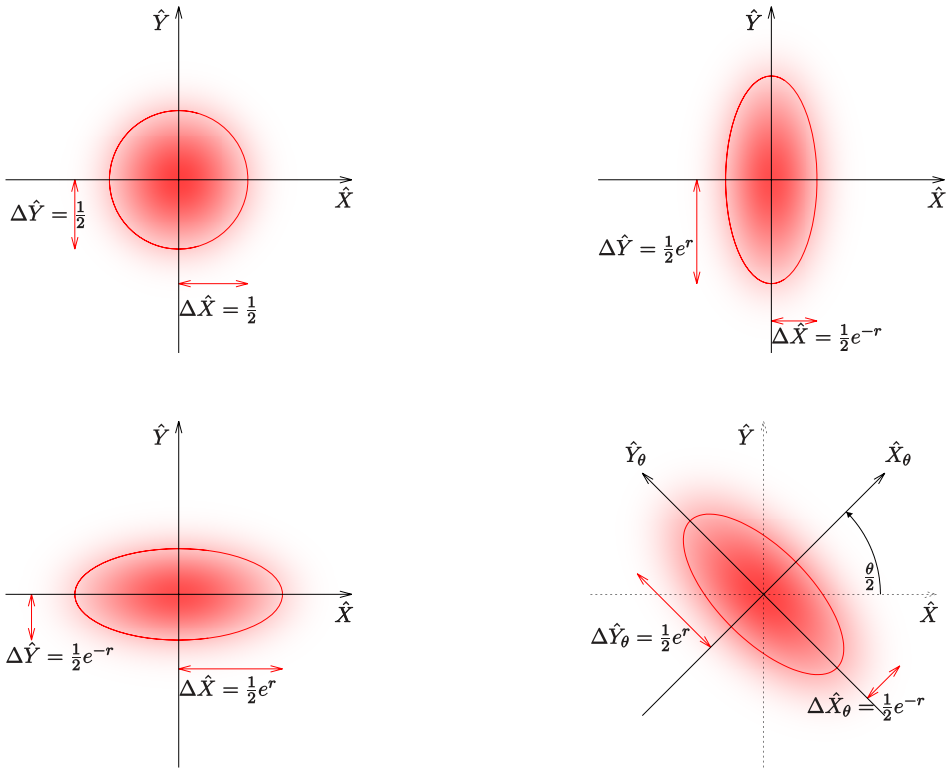

Figure 2.2: Quantum noise for a ground state and vacuum states, that are squeezed in different quadratures: The quantum noise can be visualized in the shown quadrature picture. Even for a ground state (top left) the quantum fluctuations are not zero. These vacuum fluctuations are equal in both quadratures, the amplitude quadrature $\hat{X}$ and the phase quadrature $\hat{Y}$. A state is squeezed if the fluctuations are below $\frac{1}{4}$ in one of the quadratures as in the top right for the $\hat{X}$ and the bottom left for $\hat{Y}$. r is called the squeezed parameter. A state can be squeezed for any chosen quadrature angle θ between these two as well. In the bottom right a squeezed state in the quadrature $\hat{X}_\theta$ is pictured. Then θ is called the *squeeze angle*.

To squeeze a state mathematically, the squeeze operator

$$\hat{S} = e^{\frac{1}{2}(\xi^* \hat{a}\hat{a} - \xi(\hat{a}^\dagger \hat{a}^\dagger))} \tag{2.53}$$

with

$$\xi = re^{i\theta} \tag{2.54}$$

is introduced [17]. Its expectation values for the annihilation and creation operators are:

$$\hat{S}^\dagger \hat{a} \hat{S} = \hat{a}\cosh(r) - \hat{a}^\dagger e^{i\theta}\sinh(r) \ , \tag{2.55}$$

$$\hat{S}^\dagger \hat{a}^\dagger \hat{S} = \hat{a}^\dagger\cosh(r) - \hat{a}e^{-i\theta}\sinh(r) \ . \tag{2.56}$$

From these results the variances for $\hat{X}$ and $\hat{Y}$ as defined in equations (2.38) and (2.39) follow as

$$\left\langle \Delta^2 \hat{X} \right\rangle = \frac{1}{4}[\cosh^2(r) + \sinh^2(r) - 2\sinh(r)\cosh(r)\cos(\theta)] \ , \tag{2.57}$$

$$\left\langle \Delta^2 \hat{Y} \right\rangle = \frac{1}{4}[\cosh^2(r) + \sinh^2(r) + 2\sinh(r)\cosh(r)\cos(\theta)] \ . \tag{2.58}$$

For $\theta = 0$ one receives

$$\left\langle \Delta^2 \hat{X} \right\rangle = \frac{1}{4}e^{-2r} \ , \tag{2.59}$$

$$\left\langle \Delta^2 \hat{Y} \right\rangle = \frac{1}{4}e^{2r} \ , \tag{2.60}$$

which corresponds to a state that is squeezed in the $\hat{X}$ quadrature. As described in [17] it can be shown, that applying $\hat{S}$ for an arbitrary squeeze angle θ will squeeze the state in the $\hat{X}_\theta$ quadrature.

3 The Optomechanical Setup with Silicon Nitride Membrane

Today's optomechanical experiments work a variety of oscillators is examined, whose masses, mechanical quality factors and resonance frequencies vary over several orders of magnitude. Examples are kilogram scale mirrors as the ones in gravitational-wave detectors [42][12], gram-scale mirrors [43], microtoroids [25], cantilevers [26], optomechanical crystals [27] or thin membranes made of silicon nitride as the one chosen for the presented experiment. Its properties will be described in this chapter.

For the presented work, the topology of a Michelson-Sagnac interferometer was used. Its advantages over a classical Michelson interferometer will be explained and its properties are discussed. The goal is to reach a displacement spectral density of the output signal that is dominated by shot noise at first, as a second step by the radiation pressure noise. To determine the requirements for the table top experiment described in chapter 6 the contributions of these quantum noise sources, as well as of the classical noise sources are estimated [35][29][34][31][44][8].

3.1 The Silicon Nitride Membrane

The mechanical oscillator used for the presented optomechanical experiment is a silicone nitride (SiN) membrane, that was produced by *Norcada* [46]. The thin material is strained in a silicon frame as shown on the photo on the left in figure 3.1. *Norcada* offers these with window sizes varying from $0.5\,\mathrm{mm} \times 0.5\,\mathrm{mm}$ to $2\,\mathrm{mm} \times 2\,\mathrm{mm}$ and thicknesses from 30 nm to 200 nm. These devices have quality factors of 10^6 to 10^7 and typical resonance frequencies between 10 kHz and 1 MHz depending on the thickness, size and intrinsic tension [47]. They have been used in several Fabry-Perot interferometers to measure dispersive coupling [48][49], for optical cooling [28] and to demonstrate optomechanically induced transparency [50]. In Michelson-Sagnac interferometers they served as mechanical oscillators in various experiments as [51], [52], [29] and [30].

The membrane is a dielectric medium with transmission and reflection occurring on both optical surfaces between vacuum and material. The reflectivity and transmission can be described by the Fresnel equation [53]. According to [52], the membrane's

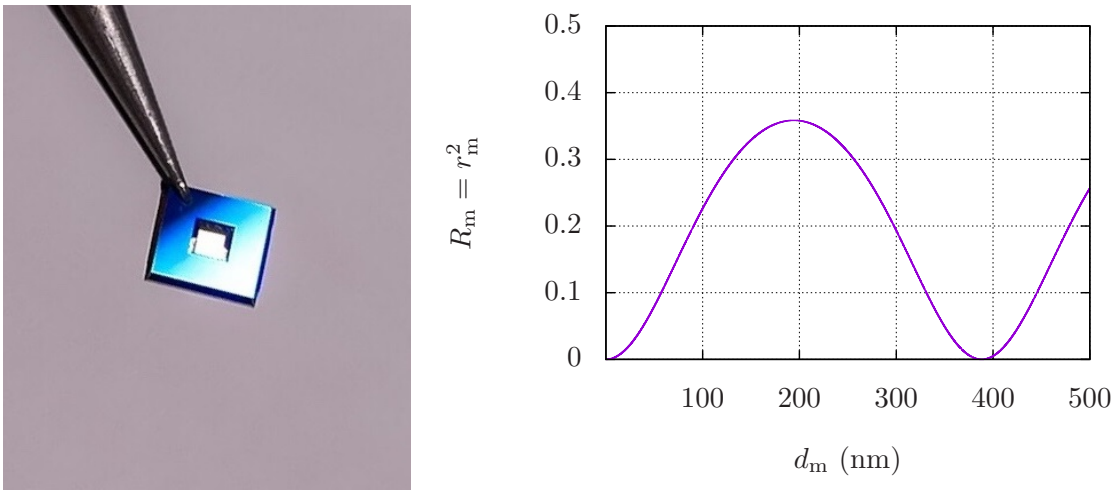

Figure 3.1: Photo of a silicon nitride membrane (left) and dependency of the membrane reflectivity on the membrane thickness (right): The photographed membrane produced by *Norcada* has a window of 1 mm × 1 mm and a thickness of 100 nm. The plotted curve of equation (3.1) is given for a membrane with a refractive index of $n_\mathrm{SiN} = 1.996$ [45] at a wavelength of $\lambda = 1550\,\mathrm{nm}$. The power reflectivity $R_\mathrm{m} = r_\mathrm{m}^2$ fluctuates periodically with increasing thickness d_m.

reflectivity in vacuum r_m for a wavelength λ can be calculated as:

$$r_\mathrm{m} = -\frac{(n_\mathrm{SiN}^2 - 1)\sin(k_\mathrm{L} n_\mathrm{SiN} d_\mathrm{m})}{2in_\mathrm{SiN}\cos(k_\mathrm{L} n_\mathrm{SiN} d_\mathrm{m}) + (n_\mathrm{SiN}^2 + 1)\sin(k_\mathrm{L} n_\mathrm{SiN} d_\mathrm{m})} \tag{3.1}$$

with k_L being the wave number and n_SiN being the refractive index of the membrane material. The dependency of the power reflectivity $R_\mathrm{m} = r_\mathrm{m}^2$ on the membrane thickness d_m is pictured on the right in figure 3.1 for a wavelength of 1550 nm and the corresponding index $n_\mathrm{SiN,1550} = 1.996$ [45]. The membrane acts as a Fabry-Perot etalon. Therefore the reflectivity depends on the thickness. At this wavelength a maximum reflectivity of $r_\mathrm{m,max}^2 = 0.358$ can not be overcome. For the thickness of the used membrane of $d_\mathrm{m} = 100\,\mathrm{nm}$ the theoretical resulting power reflectivity is:

$$R_\mathrm{m} = r_\mathrm{m,theo}^2 = 0.231\ . \tag{3.2}$$

In contrast to a classical pendulum, the membrane is not a stiff mass, but has an oscillating mass distribution with boundary conditions. For its oscillation properties not the real mass m_real, but its so called *effective mass* m_eff needs to be determined, such that the differential equation for a harmonic oscillator given in equation (2.6) is

fulfilled. As derived in [44] it applies

$$m_{\text{eff}} = \frac{m_{\text{real}}}{4} \ . \tag{3.3}$$

The resonance frequency of the membrane depends on its dimensions l_{x} and l_{y}, the intrinsic tension T, and the mass per area μ. According to [44], the resonance frequency $\Omega_{\text{res}}^{m,n}$ for an (m,n)-mode is given by

$$\Omega_{\text{res}}^{m,n} = \pi \sqrt{\frac{T}{\mu}\Big(\frac{m^2}{l_{\text{x}}^2} + \frac{n^2}{l_{\text{y}}^2}\Big)} \ . \tag{3.4}$$

The membrane in the later presented experiment was a stochiometric high stress membrane with a thickness of $d_{\text{m}} = 100\,\text{nm}$ and a square window with a size of $1\,\text{mm} \times 1\,\text{mm}$. According to [54] the membrane material had a mass density of $\rho = (2.84 \pm 0.2) \cdot 10^3 \frac{\text{kg}}{\text{m}^3}$ and the intrinsic tension was $T \approx 1\,\text{GPa}$ [46]. The calculated effective mass of the membrane therefore was

$$m_{\text{eff}} = (71 \pm 5)\,\text{ng} \tag{3.5}$$

and the resonance frequency of the (1,1) mode was expected to be

$$f_{\text{res}}^{1,1} = \frac{\Omega_{\text{res}}^{1,1}}{2\pi} \tag{3.6}$$

$$\approx 418\,\text{kHz} \ . \tag{3.7}$$

3.2 The Michelson-Sagnac Interferometer

Laser interferometers are used for precise measurements of small optical length changes. In a Michelson interferometer a beamsplitter splits an electromagnetic field into two arms. Both beams are reflected back and interfere on the same beamsplitter. A change of their path lengths results in a phase difference between the fields and therefore in an amplitude quadrature change of their sum. This effect can be measured with a photodetector. For length changes much smaller than the used laser wavelength, the differential phase change describes the change in the phase quadrature in very good approximation as well. This shall be applied to measure the displacement of the membrane as mechanical oscillator.

Using the membrane as an end mirror of a Michelson interferometer is challenging due to its low power reflectivity. For 1550 nm it applies $r_{\text{m,theo}}^2 = 0.23$ for the membrane. To avoid losses due to the high transmission a combination of a Michelson and

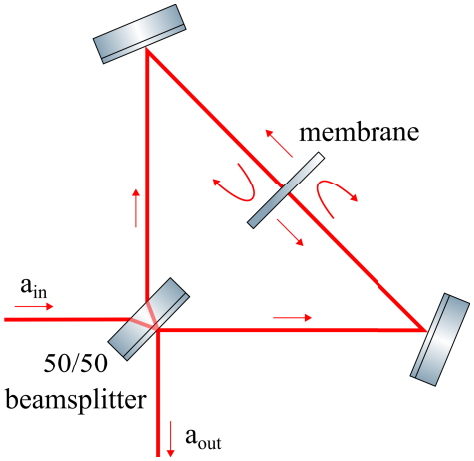

Figure 3.2: The Michelson-Sagnac interferometer topology: The incoming light is split up into two fields on the 50/50 beamsplitter. Both are reflected at the two steering mirrors and hit the membrane. The transmitted parts run through the triangular setup in opposite directions and interfere on the beamsplitter as a Sagnac-interferometer signal. The retro reflected parts interfere on the beamsplitter as a Michelson-interferometer signal.

a Sagnac interferometer was chosen. This so called Michelson-Sagnac interferometer (MSI) topology has already been successfully used in previous experiments as in [29] and [30].

The MSI as shown in figure 3.2 consists of a typical Sagnac-interferometer setup with a balanced beamsplitter and two steering mirrors. The input light with amplitude a_{in} is split up at the beamsplitter with reflectivity r_{bs} and transmission t_{bs}. The transmitted and the reflected beam run through the interferometer formed by the two mirrors in opposite directions before being overlapped again on the beamsplitter. In addition the membrane is placed in the middle between both mirrors, such that a fraction r_{m} of the light is reflected on each side and interferes as well on the beamsplitter. In consequence the output field does not only contain a Sagnac mode, but also a Michelson mode. This topology provides the signal of a Michelson interferometer with the membrane as end mirror, but the transmitted fraction t_{m} does not leave the interferometer as optical loss.

The amplitude at the output port of the interferometer is formed by the sum of

all four light fields [35]:

$$a_{\mathrm{out}} = \underbrace{a_{\mathrm{in}} t_{\mathrm{m}} r_{\mathrm{bs}}^2 e^{i\theta_{\mathrm{S1}}} + a_{\mathrm{in}} t_{\mathrm{m}} t_{\mathrm{bs}}^2 e^{i\theta_{\mathrm{S2}}}}_{\text{Sagnac mode}} + \underbrace{a_{\mathrm{in}} r_{\mathrm{m}} r_{\mathrm{bs}} t_{\mathrm{bs}} e^{i\theta_{\mathrm{M2}}} + a_{\mathrm{in}} r_{\mathrm{m}} r_{\mathrm{bs}} t_{\mathrm{bs}} e^{i\theta_{\mathrm{M2}}}}_{\text{Michelson mode}} \ . \tag{3.8}$$

To quantify the output signal, the phases (θ_{S1}, θ_{S2}) of the Sagnac mode and the phases (θ_{M1}, θ_{M2}) of the Michelson mode need to be determined. They depend on the distances between the beamsplitter and the two sides of the membrane l_1 and l_2, as well as on the phase shifts θ_{mt} and θ_{mr} that occur when the light is transmitted and reflected by the membrane:

$$\theta_{\mathrm{S1}} = \frac{2\pi}{\lambda}(l_1 + l_2) + \theta_{\mathrm{mt}} + \pi \ , \tag{3.9}$$

$$\theta_{\mathrm{S2}} = \frac{2\pi}{\lambda}(l_1 + l_2) + \theta_{\mathrm{mt}} \ , \tag{3.10}$$

$$\theta_{\mathrm{M1}} = \frac{4\pi}{\lambda} l_1 + \theta_{\mathrm{mr}} + \pi \ , \tag{3.11}$$

$$\theta_{\mathrm{M2}} = \frac{4\pi}{\lambda} l_2 + \theta_{\mathrm{mr}} \ . \tag{3.12}$$

The phase flips on the beamsplitter must add up to $\frac{\pi}{2}$ to comply with the energy conservation [55]. Therefore a flip of π for the reflection of the input beam was defined. The interferometer output amplitude normalized to the input amplitude transforms to

$$\frac{a_{\mathrm{out}}}{a_{\mathrm{in}}} = \underbrace{t_{\mathrm{m}} e^{i\theta_{\mathrm{S1}}}(t_{\mathrm{bs}}^2 - r_{\mathrm{bs}}^2)}_{\text{Sagnac mode}} + \underbrace{r_{\mathrm{bs}} t_{\mathrm{bs}} r_{\mathrm{m}} e^{\frac{i}{2}(\theta_{\mathrm{M1}} + \theta_{\mathrm{M2}})} 2\cos\left(\frac{\theta_{\mathrm{M2}} - \theta_{\mathrm{M1}}}{2}\right)}_{\text{Michelson mode}} \ . \tag{3.13}$$

Here the equation

$$e^{ix} + e^{iy} = 2e^{\frac{i}{2}(x+y)} \cdot \cos\left(\frac{x-y}{2}\right) \tag{3.14}$$

[56] was used. Equation (3.13) shows that the amplitude of the Sagnac mode is independent of a membrane displacement. From now on the beamsplitter is assumed to be perfectly balanced with $r_{\mathrm{bs}} = \sqrt{0.5} = t_{\mathrm{bs}}$, such that the Sagnac mode is equal to zero and can be neglected. In this ideal case only the Michelson mode remains. The sum $\theta_{\mathrm{M1}}+\theta_{\mathrm{M2}}$ is also independent of the membrane displacement. For the calculation of the output power, the modulus square of $e^{\frac{i}{2}(\theta_{\mathrm{M1}}+\theta_{\mathrm{M2}})}$ vanishes. The difference between the phases $\theta_{\mathrm{M2}} - \theta_{\mathrm{M1}}$ describes the influence on the output power caused by an arm length change due to a displacement of the membrane. The normalized output power

of the interferometer is given by:

$$\frac{P_{\text{out}}}{P_{\text{in}}} = \left|\frac{a_{\text{out}}}{a_{\text{in}}}\right|^2 = \frac{r_{\text{m}}^2}{2}\left[1 + \cos\left(\frac{8\pi}{\lambda}\Delta x\right)\right] . \tag{3.15}$$

The argument $\frac{8\pi}{\lambda}\Delta x$ describes the phase change caused by a membrane displacement Δx from its original position. At this point, a difference to a classical Michelson interferometer as described in [8] should be mentioned. A displacement Δx of the membrane induces a differential arm length difference of $\Delta l = 2\,|l_1 - l_2|$, whereas a displacement of one mirror in a simple Michelson interferometer only induces an arm length difference of $\Delta l = |l_1 - l_2|$.

The maximum output power is achieved at the so called *bright fringe* for $\Delta x = \frac{\lambda}{8} \cdot 2n$ and the minimum output power at the so called *dark fringe* for $\Delta x = \frac{\lambda}{8} \cdot (2n+1)$ with $n \in \mathbb{N}$.

These conditions are a good approximation for the experiment, however, a real beamsplitter is never perfectly balanced. In figure 3.3 the normalized power transmission of the interferometer according to equation (3.13) is shown for two different beamsplitter reflectivities. Using the example $|r_{\text{bs}}^2 - t_{\text{bs}}^2| = 0.1$ it illustrates that even for the case of an unbalanced beamsplitter, there is a dark fringe with $\frac{P_{\text{out}}}{P_{\text{in}}} = 0$. In comparison to the perfectly balanced case, the dark fringe is reached for a slight detuning. At this point, the leftover Sagnac mode, which is not completely dark for an unbalanced beamsplitter, interferes with the Michelson mode destructively. The height of the maxima become uneven. In the low maxima the constructively interfering Michelson mode interferes destructively with the leftover Sagnac mode, in the high maxima constructively. It has to be considered that correlated amplitude noise of the light in both arms does not vanish as for the balanced case, which is relevant for the impact of the laser noise, which is regarded in section 3.4.2. For this reason, the goal is to achieve a good balancing and therefore a high contrast with even heights of the maxima.

3.3 Quantum Noise Sources in the Interferometer

3.3.1 The Shot Noise

The laser light has a quantum uncertainty in the differential phase quadrature $Y_{\Omega,\Delta\Omega}$. As the photons are uncorrelated, the events of arriving photons are random. This effect causes the so called *shot noise*.

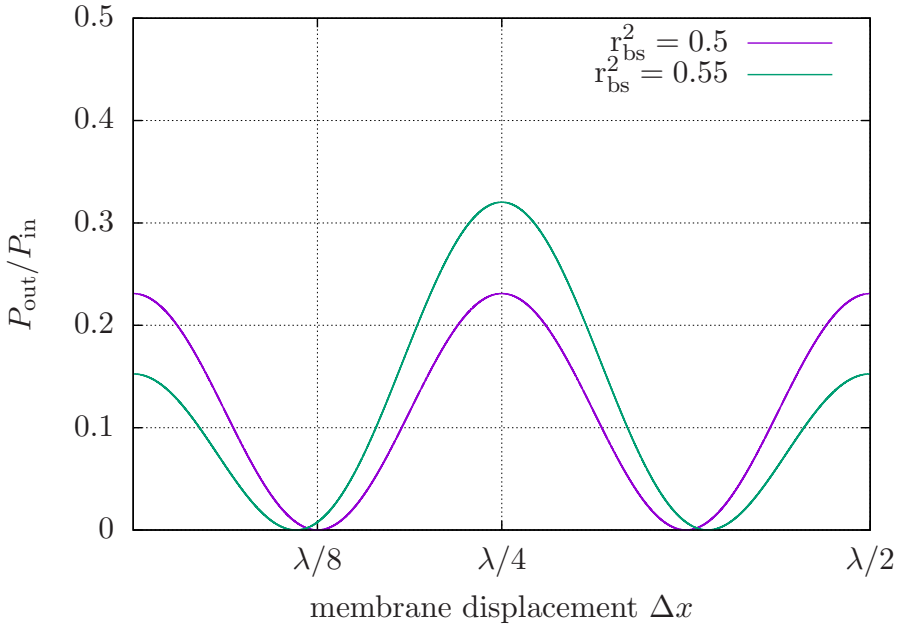

Figure 3.3: The transmission of the interferometer for a balanced and an unbalanced beamsplitter: The function following from equation (3.13) shows the normalized square of the Michelson-Sagnac interferometer transmission plotted against the membrane displacement Δx for the calculated power reflectivity $r^2_{\mathrm{m,theo}} = 0.23$ of the membrane. Even for an unbalanced beamsplitter with $|r^2_{\mathrm{bs}} - t^2_{bs}| = 0.1$ complete destructive interference can be realized. At a point slightly detuned from dark fringe of the balanced case, the Sagnac mode and the Michelson mode cancel out, such that the output power gets zero.

In the interferometer output a photodetector measures the photons arriving at times t_k:

$$I(t) = \sum_k \delta(t - t_\mathrm{k}) \tag{3.16}$$

with the average photon number $\bar{I} = \bar{n}$. The single-sided spectral density from equation (2.4) for this case is:

$$|S_I(\Omega)| = 2\bar{n} \ . \tag{3.17}$$

The power charge of each photon of the laser with an optical power P and a frequency $\omega = \frac{2\pi c}{\lambda}$ is $\hbar\omega = \frac{2\pi c\hbar}{\lambda}$. The proportionality constant $\hbar$ is the reduced Planck [2]. The power spectral density is:

$$|S_P(\Omega)| = 2 \cdot \frac{2\pi c\hbar}{\lambda} P \ . \tag{3.18}$$

This result describes the shot noise of the light field. It appears on the photodetector in the output of the Michelson-Sagnac interferometer. As the wavelength λ is given by the used laser, the output power P_out is the relevant parameter for the influence of the shot noise. As common in [57], [36] and [8], for the further thesis the linear spectral density, given by

$$\sqrt{S_\mathrm{SN}^\mathrm{MSI}} = \sqrt{2\hbar\omega P_\mathrm{out}} \tag{3.19}$$

$$= \sqrt{\frac{4\pi c\hbar P_\mathrm{out}}{\lambda}} \ , \tag{3.20}$$

will be used. The shot noise itself is not induced by a membrane displacement, but by the photons arriving on the photodetector. Nevertheless, it is indistinguishable from the interferometric signal. They differ however in their dependency of the input power. Whereas the shot noise scales with $\sqrt{P_\mathrm{in}}$, the signal scales with P_in. The shot noise single sided spectral density normalized to a signal induced by a membrane displacement Δx in units of $\frac{\mathrm{m}}{\sqrt{\mathrm{Hz}}}$ is:

$$\sqrt{S_\mathrm{SN,x}^\mathrm{MSI}} = \sqrt{\frac{S_\mathrm{SN}^\mathrm{MSI}}{\delta P_\mathrm{out}/\delta x}} \tag{3.21}$$

$$= \sqrt{\frac{\hbar c\lambda}{8\pi r_\mathrm{m}^2 P_\mathrm{in}} \frac{1 + \cos(\frac{8\pi}{\lambda}\Delta x)}{\sin^2(\frac{8\pi}{\lambda}\Delta x)}} \ , \tag{3.22}$$

where equation (3.15) was used. $S_\mathrm{SN,x}^\mathrm{MSI}$ has its minimum in $\Delta x = \frac{\lambda}{8} \times (2n+1)$, which matches the dark fringe condition from section 3.2. In this case of $P_\mathrm{out}(\Delta x = \frac{\lambda}{8}) = 0$,

the single sided spectral density of the impact of the shot noise is

$$\sqrt{S_{\mathrm{SN,x}}^{\mathrm{MSI}}} = \sqrt{\frac{\hbar c\lambda}{16\pi r_{\mathrm{m}}^2 P_{\mathrm{in}}}} \ . \tag{3.23}$$

According to this result, the shot noise of a setup with defined laser wavelength λ and a membrane with reflectivity r_{m} can only be decreased by using a higher laser input power P_{in}. An alternative option is the injection of squeezed states as it is described in section 6.3.

3.3.2 The Radiation Pressure Noise

The second quantum noise source is caused by the quantum uncertainty of the differential amplitude quadrature $X_{\Omega,\Delta\Omega}$ of the laser light. The photons hitting the membrane cause a radiation pressure force. Due to the uncertainty of the amplitude, this force is not constant. This effect is the origin of the so called *quantum radiation pressure noise*.

Each photon, that is reflected by the membrane, induces a force of $F = \frac{2\hbar\omega}{c}$. The sum of the forces of all photons for a light power P is $F_P = \frac{2}{c}P$. Coming from equation (3.17) the single sided radiation-pressure-noise spectral density can be derived similar as for the shot noise:

$$\sqrt{S_{\mathrm{RPN,x}}^{\mathrm{F}}} = \sqrt{\frac{16\pi\hbar P}{c\lambda}} \ . \tag{3.24}$$

In the Michelson-Sagnac interferometer a power of $P = r_{\mathrm{m}}^2 P_{\mathrm{in}}$ is reflected and therefore causes a force on the membrane. To receive the spectral density for the resulting displacement, equation (3.24) must be multiplied with the oscillator transfer function from equation (2.19):

$$\sqrt{S_{\mathrm{RPN,x}}^{\mathrm{MSI}}} = |H(\Omega)| \sqrt{\frac{16\pi\hbar r_{\mathrm{m}}^2 P_{\mathrm{in}}}{c\lambda}} \ . \tag{3.25}$$

A more detailed derivation, which also shows that the photons being reflected on both sides of the same oscillator don't compensate each other, can be found in [31]. Even if the beamsplitter is perfectly balanced, the radiation pressure uncertainties from the two arms don't cancel each other out due to the vacuum fluctuations entering through the open port at the output of the beamsplitter of the interferometer. In consequence of the phase flip on the beamsplitter due to the energy conservation, the vacuum fluctuations in both arms are anti correlated and the displacement noise sums up.

In contrast to the shot noise, the radiation pressure noise increases for high light powers as it follows from equation 3.25.

Figure 3.4 shows the displacement spectral densities of the two quantum-noise sources in dependency of the measurement frequency $f = \frac{\Omega}{2\pi}$ for two different input powers P_{in}. The power reflectivity $r^2_{\mathrm{m,theo}} = 0.23$ and the effective mass of $m_{\mathrm{eff}} = 71\,\mathrm{ng}$ correspond to the membrane used for the presented work. For $P_{\mathrm{in}} = 1\,\mathrm{W}$ the shot noise is three orders of magnitude higher than the radiation pressure noise. In a measurement of the total displacement spectral density only the tip of the resonance peak would be visible. To see the whole peak of the radiation pressure noise, the incoming light power needs to be increased by four orders of magnitude. For such high laser powers, issues like thermal lensing in the beamsplitter and heating of the membrane due to absorption would appear. In addition the power of the used laser is limited in the experiment, therefore different techniques as injecting squeezed stated as described in 6.3 or using signal recycling as described in section 8.4 need to be applied to reach a spectrum, that is radiation-pressure-noise limited over a broad frequency range.

3.3.3 The Standard Quantum Limit

The total quantum noise of an interferometer is given by the sum of the shot noise from equation (3.23) and the radiation pressure noise from equation (3.25). Both variances add up when the output light is detected. As

$$\sqrt{S^{\mathrm{MSI}}_{\mathrm{SN,x}}} \propto \frac{1}{\sqrt{P_{\mathrm{in}}}} \tag{3.26}$$

an input power increase results in a lower shot noise. However it applies

$$\sqrt{S^{\mathrm{MSI}}_{\mathrm{RPN,x}}} \propto \sqrt{P_{\mathrm{in}}}\ , \tag{3.27}$$

such that an input power increase results in a higher radiation pressure noise. Therefore for every measurement frequency, there is an optimum power to receive the smallest sum of both two. However, for uncorrelated radiation pressure and shot noise, the total quantum noise can not decrease below a minimum value, which is therefore

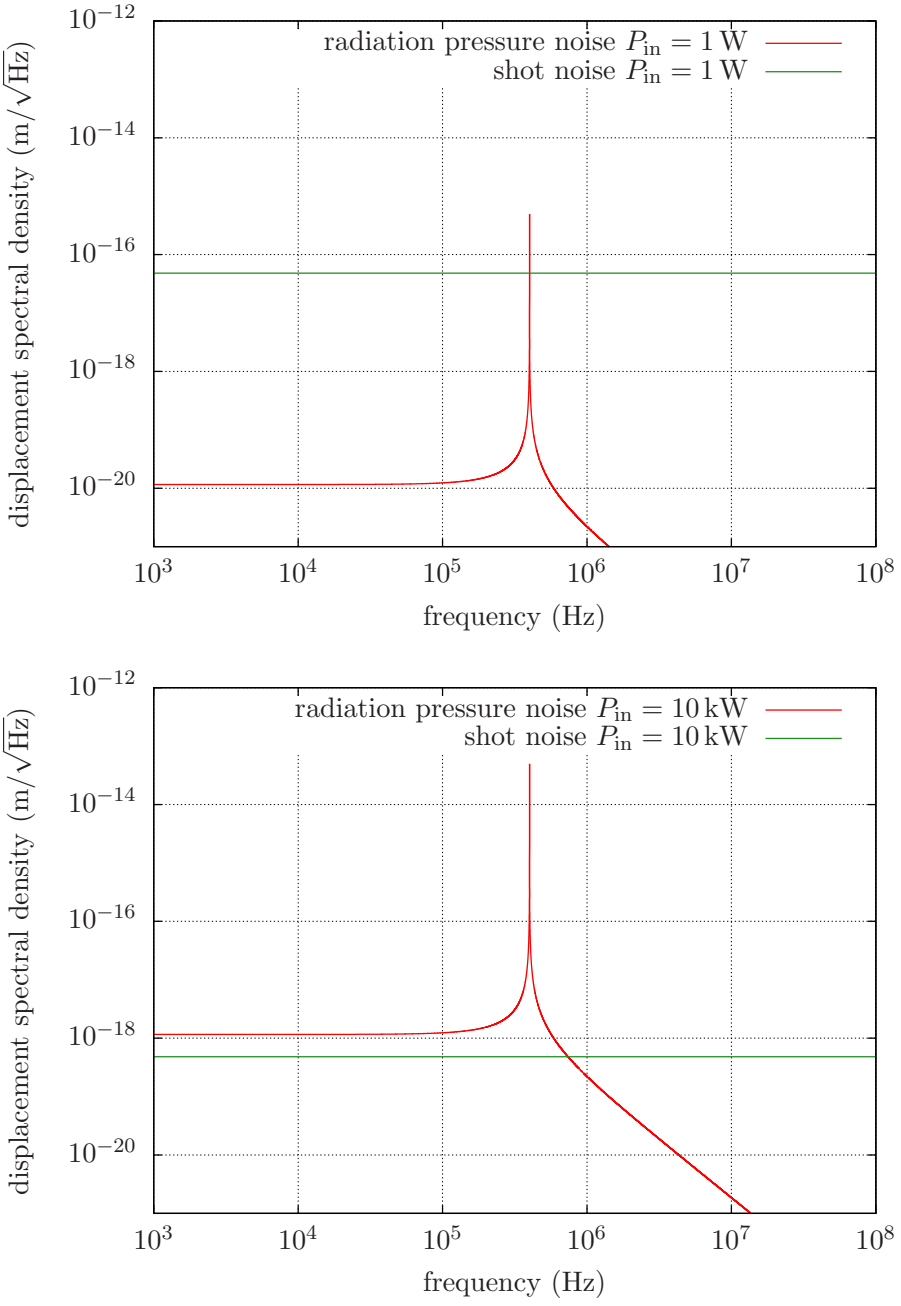

Figure 3.4: Quantum radiation pressure noise and shot noise for input powers of 1 W (top) and 10 kW (bottom): The used parameters in these models given by equations (3.23) and (3.25) are a quality factor of $Q = 10^6$, a membrane power reflectivity $r^2_{\mathrm{m,theo}} = 0.23$, an effective mass of $m_{\mathrm{eff}} = 71\,\mathrm{ng}$ and a resonance frequency of $f_{\mathrm{res}} = 400\,\mathrm{kHz}$. It shows that high input powers are required for a spectrum that is dominated by radiation pressure noise over a broad frequency range.

called the standard quantum limit. The sum of the single-sided spectral densities is:

$$S_{\mathrm{tot,x}}^{\mathrm{MSI}} = S_{\mathrm{SN,x}}^{\mathrm{MSI}} + S_{\mathrm{RPN,x}}^{\mathrm{MSI}} \tag{3.28}$$

$$= \frac{\hbar c\lambda}{16\pi r_{\mathrm{m}}^2 P_{\mathrm{in}}} + |H(\Omega)|^2 \frac{16\pi\hbar r_{\mathrm{m}}^2 P_{\mathrm{in}}}{c\lambda} \ . \tag{3.29}$$

To receive the minimum, the derivative

$$\frac{dS_{\mathrm{tot,x}}^{\mathrm{MSI}}}{dP_{\mathrm{in}}} = -\frac{\hbar c\lambda}{16\pi r_{\mathrm{m}}^2 P_{\mathrm{in}}^2} + |H(\Omega)|^2 \frac{16\pi\hbar r_{\mathrm{m}}^2}{c\lambda} \tag{3.30}$$

is set to zero which results in:

$$P_{\mathrm{SQL}}^{\mathrm{MSI}} = \frac{1}{|H(\Omega)|} \frac{c\lambda}{16\pi r_{\mathrm{m}}^2} \ . \tag{3.31}$$

This optimum input power can now be inserted into equation (3.28) to receive the standard quantum limit in $\frac{\mathrm{m}}{\sqrt{\mathrm{Hz}}}$:

$$\sqrt{S_{\mathrm{SQL,x}}^{\mathrm{MSI}}} = \sqrt{2\,|H(\Omega)|\,\hbar} \ . \tag{3.32}$$

It follows, that the minimum of the total quantum noise is reached when the shot noise and the radiation pressure noise are equal with

$$\sqrt{S_{\mathrm{SN,x}}^{\mathrm{MSI}}} = \sqrt{|H(\Omega)|\,\hbar} = \sqrt{S_{\mathrm{RPN,x}}^{\mathrm{MSI}}} \ . \tag{3.33}$$

The highest standard quantum limit is reached for the maximum of the transfer function $H(\Omega)$ from equation (2.19) at the membrane resonance frequency Ω_0:

$$\sqrt{S_{\mathrm{SQL,x}}^{\mathrm{MSI}}} = \sqrt{\frac{2\hbar Q}{m\Omega_0^2}} \ . \tag{3.34}$$

One fundamental goal in optomechanics is to undercut the standard quantum limit. When the in section 2.3.4 introduced squeeze angle θ is neither 0 or $\frac{\pi}{2}$, but any arbitrary angle in between, the uncertainties in the amplitude and phase quadrature are correlated. It is further explained in [8], how it is therefore possible to squeeze shot noise and radiation pressure noise simultaneously. The maximum enhancement for a displacement spectral density at the standard quantum limit with equal shot noise and radiation pressure noise can be realized for a squeeze angle of $\theta = \frac{\pi}{4}$.

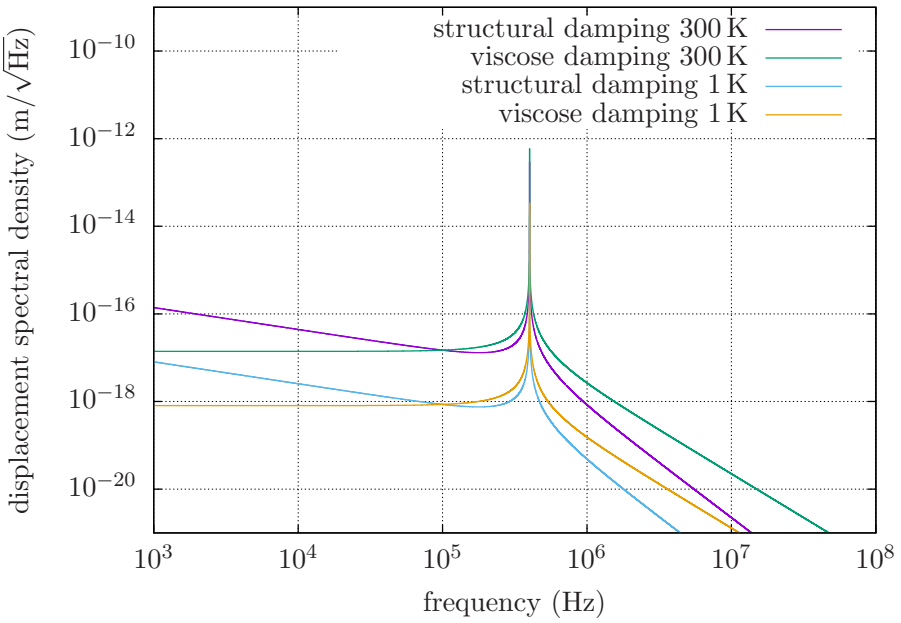

Figure 3.5: Displacement sensitivity for structural and viscous damping: The used parameters in this models given by the equations (3.38) and (3.39) are an effective mass of $m_{\text{eff}} = 71\,\text{ng}$, a resonance frequency of $f_{\text{res}} = \frac{\Omega_0}{2\pi} = 400\,\text{kHz}$ and a mechanical quality factor of $Q = 10^6$. The curves are shown for temperatures of $T = 1\,\text{K}$ and $T = 300\,\text{K}$.

3.4 Classical Noise Sources in the Interferometer

3.4.1 The Thermal Noise

In the presented work it is aimed for a quantum-noise dominated sensitivity for measurements with the described interferometer. Therefore the impact of the classical noise sources needs to be considered. For the table top Michelson-Sagnac interferometer the relevant contributions are the thermal noise and the laser noise, hence their origin and their orders of magnitude are regarded. The influence of thermal noise appears in different forms. Examples are the thermal refractive noise [58], the thermal coating noise [59] and the Brownian thermal noise of the optics [60]. The latter is the dominating source in the Michelson-Sagnac interferometer and for this reason the only one considered here. The lightest mass is the membrane, thus its Brownian thermal noise has the highest influence. The atoms have a heat induced random movement. It is caused by two different damping effects, the viscous and the structural damping. The Fluctuation Dissipation Theorem by Nyquist [61][36] states that the spectral

density in a dissipative system of thermal equilibrium is given by

$$|S^{\mathrm{x}}_{\mathrm{therm}}(\Omega)| = -\frac{4k_{\mathrm{B}}T}{\Omega}\Im[H(\Omega)] \tag{3.35}$$

with $H(\Omega)$ being the oscillator transfer function, k_{B} being the Boltzmann constant and T being the temperature of the thermal equilibrium. For the oscillator transfer functions given in equation (2.19) and (2.20) it applies

$$\Im[H_{\mathrm{vis}}(\Omega)] = -\frac{m\Omega_0\Omega}{Q_{\mathrm{vis}}}\left|H_{\mathrm{vis}}(\Omega)\right|^2 \ , \tag{3.36}$$

$$\Im[H_{\mathrm{str}}(\Omega)] = -\frac{m\Omega_0^2}{Q_{\mathrm{str}}}\left|H_{\mathrm{str}}(\Omega)\right|^2 \ . \tag{3.37}$$

With the Fluctuation Dissipation Theorem given in equation (3.35) the linear thermal-noise displacement spectral density for viscose and structural damping can be determined by using the moduli of the transfer functions from equations (2.21) and (2.22):

$$\sqrt{S^{\mathrm{x}}_{\mathrm{vis}}(\Omega)} = \sqrt{\frac{4mk_{\mathrm{B}}T\Omega_0}{Q_{\mathrm{vis}}}}\left|H_{\mathrm{vis}}(\Omega)\right| \ , \tag{3.38}$$

$$\sqrt{S^{\mathrm{x}}_{\mathrm{str}}(\Omega)} = \sqrt{\frac{4mk_{\mathrm{B}}T\Omega_0^2}{Q_{\mathrm{str}}\Omega}}\left|H_{\mathrm{str}}(\Omega)\right| \ . \tag{3.39}$$

Figure 3.5 compares the viscous and structural damping for the example of an oscillator with a resonance frequency of 400 kHz and a quality factor $Q = 10^6$. Both functions are plotted for the temperatures 300 K and 1 K. As they show the same behavior for $Q \gg 1$, from now on only the case of viscous damping will be regarded, such that $S^{\mathrm{x}}_{\mathrm{vis}}(\Omega) = S^{\mathrm{x}}_{\mathrm{temp}}(\Omega)$ and $H_{\mathrm{vis}}(\Omega) = H(\Omega)$.

The integral of equation (3.38) is independent of the quality factor and proportional to the mode temperature of the membrane. It applies [62]:

$$T_{\mathrm{mode}} = \frac{1}{2\pi}\frac{m\Omega_0^2}{k_{\mathrm{B}}}\int_0^\infty S^{\mathrm{x}}_{\mathrm{temp}}(\Omega)\ d\Omega \ . \tag{3.40}$$

In figure 3.6 the thermal noise and the previously discussed shot noise given in equation (3.23) and radiation pressure noise given in equation (3.25) are compared. With the membrane parameters $f_{\mathrm{res}} = 400\,\mathrm{kHz}$, $Q = 10^6$, $m_{\mathrm{eff}} = 71\,\mathrm{ng}$ and $r^2_{\mathrm{m,theo}} = 0.23$ and with an input power of 10 kW a radiation-pressure-noise dominated spectrum could be reached theoretically. Off resonance the thermal noise at 300 K is an order

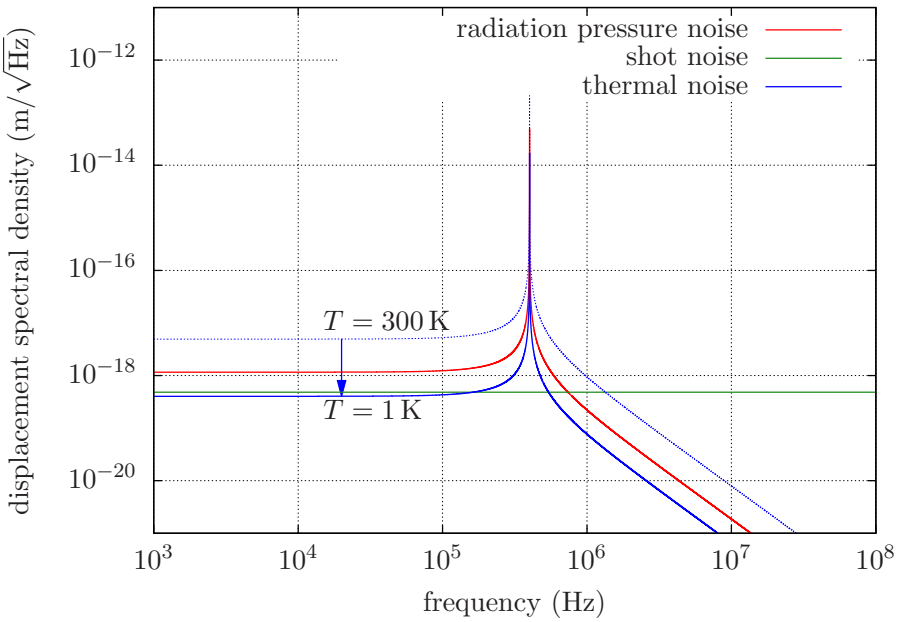

Figure 3.6: Quantum radiation pressure noise, shot noise and thermal noise for $T = 300\,\mathrm{K}$ and $T = 1\,\mathrm{K}$ for an input power $P_{\mathrm{in}} = 10\,\mathrm{kW}$: The radiation pressure noise is given in equation (3.25), the shot noise in equation (3.23) and the thermal noise in equation (3.38). The used parameters in this model are a quality factor of $Q = 10^6$, the effective mass $m_{\mathrm{eff}} = 71\,\mathrm{ng}$, the membrane power reflectivity $r^2_{\mathrm{m,theo}} = 0.23$ and a resonance frequency of $\frac{\Omega_0}{2\pi} = 400\,\mathrm{kHz}$

of magnitude higher than the quantum noise. For a temperature of 1 K however it can be decreased such, that it stays below the shot noise off resonance and below the radiation pressure noise on the peak. This graph demonstrates that the cooling of the interferometer is a crucial step to measure the radiation pressure noise over a broad frequency band.

Generally the comparison of the displacement spectral densities for the shot noise, the radiation pressure noise and the thermal noise shows, that an observation of the radiation pressure noise requires a high input power P_{in}, a high quality factor Q and a low effective mass m_{eff}. In consequence of the previous estimations, a low resonance frequency would have the advantage of a stronger response of the oscillator to radiation pressure, but another noise source, the technical laser noise, can not be neglected. Typically the laser noise decreases with higher frequencies.

3.4.2 The Technical Laser Noise

For high precision interferometric measurements the technical noise introduced by the laser system in the experiment needs to be considered. To achieve a quantum-noise dominated spectrum, the technical noise needs to be lower than the shot noise. It has to be distinguished between the frequency and the amplitude noise.

The Frequency Noise: The frequency noise only gets relevant for unequal lengths of interferometer arms or more generally for different path lengths of interfering fields. The Michelson-Sagnac interferometer has almost equal arm lengths with a difference $< 0.5\,\text{mm}$, hence it won't be discussed further. A detailed description is given in [35]. If the interferometer is enhanced using a signal-recycling mirror in the future as it will be discussed in 8.4, the effective path length of the signal path will be increased and the phase noise might have to be considered again.

The Amplitude Noise: The amplitude noise of the laser depends on the measurement frequency. It is quantified by the relative intensity noise (RIN) function which is given by the ratio of the power fluctuation to the average measured power. The power fluctuation density therefore is

$$\sqrt{S_{\text{ln}}^{P}} = \sqrt{P} \cdot \text{RIN} \ . \tag{3.41}$$

For a shot-noise limited measurement, the condition

$$\frac{\sqrt{S_{\mathrm{SN}}^{\mathrm{MSI}}}}{\sqrt{S_{\mathrm{ln}}}} > 1 \tag{3.42}$$

must be fulfilled. The influence of laser amplitude noise occurs at two points in the experiment: On the membrane and on the detector in the output. The membrane is hit by the light from both sides. Therefore the displacement noise of the membrane caused by the power fluctuations would cancel itself out for a perfectly balanced beamsplitter. For a non perfectly balanced beamsplitter with not exactly equal power reflection r_{bs}^2 and transmission t_{bs}^2, the laser noise depends on the unbalancing $\Delta_{\mathrm{bs}} = |t_{\mathrm{bs}}^2 - r_{\mathrm{bs}}^2|$. According to [35] the corresponding displacement spectral density for the interferometer output is:

$$\sqrt{S_{\mathrm{ln}}} = \frac{2}{c} \left|H(\Omega)\right| r_{\mathrm{m}}^2 \Delta_{\mathrm{bs}} S_{\mathrm{ln}}^P \ . \tag{3.43}$$

Using equations (3.18) and (3.41), the limit given in equation (3.42) transforms to

$$\Delta_{\mathrm{bs}} P_{\mathrm{in}} \cdot \mathrm{RIN} < \sqrt{\frac{4\pi c \hbar P_{\mathrm{in}}}{\lambda}} \ . \tag{3.44}$$

The second point, where the laser amplitude noise occurs, is on the photodetector. In this case not the incoming power P_{in}, but the outcoming power P_{out} is relevant. The condition from equation (3.42) transforms to

$$P_{\mathrm{out}} \cdot \mathrm{RIN} < \sqrt{\frac{4\pi c \hbar P_{\mathrm{out}}}{\lambda}} \ , \tag{3.45}$$

When the interferometer is operated at the dark fringe, the output power is in its minimum. It calculates as $P_{\mathrm{out,df}} = r_{\mathrm{m}}^2(1-C)P_{\mathrm{in}}$ with C being the contrast of the modes in the output of the interferometer.

4 The Generation and Detection of Squeezed States

The injection of squeezed states can improve the sensitivity of interferometric measurements as successfully demonstrated for ground-based gravitational-wave detectors [39][63][42]. One goal of the presented work is to achieve a comparable enhancement for an optomechanical experiment and to demonstrate that a reduction of the quantum noise for a radiation-pressure-noise limited sensitivity is possible.

Squeezed light was produced for the first time in 1985 via four-wave-mixing of sodium atoms [18]. One year later the first generation by four-wave-mixing in optical fibers was published [64]. The first squeezed states from a nonlinear crystal in a cavity were also produced in 1986 [65].

The squeezed states for this work were generated via degenerate parametric down-conversion in nonlinear crystals. The process requires a frequency-doubled pump field. This field is produced by another nonlinear process, the second-harmonic generation. For the measurement of squeezed states the principle of balanced homodyne detection is used. I built up the specific source and the balanced homodyne detector at the AEI Hannover and moved it to the ILP Hamburg. The implementation into the optomechanical experiment is presented in section 6.3 [66][8][39][38][67].

4.1 The Experimental Generation of Squeezed Vacuum States

4.1.1 Nonlinear Processes for the Generation of Squeezed States

An incoming light field entering a medium induces a separation of charges and therefore a polarization. Consequently a phase shifted electrical field is emitted. For a nonlinear medium a Taylor series of the polarization $P(t)$ decomposes it to

$$P(t) = \epsilon_0(\chi^{(1)}E(t) + \chi^{(2)}E^2(t) + \chi^{(3)}E^3(t) + ...) \tag{4.1}$$

with ϵ_0 being the vacuum permittivity, $E(t)$ being the electrical field of the incoming light and $\chi^{(1)}$, $\chi^{(2)}$, $\chi^{(3)}$,... being the susceptibilities of the different orders, which are tensors of third order [68]. For linear optics only $\chi^{(1)}$ is considered. For higher light powers also the higher orders get relevant. In the $\chi^{(2)}$ process three photons interact. The higher-order susceptibilities are small enough to be neglected for light powers under the threshold.

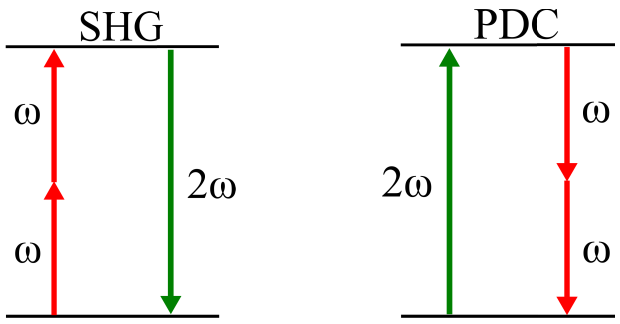

Figure 4.1: Energy level diagrams for the second-harmonic generation (left) and degenerate parametric down-conversion (right): In SHG two photons of ω excite the nonlinear medium such that a photon of 2ω is created. The degenerate PDC is the inverse process with one photon of 2ω converting into two photons of ω.

In the up-conversion the energies of two photons add up to one photon and in the down-conversion the energy of one photon gets split up into two photons. Both effects result in the creation of new frequency components as illustrated in figure 4.1. The relevant processes for the presented setup are the *second-harmonic generation* (SHG) and the degenerate *parametric down-conversion* (PDC). In the first, two photons of ω lead to an excitation of double their energy, such that a photon of 2ω gets emitted. In the second, the inverse process, two photons of ω are emitted after an excitation with a photon of 2ω [38][67].

4.1.2 Degenerate Parametric Down-Conversion

The nonlinear process to generate squeezed states is degenerate type I parametric down-conversion, thus only this type is described. The starting point for the squeezed-state generation are two fields with frequencies ω and 2ω interacting in a nonlinear medium with a second order susceptibility $\chi^{(2)}$ unequal to zero. They have amplitudes A and B as well as a phase difference $\Delta\phi$. The sum of their electromagnetic fields

$$E(t) = A\cos(\omega t + \Delta\phi) - B\cos(2\omega t) \tag{4.2}$$

induces a second-order polarization

$$\begin{aligned} P^{(2)}(E) &= \epsilon_0\chi^{(2)}[A^2\cos^2(\omega t + \Delta\phi) + B^2\cos^2(2\omega t) - 2AB\cos(\omega t + \Delta\phi)\cos(2\omega t)] \\ &= \epsilon_0\chi^{(2)}\Big[\frac{A^2}{2}[1 + \cos(2\omega t + 2\Delta\phi)] + \frac{B^2}{2}[1 + \cos(4\omega t)] \\ &\quad - AB[\cos(\omega t - \Delta\phi) + \cos(3\omega t - \Delta\phi)]\Big] \ . \end{aligned} \tag{4.3}$$

The second line of the equation shows, that the polarization contains a constant DC part, as well as parts depending on the frequencies ω, 2ω, 3ω and 4ω. The relevant effect for the squeezed-state generation is the interaction of the linear polarization component $P^{(1)} = -\epsilon_0 \chi^{(1)} A \cos(\omega t + \Delta\phi)$ with the ω dependent component $P^{(2)}_{\omega} = -\epsilon_0 \chi^{(2)} AB \cos(\omega t - \Delta\phi)$ of equation (4.3). For a phase $\Delta\phi = \frac{\pi}{2}(2n+1)$ with $n \in \mathbb{N}_0$, the field at ω is deamplified, while for a relative phase $\Delta\phi = \pi n$ the field is amplified. This is the degenerate parametric down-conversion at the fundamental frequency ω. It does not only affect the amplitude of the field, but also its quantum fluctuations.

A visualization of this process is given by the illustration in figure 4.2. Its concept by Jöran Bauchrowitz was published in [66]. Here only the degenerate parametric down-conversion for a vacuum state is shown. A complete discussion can be found in the publication. The incoming fields come from the bottom left of the picture. The bright so called *pump field* $E^{\text{in}}_{2\omega}$ with frequency 2ω and the vacuum field E^{in}_{ω} with frequency ω overlap in the nonlinear crystal and induce a separation of charges. The impact of the nonlinearity of the polarization is demonstrated by picturing the emitted field as a reflection on the function $P(E)$. It shows that the resulting field's quantum uncertainties now are phase dependently amplified and deamplified. Decomposing the field E^{out} delivers three components: $E^{\text{out}}_{2\omega}$, $E^{\text{out}}_{4\omega}$ and the squeezed vacuum field $E^{\text{out}}_{\text{sqz},\omega}$. The amplitude of the first depends on the first-order polarization $P^{(1)}(E_{2\omega})$, the amplitude of the second on the second-order polarization $P^{(2)}(E_{2\omega})$.

The illustration shows the necessity of a pump field with double frequency as it deforms the uncertainty of the original vacuum field to the characteristic curve $E^{\text{out}}_{\text{sqz},\omega}$. Compared to the incoming uncertainty the squeezing effect is revealed by the phase dependent width. In the knots of the curve the state is squeezed and in the extrema it is antisqueezed. The strength of this effect scales with the power of the pump field. Uncertainties in the pump field are small enough to be neglected. Only the vacuum input field with a frequency half of the pump field frequency is parametrically amplified.

4.1.3 Second-Harmonic Generation

As a consequence of the presented process for the squeezed-state generation, a light field with double the fundamental frequency is required. It is also generated with a nonlinear effect, the second-harmonic generation. In principle, this is the inverse

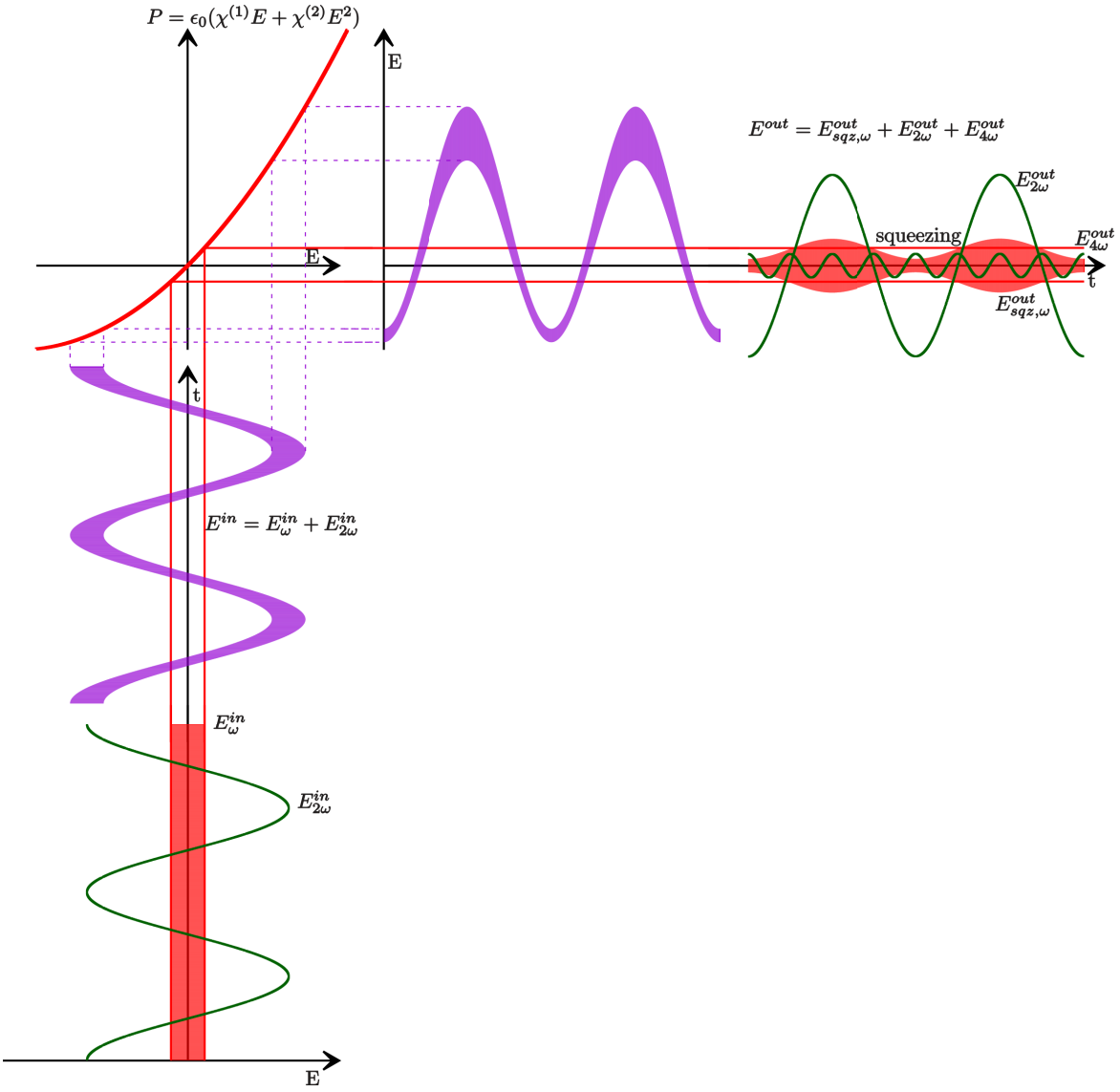

Figure 4.2: Visualization of degenerate parametric down-conversion of a vacuum state: The incoming field from the bottom is the sum of the vacuum noise with E^{in}_{ω} and a strong light field with double frequency $E^{\text{in}}_{2\omega}$. The nonlinear process in the crystal is illustrated as a reflection of the field at the nonlinear polarization function $P(E)$ in the top left. The resulting field E^{out} shows a time dependent uncertainty amplification and can be decomposed into light fields of frequencies 2ω, 4ω and a squeezed vacuum field with $E^{\text{out}}_{\text{sqz},\omega}$ at frequency ω. The concept of this illustration by Jöran Bauchrowitz was published in [66].

process to the described degenerate parametric down-conversion. A pump field with the frequency ω is used to generate an output field with 2ω. The corresponding Hamiltonian for the interaction of two fields $\hat{a}$ and $\hat{b}$ with ω_a and ω_b is:

$$\hat{H} = \hbar\omega_a \hat{a}^\dagger \hat{a} + \hbar\omega \hat{b}^\dagger \hat{b} + i\hbar\chi^{(2)}(\hat{a}^2\hat{b}^\dagger - (\hat{a}^\dagger)^2\hat{b}) \ . \tag{4.4}$$

In this case two photons of the same frequency ω of an electrical field $E(\omega)$ interact. Considering the nonlinear part of equation (4.1) the resulting polarization depends on the square of the field:

$$\begin{aligned} E^2 &= E_0^2 \cos(\omega t)^2 && (4.5)\\ &= \frac{1}{4} E_0^2 (e^{i\omega t} + e^{-i\omega t})^2 && (4.6)\\ &= \frac{1}{4} E_0^2 (e^{2i\omega t} + e^{-2i\cdot 0\cdot t} + e^{2i\cdot 0\cdot t} + e^{-2i\omega t}) && (4.7)\\ &= \frac{1}{2}(\cos(2\omega t) + 1) \ . && (4.8) \end{aligned}$$

The result contains only a term depending on the doubled frequency and a frequency independent term. Hence the generated photon in this process has the frequency 2ω [69].

Now the inhomogeneous wave equation

$$\nabla^2 \vec{E}_\mathrm{n} - \frac{\epsilon^{(1)}(\omega_\mathrm{n})}{c^2} \frac{\delta^2}{\delta t^2} \vec{E}_\mathrm{n} = \frac{1}{\epsilon_0 c^2} \frac{\delta^2}{\delta t^2} \vec{P}_\mathrm{n} \tag{4.9}$$

with the nonlinear polarization $\vec{P}_\mathrm{n}$ inducing the electromagnetic fields $\vec{E}_\mathrm{n}$ at frequencies ω_n is considered. ϵ_0 is the absolute permittivity of the vacuum and $\epsilon^{(0)}$ the relative permittivity of the medium. This equation can be derived from the Maxwell equations as described in [70]. The polarizations $\vec{P}_\mathrm{n}$ depend on the incoming fields that have to fulfill another wave equation, such that a system of coupled differential equations is formed. The susceptibilities are its coupling constants. Considering two incoming fields with intensities I_1 and I_2 and wave numbers $k_1 = \frac{\omega_1}{c_1}$ and $k_2 = \frac{\omega_2}{c_2}$, the solution

for the converted intensity in a crystal of length l is

$$I_{\text{conv}} = \frac{8 d_{\text{eff}}^2 \omega_{\text{conv}}^2 \, |I_1| \, |I_2|}{n_1 n_2 n_{\text{conv}} \epsilon_0 c^2} l^2 \text{sinc}^2\Big(\frac{\Delta k l}{2}\Big) \tag{4.10}$$

$$= I_{\text{conv}}^{\max} \begin{cases} 1 & , \Delta k = 0 \\ \left(\frac{\sin(\frac{\Delta k l}{2})}{\frac{\Delta k l}{2}}\right)^2 & , \Delta k \neq 0 \ . \end{cases} \tag{4.11}$$

d_{eff} is a scalar parameter, that substitutes the tensor $\chi^{(2)}$ under the condition of a defined propagation axis. The phase difference is $\Delta k = k_1 + k_2 - k_{\text{conv}}$ for plane wavefronts. ω_{conv} is the frequency of the converted field and n_{conv} the corresponding refractive index. The influence of the Gouy phase is neglected here. The solutions of the system of differential equations can be written as:

$$A_1^2(z) = A_1^2(0)(1 - \tanh^2(K A_1(0) z)) \ , \tag{4.12}$$

$$A_{\text{conv}}^2(z) = A_1^2(0) \tanh^2(K A_1(0) z) \tag{4.13}$$

with the amplitude of the incoming field $A_1(z)$, the amplitude of the converted field $A_{\text{conv}}(z)$ and the constant

$$K = \frac{1}{2} d_{\text{eff}} \sqrt{\frac{\mu_0}{\epsilon_0}} \sqrt{\frac{\omega_1 \omega_2 \omega_{\text{conv}}}{n_1 n_2 n_{\text{conv}}}} \ . \tag{4.14}$$

The dependency of the converted amplitude A_{conv} on the pump amplitude $A_1(0)$ and on the propagation length in the nonlinear medium along the z-axis is the same. This applies as well for the converted intensity with $I_{\text{conv}}(z) \propto A_{\text{conv}}^2(z)$. In figure 4.3 the dependencies of A_{conv} and A_1 of these parameters are plotted in arbitrary units for the ideal case of $\Delta k = 0$. It shows, that for perfect phase matching and a long crystal or high pump intensities a conversion efficiency of 100 % can be reached. There is no minimum length or pump intensity to induce the conversion process.

4.1.4 The Phase Matching

To achieve a high conversion efficiency for the second-harmonic generation and the parametric down-conversion, a good phase matching between the incoming and the generated field inside the used medium is of interest. The dispersion causes a mismatch between the velocities of the fields of different wavelengths. This effect leads to constructive interference of the generated waves, created at different points in the medium. As shown in figure 4.3 the crystal length should be long for a high conversion.

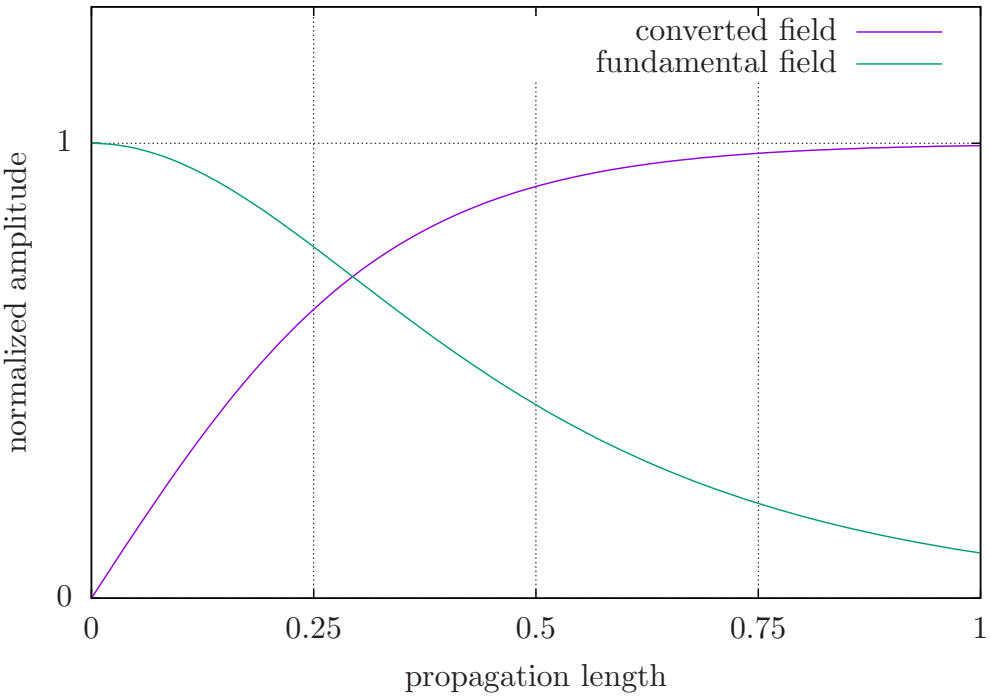

Figure 4.3: Theoretical converted amplitude $A_{\mathrm{conv}}(z)$ in a nonlinear crystal: Assuming $\Delta k = 0$, the converted amplitude given by equation (4.13) shows the same dependency on the crystal length as on the incoming pump power. For long crystals or high powers an efficiency close to 100 % can be reached. No minimum intensity or length is required to induce the process.

But considering equation (4.11) the converted intensity decreases for a defined phase difference Δk due to the $\mathrm{sinc}^2(\frac{\Delta k l}{2})$ term. After the length $l = \frac{1}{\Delta k}$, the converted field is converted back. The coherence length

$$l_{\mathrm{coh}} = \frac{2}{\Delta k} \tag{4.15}$$

defines the length before the fields diverge. The goal is to achieve that both fields propagate with the same speed, such that the phases match and the efficiency reducing destructive interference is minimized.

The phase mismatch for the second-harmonic generation is

$$\Delta k = 2k_1 - k_{\mathrm{conv}} \tag{4.16}$$

with the wave numbers $k_1 = \frac{\omega_1}{c_1}$ and $k_{\mathrm{conv}} = \frac{\omega_{\mathrm{conv}}}{c_{\mathrm{conv}}}$. The resulting phase matching condition is

$$\Delta k = 2k_1 - k_{\mathrm{conv}} = 0 \ , \tag{4.17}$$

which transforms to

$$\frac{n_{\mathrm{conv}}\omega_{\mathrm{conv}}}{c_{\mathrm{conv}}} = 2\frac{n_1\omega_1}{c_1} \ . \tag{4.18}$$

As it applies $\omega_{\mathrm{conv}} = 2\omega_1$, the concluding condition for perfect phase matching is $n_1 = n_{\mathrm{conv}}$. Considering the dependencies of the absorption coefficients and refractive indices of materials for the used light frequencies, this condition is challenging to realize. One approach is the usage of the birefringence of a nonlinear material with different refractive indices for the ordinary and the extraordinary polarization [68].

An alternative is the here applied so called *quasi phase matching*. Figure 4.4 illustrates the difference between a usual nonlinear crystal and one for quasi phase matching. The crystal on top is continuously poled in one direction. The crystal in the bottom has areas with alternating polarization directions. To realize such a medium, the crystal needs to be a ferroelectricum. This means, that its crystalline symmetry allows a polar axis, that can be polarized in different directions by shifting charged ions. To produce such a crystal, stripes of an isolating material are applied on the surface using lithography. Then it is covered with a electrolyte liquid and a high voltage is applied. The resulting flipped polarization of the not covered areas is stable at room temperature. Usual materials for this procedure are lithium niobate (LN) and potassium titanyl phosphate (KTP). Here a crystal of periodically poled potassium titanyl phosphate

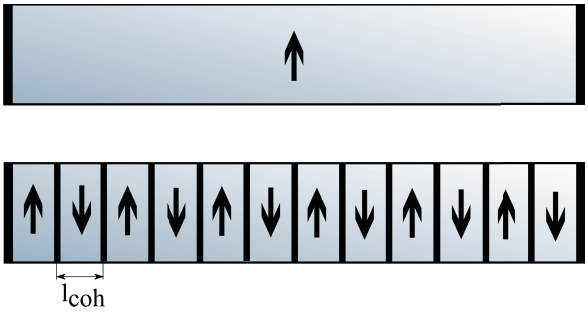

Figure 4.4: Comparison of a simple nonlinear crystal (top) and a periodically poled nonlinear crystal (bottom): In a simple crystal as shown above the effective polarization inside the crystal is constant over its full length. For quasi phase matching a periodically poled crystal is used. The direction of the effective nonlinearity varies between different regions with the thickness of the coherence length l_{coh}.

(PPKTP) was used [38].

The thickness of a layer of one polarization is l_{coh} to achieve the optimum quasi phase matching. Over this length the fundamental and the second-harmonic wave are in phase. In a usual crystal, they would separate afterward, but in the periodically poled crystal they enter a layer of the opposite polarization, in which they run back together. The resulting effect is illustrated in figure 4.5 for a linear approximation of the tanh-function in the converted amplitude from equation (4.13). In the theoretical case of a medium with the same refractive index for both wavelengths the converted amplitude would increase with the propagation length. In a realistic crystal with one polarization direction the converted light is converted back, such that the amplitude fluctuates, but never reaches high values. In the case of quasi phase matching the waves run back together after the coherence length l_{coh} and the converted part increases with slight oscillations. For an efficient conversion, the crystal must be temperature stabilized. The temperature influences the refractive index and the length of the crystal and therefore also the thickness of the layers in the periodically poled case. The temperature for maximum conversion is called the *phase matching temperature* [38].

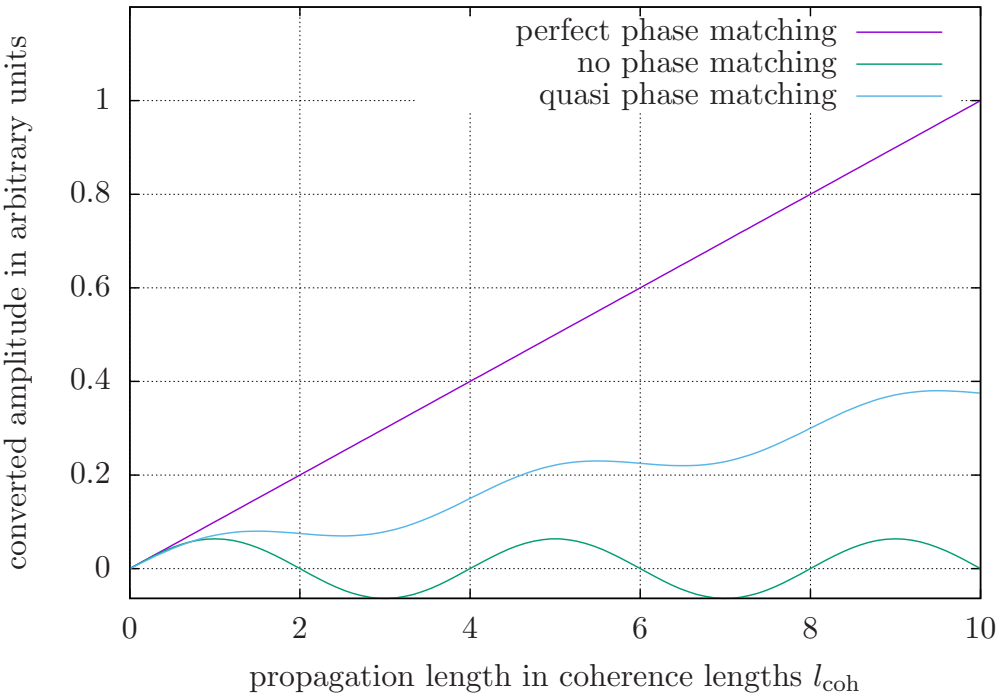

Figure 4.5: Qualitative comparison of the converted amplitude in an ideal, in a regular nonlinear crystal and in a periodically poled crystal: For an ideal crystal with an equal refractive index for the fundamental and the second-harmonic wavelength, the converted amplitude would increase linearly with the crystal length. In a regular crystal with one polarization direction the converted light is converted back after the coherence length. In a periodically poled crystal the waves run back together when they enter the layer of opposite polarization. The converted amplitude shows a small oscillation, but increases with the length.

4.2 The Detection of Squeezed States

4.2.1 The Principle of Balanced Homodyne Detection

With a single photodiode only noise in the amplitude quadrature $\hat{X} = \hat{X}^{\theta=0°}_{\Omega,\Delta\Omega}$ can be measured. In contrast, a balanced homodyne detector using two photodiodes provides the option to characterize a squeezed state for all angles θ. But this is only one of the advantages. When squeezed vacuum or a dark interferometer output is supposed to be measured as in the presented work, the vacuum shot-noise level can be determined with a balanced homodyne detector, but not with a single photodiode.

The scheme as shown in figure 4.6 consists of two photodiodes and a balanced beamsplitter. The signal field $\hat{b}$ hits the beamsplitter in one port. It is overlapped with an external so called *local-oscillator* field $\hat{a}$ entering through the other input port. Here a perfect matching of the modes is assumed. The amplitude of the local-oscillator field should be much higher than the one of the signal. The two output fields $\hat{c}$ and $\hat{d}$ are focused on the photodiodes. The difference of the voltages is formed electronically. By shifting the phase θ of the local-oscillator beam, the phase relation between the fields is defined.

For a balanced beamsplitter with $r^2_{\mathrm{bs}} = 0.5$, the resulting photo voltages for the single photodiodes are proportional to:

$$\hat{c}^\dagger\hat{c} = \frac{1}{2}(\hat{a}^\dagger + \hat{b})(\hat{a} + \hat{b}^\dagger) \ , \tag{4.19}$$

$$\hat{d}^\dagger\hat{d} = \frac{1}{2}(-\hat{a}^\dagger + \hat{b}^\dagger)(-\hat{a} + \hat{b}) \ . \tag{4.20}$$

Here a phase flip of π of $\hat{a}$ at reflection was chosen to fulfill the energy conversation. To calculate the difference of the voltages, the amplitudes can be written as described in [71] as

$$\hat{a} = \alpha + \delta\hat{a} \ , \qquad \hat{a}^\dagger = \alpha^* + \delta\hat{a}^\dagger \ , \tag{4.21}$$

$$\hat{b} = \beta + \delta\hat{b} \ , \qquad \hat{b}^\dagger = \beta^* + \delta\hat{b}^\dagger \tag{4.22}$$

with $\alpha = \langle\hat{a}\rangle$ and $\beta = \langle\hat{b}\rangle$ being the classical amplitudes of the fields whereas $\delta\hat{a}$ and $\delta\hat{b}$ are the time dependent fluctuations including the quantum noise. The phase of $\hat{b}$

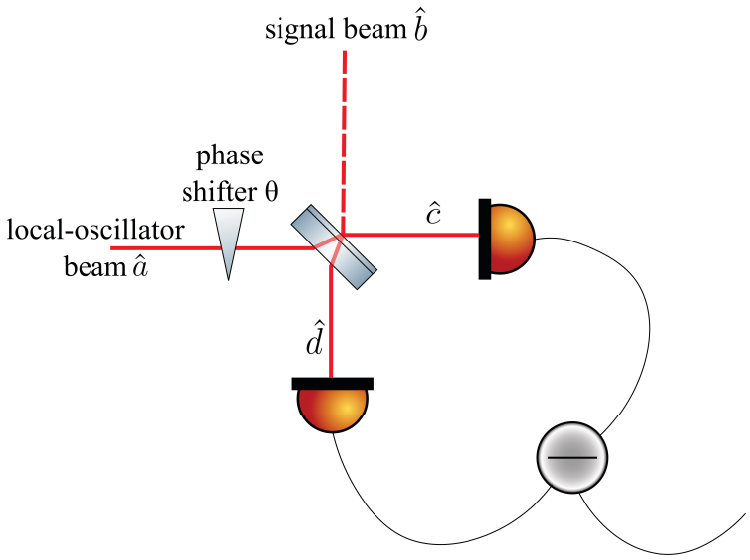

Figure 4.6: The principle of balanced homodyne detection: The local-oscillator beam $\hat{a}$ and the signal beam $\hat{b}$ interfere on a 50/50 beamsplitter and the resulting fields $\hat{c}$ and $\hat{d}$ induce photo voltages in the photodiodes, whose difference serves as homodyne detector signal. The phase θ between both fields can be shifted to choose the quadrature angle for the measurement.

is used as the reference phase, such that β is a real number. It applies:

$$\hat{a} = \hat{a}_0 e^{i\theta} = \alpha_0 e^{i\theta} + \delta\hat{a}_0 e^{i\theta} \tag{4.23}$$

with the phase θ between both fields. This leads to the difference of the photo voltages

$$\begin{aligned} V_- &\propto \left\langle \hat{c}^\dagger \hat{c} - \hat{d}^\dagger \hat{d} \right\rangle && (4.24)\\ &= \Big\langle (\alpha_0\beta + \alpha_0\delta\hat{b} + \delta\hat{a}_0^\dagger\beta + \delta\hat{a}_0^\dagger\delta\hat{b}_0)e^{-i\theta} && (4.25)\\ &\quad + (\beta\alpha_0 + \beta\delta\hat{a}_0 + \delta\hat{b}_0^\dagger\alpha + \delta\hat{b}_0^\dagger\delta\hat{a}_0)e^{\theta} \Big\rangle && (4.26)\\ &= \Big\langle 2\alpha_0\beta\cos\theta + \alpha_0\delta\hat{X}_b^\theta + \beta\delta\hat{X}_a^{-\theta} + \delta\hat{a}_0^\dagger\delta\hat{b}_0 e^{-i\theta} + \delta\hat{b}_0^\dagger\delta\hat{a}_0 e^{-\theta} \Big\rangle. && (4.27) \end{aligned}$$

with $\delta\hat{X}_a^{-\theta} = \frac{1}{2}(\delta\hat{a}e^{i\theta} + \delta\hat{a}^\dagger e^{-i\theta})$ and $\hat{X}_b^\theta = \frac{1}{2}(\delta\hat{b}e^{-i\theta} + \delta\hat{b}^\dagger e^{i\theta})$ being the quadrature operators of the amplitude fluctuations $\delta\hat{X}_a^\dagger = \delta\hat{a} + \delta\hat{a}^\dagger$ and $\delta\hat{X}_b^\dagger = \delta\hat{b} + \delta\hat{b}^\dagger$ for the phases $-\theta$ and θ. As the light power of the local-oscillator field is much higher than the signal field, one can assume $\beta^2 \ll \alpha_0^2$ or for the case of a squeezed vacuum state even $\beta = 0$. Also the contributions depending only on the fluctuations can be neglected.

Therefore

$$V_- \propto \left\langle \alpha_0 \delta \hat{X}_b^\theta \right\rangle \tag{4.28}$$

is a valid approximation. This result demonstrates the advantages of using a balanced homodyne detector instead of a signal photodiode. The local-oscillator amplitude replaces the one of the signal field, amplifying its fluctuations. It enables the feature to choose the phase difference θ to the signal beam and thereby allows to measure the noise of a state

$$\hat{X}^\theta(t) = \cos(\theta)\hat{X}(t) + \sin(\theta)\hat{Y}(t) \ , \tag{4.29}$$

for a chosen quadrature angle θ. For $\theta = 0$ one obtains the amplitude quadrature $\hat{X}(t)$ and for $\theta = \frac{\pi}{2}$ the phase quadrature $\hat{Y}(t)$ [8].

4.2.2 The Impact of Optical Losses in the Homodyne Detector

The minimization of optical losses is crucial to reach high squeezing. An ideal detector would measure a noise power of a squeezed vacuum state with variance $\Delta^2\hat{X}_\theta$, normalized to the variance $\Delta^2\hat{X}_{\text{vac}}$ of a non-squeezed vacuum state [8]:

$$P_{\text{dB}} = -10\log_{10}\left(\frac{\Delta^2\hat{X}_\theta}{\Delta^2\hat{X}_{\text{vac}}}\right) = -10\log_{10}(e^{-2r}) \ . \tag{4.30}$$

The squeeze parameter r was introduced in 2.3.4. This equation however does not consider the effect of optical losses. For measurements of squeezed states, these result not only in the detection of less signal, but also in the overlap with vacuum fluctuations. In consequence the squeezing ellipse is broadened and the squeeze factor decreases. For a detection efficiency η^2 and resulting optical loss of $(1-\eta^2)$ the squeezed variance transforms to

$$\Delta^2\hat{X}_{\theta,\eta} = \eta^2\Delta^2\hat{X}_{\theta,\eta=1} + (1-\eta^2)\Delta^2\hat{X}_{\text{vac}} \tag{4.31}$$

with a measured relative noise power of

$$P_{\text{dB},\eta} = -10\log_{10}[\eta^2 e^{-2r} + (1-\eta^2)] \ . \tag{4.32}$$

For $\eta = 0$ it applies $P_{\text{dB,sqz}} = -P_{\text{dB,antisqz}}$. In figure 4.7 the detected noise power $P_{\text{dB},\eta}$ is plotted against the detection efficiency η^2 for states with original relative noise powers of $P_{\text{dB},\eta=0} = \pm 5\,\text{dB}$, $P_{\text{dB},\eta=0} = \pm 10\,\text{dB}$ and $P_{\text{dB},\eta=0} = \pm 15\,\text{dB}$. It shows that the squeeze factor decreases much steeper with decreasing efficiency than the antisqueeze

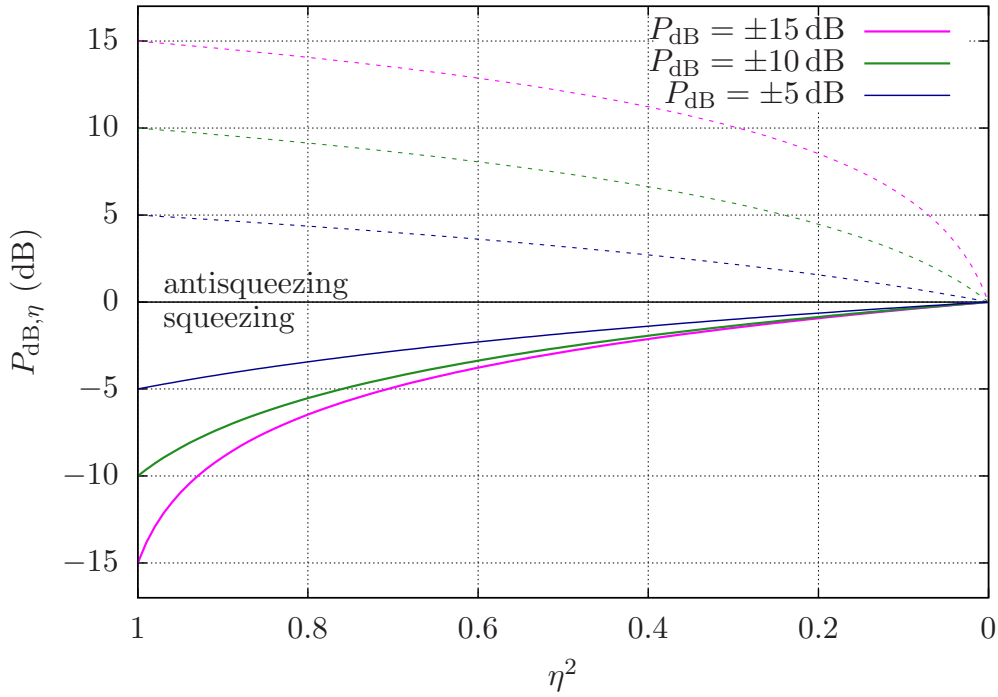

Figure 4.7: Reduction of the squeeze factor due to optical losses: The theoretical graph shows the relative squeeze factor $P_{\mathrm{dB},\eta}$ in dependence of the measurement efficiency η^2 for initial squeezing values of $P_{\mathrm{dB},\eta=0} = -15\,\mathrm{dB}$, $-10\,\mathrm{dB}$ and $-5\,\mathrm{dB}$ as given by equation (4.32). The corresponding antisqueezing is shown by the dashed lines. The higher the optical loss, the lower is the efficiency and the lower is the measured squeeze and antisqueeze factor. It can be seen, that especially for high initial factors already small optical losses reduce the squeezing significantly.

factor. The higher the initial squeezing value is, the quicker it drops with increasing losses.

Thus, to reach high squeezing, the experiment requires high quality optics as well as a good contrast of the interferometer. The so called *propagation loss* L appears due to imperfect optics, for example a mirror in the path with a transmission $t^2 = L$. The reduced detection efficiency is described by

$$\eta_L^2 = 1 - L \ . \tag{4.33}$$

The imperfect quantum efficiency of the photodiodes of the balanced homodyne detector is another cause of optical loss. The not detected percentage of the light degrades the detection efficiency the same way as imperfect optics.

A good mode overlap of the injected squeezed vacuum field with the local-oscillator field is required. A mismatch between the beams like differences in the radii of curvature of the wavefronts or different polarizations causes additional optical losses. If the field in one homodyne detector arm is detected with a single photodiode for equal powers of the two incoming beams, the overlap between both fields can be quantified. The visibility is defined as

$$VIS = \frac{V_{\max} - V_{\min}}{V_{\max} + V_{\min}} \tag{4.34}$$

with $V_{\max}$ being the maximum voltage for constructive interference and $V_{\min}$ being the minimum voltage for destructive interference. The visibility corresponds to the detection efficiency

$$\eta_{\text{overlap}}^2 = VIS \ . \tag{4.35}$$

Another influence to be considered is the escape efficiency of the resonator

$$\eta_{\text{escape}}^2 = \frac{t_{\text{m}}^2}{T + L_{\text{cav}}} \tag{4.36}$$

with L_{cav} being the intra cavity round trip loss and t_{m}^2 being the power transmission of the coupling mirror [39]. The round trip loss is caused by absorption in the crystal and imperfect antireflective coatings.

4.2.3 The Impact of Phase Jitter

To measure high squeezing, the impact of phase noise needs to be taken into account. The readout quadrature of the balanced homodyne detector is determined by the phase relation between the signal and the local-oscillator field. Oscillations of optical components caused by incoupling acoustic vibrations disturb this phase relation. If the period of such an oscillation is below the recording time for one data point of the spectrum analyzer, the point is an integral over a range of angles depending on the amplitude of the oscillation. As a result, the measured point does not correspond to the maximum squeezing factor but to a mixture with the antisqueezed quadrature, thus it has a reduced value [72].

Simulations in [39] comparing squeezing for a constant angle and for a jittering angle demonstrate, that especially for low frequencies below 1 MHz this effect degrades the detected squeeze factor. An indicator for present phase noise is, that the squeezing does not increase monotonously with increasing pump power, but decreases after reaching a maximum.

4.3 The Generation of Squeezed Light for the Optomechanical Experiment

4.3.1 The Resonators for the Squeezed-State Generation

To produce frequency-doubled light and squeezed states, a nonlinear medium is required. By placing the used crystals inside resonators, the conversion efficiency could be enhanced significantly. In addition resonators determine the transversal spatial mode of the amplified field, usually the TEM_{00} mode. For the squeezed-states generation antisqueezed states from other modes were suppressed.

Both cavities are schematically shown in figure 4.8. One end mirror of each cavity was given by the coating on the curved side of the crystal, the other by a coupling mirror. This mirror was attached to a piezo-electric element, that was used to change the resonator length by applying a voltage. It was screwed onto the aluminium frame, that surrounded the other components. The plane side of the crystal had an antireflective coating for both wavelengths. The crystal was heated with a Peltier element. An negative temperature coefficient (NTC) resistor was implemented to measure the temperature. Using the resistance as reference value, a temperature control loop was built up to provide a stable operating temperature and to achieve the best possible

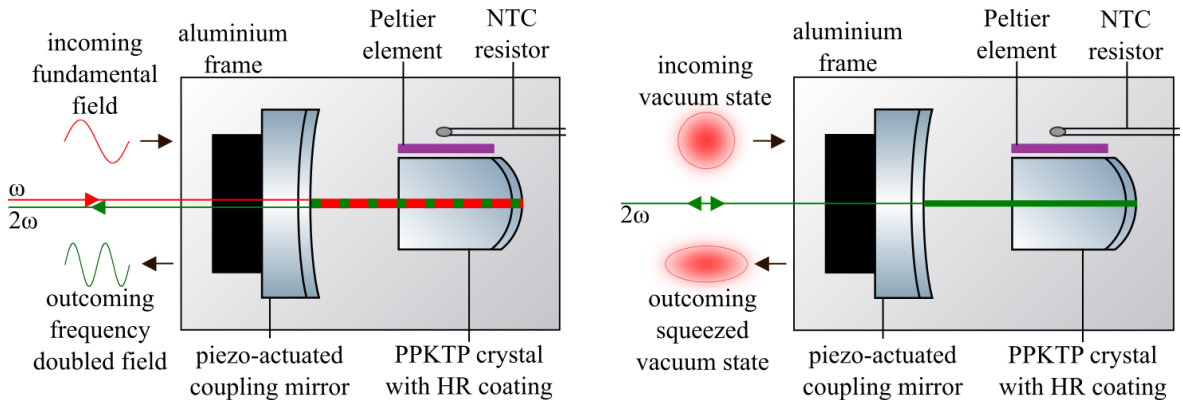

Figure 4.8: The resonators for the second-harmonic generation (left) and the degenerate parametric down-conversion (right): In both cases the resonator is formed by the coating on the curved side of the nonlinear crystal and a coupling mirror, that is attached to a piezo-electric element, which is used for the length stabilization. The crystal is heated with a Peltier element. The resistance of the attached NTC resistor acts as reference value for a temperature stabilization control loop. The components are surrounded by an aluminium frame. The SHG resonator is pumped with light at the fundamental wavelength and frequency-doubled light is generated. The PDC resonator is pumped with the frequency-doubled light to squeeze the uncertainty of the incoming vacuum field.

phase matching.

The SHG resonator: For the generation of frequency-doubled light, a high power pump field with the fundamental wavelength is sent into the SHG resonator. Both sides have a high reflectivity for the fundamental wavelength. The coupling mirror has a high reflectivity for the fundamental field, but a low reflectivity for the frequency-doubled field. Due to this configuration, the pump field light is amplified and with every round trip more photons at the doubled frequency are generated, that transmit through the coupling mirror.

The PDC resonator: A cavity for the optical parametric amplification introduces a threshold pump power, above which the vacuum field is amplified to a bright laser field. This effect is called an *optical parametric oscillator*. For the generation of squeezed

	Reflectivity mirror 1550 nm	Reflectivity mirror 775 nm	Reflectivity crystal 1550 nm	Reflectivity crystal 775 nm
SHG	90 %	< 1 %	> 99.8 %	99.5 %
PDC	85 %	97.5 %	99.95 %	99.5 %

Table 1: Power reflectivities of the SHG and PDC resonators.

states pump powers below this threshold were used [8].

The chosen reflectivities for the PDC resonator are crucial to reach high squeezing. For equal reflectivities of both end mirrors $r_1 = r = r_2$ an incoming mode matched field is transmitted completely. The resonator is called *impedance matched*. In consequence no part of the uncertainty of the vacuum field is reflected. Due to the full transmission of the vacuum state in both directions, the mode propagating away from the resonator is not nonclassical.

In the case of the so called *overcoupled* resonator, the crystal's reflectivity is higher than the reflectivity of the coupling mirror $r_2 > r_1$. For a perfectly overcoupled resonator with $r_2 = 1$, no field could enter or leave the resonator through the back. The amplitude quadrature of the reflected field on the high-reflective side destructively interferes with itself. The coupling mirror is partially transmissive, such that the internal resonator mode couples to the external modes on this side, the incoming and the outcoming fields. If a nonlinear crystal is added to such a resonator, infinite squeezing can be achieved. The gain in the crystal per round trip due to the parametric down-conversion can mimic the impedance matched case. It can be shown that the strongest possible intra cavity squeeze factor is $\frac{(1+r_1)^2}{r_1^2}$ [67]. For the case of high reflectivities this value is 6 dB and averaged over the full resonator mode, the limit is 3 dB [73]. The external field shows infinite squeezing.

The specific resonators in the experiment: In the presented work the fundamental light had a wavelength of 1550 nm and the frequency-doubled light a wavelength of 775 nm. Both resonators for the second-harmonic generation and the degenerate parametric down-conversion consisted of a coupling mirror and a crystal of periodically poled potassium titanyl phosphate (PPKTP). The power reflectivities of the optics for both wavelengths are given in table 1. In previous setups as [39] the PDC cavity was

only resonant for the fundamental wavelength, such that high pump powers in the magnitude of 100 mW were required for the degenerate parametric down-conversion. The resonator for the squeezed-state generation in this experiment had high reflectivities on both sides for both relevant wavelengths. The waist sizes for the TEM_{00} mode for both wavelengths and the amplification of the incoming amplitude a_{in} inside the cavity were simulated with the software *finesse* by Andreas Freise. From the reflectivities, the radii of curvature of the mirror $r_{\mathrm{c,m}} = 20\,\mathrm{mm}$ and the crystal $r_{\mathrm{c,c}} = 12\,\mathrm{mm}$, the length of the air gap $l_{\mathrm{air}} = 20\,\mathrm{mm}$ and the crystal length $l_{\mathrm{c}} = 8.3\,\mathrm{mm}$, the waist sizes were calculated:

$$w_0^{775} = 25\,\mu\mathrm{m}\ , \tag{4.37}$$

$$w_0^{1550} = 35\,\mu\mathrm{m}\ . \tag{4.38}$$

For the amplitude a_{cav} inside the cavity applied

$$|a_{\mathrm{cav}}|^2 = 107 \cdot |a_{\mathrm{in}}|^2\ . \tag{4.39}$$

Due to the double resonance, the temperature of the crystal had to be chosen such, that the resonance condition was fulfilled for both wavelengths at the same cavity length. This requirement had the consequence, that the squeezed-light source could only be operated at a selection of temperatures. The closest one to the phase matching temperature was chosen. Even if the temperature did not match the temperature for perfect phase matching, the necessary pump power for the presented squeezed-light source was in the order of magnitude of 10 mW.

4.3.2 The Setup of the Squeezed-Light Source

The squeezed-light source in this experiment was a table top experiment, that I built during my master thesis at the AEI Hannover [38]. The setup is shown in figure 4.9. The laser light with the fundamental wavelength of 1550 nm was split up into different beams. One part of the light went directly to the balanced homodyne detector as local oscillator. The balanced homodyne detector electronics were designed and built by Moritz Mehmet, who used the device for the measurement of 12.3 dB squeezing in [74].

One light field with a wavelength 1550 nm was used as pump field entering the SHG cavity through the coupling mirror. The generated frequency-doubled light of 775 nm left the resonator through the same mirror and transmitted through a dichroitic mir-

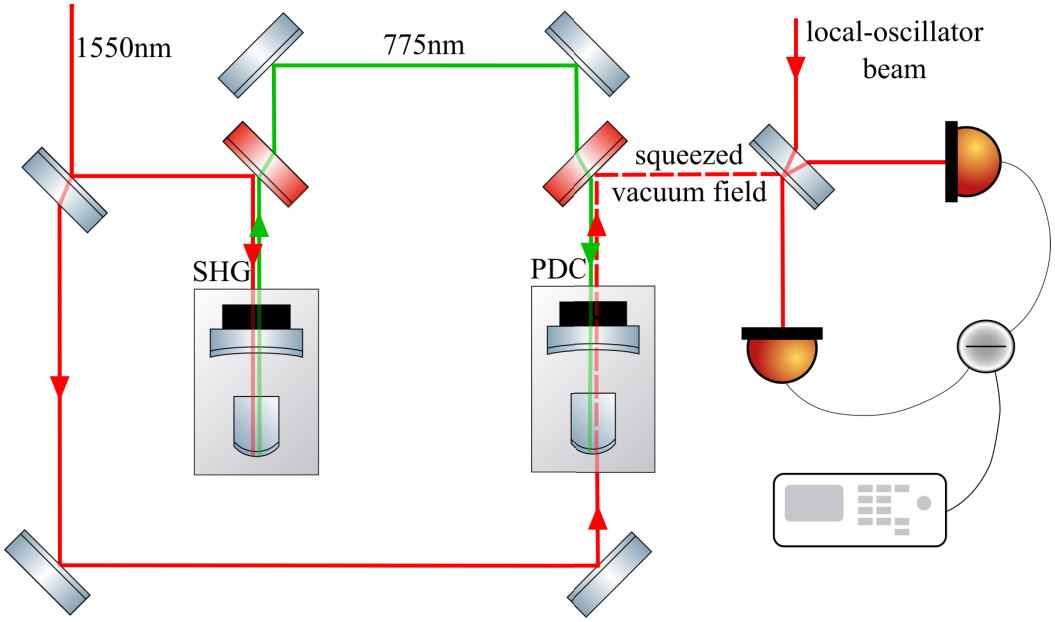

Figure 4.9: The setup of the squeezed-light source: The 1550 nm light was converted to 775 nm in the SHG resonator and a dichroitic mirror separated both fields. The converted light served as a pump field entering the PDC resonator through the coupling mirror. The generated squeezed states left the resonator on the same side and were also separated from the incoming light with a dichroitic mirror. They overlapped with the local-oscillator field on the beamsplitter of the balanced homodyne detector. The 1550 nm light entering the PDC resonator through the crystal was only necessary for the adjustment and was blocked during the squeezing measurement.

ror with high reflectivity for 1550 nm. With the same SHG resonator a conversion efficiency of 99.5 % could be achieved for an input power of 1.1 W [38]. Due to the double resonance of the PDC cavity much less frequency-doubled light was required to generate high squeezing values. With an input power of 260 mW for the SHG, a conversion efficiency of 57 % was reached and 147 mW of light with 775 nm was generated.

A light field with 1550 nm was sent through the back of the PDC resonator. As the resonator was strongly overcoupled, even on resonance only a power of 0.65 mW of the input power of 635 mW was transmitted. This field, from now on called the *adjustment field*, was used to build the optical path of the squeezed vacuum states to the balanced homodyne detector and to adjust the mode overlap with the local-oscillator field. This procedure is explained more detailed in section 6.3.

For the actual squeezed-state generation the adjustment field was blocked and the PDC cavity was pumped with the frequency-doubled light. The produced squeezed

vacuum states left the resonator through the coupling mirror and were reflected by another dichroitic mirror. On the balanced beamsplitter they interfered with the local-oscillator field for the balanced homodyne detection. The difference between the currents of the two photodiodes was built electronically and the resulting output served as signal for the spectrum analyzer to measure the relative noise power. With two lenses each, the modes of the light fields were matched to the resonators. Their positions were calculated with the software *JamMt* by André Thüring and Nico Lastzka.

To stabilize the lengths of the SHG and the PDC resonators, Pound-Drever-Hall control feedback loops were applied [75]. For this technique, the beam passes an electro-optic modulator to generate sidebands to the carrier frequency before the light is coupled into a resonator. If the cavity fulfills the resonance condition for the carrier frequency, the side bands and in the non-impedance-matched case also a part of the carrier light are reflected. At resonance the carrier and the sidebands have the same phase. If the resonator drifts away from the resonance, also phase shifted carrier light is reflected and overlaps with the sidebands. The resulting phase modulation of the reflected light can be measured as an amplitude modulation with a photodiode. Demodulating the photodiode signal with the modulation frequency results in an error signal, that can be used for a feedback loop keeping the resonator length stable.

For the stabilization of the SHG resonator, sidebands at a frequency of 119 MHz were generated on the carrier light using a free space electro-optic modulator. A 1550 nm photodiode in transmission was used to receive the error signal. To stabilize the PDC resonator, two control loops were set up. When the adjustment field was used, the resonator was stabilized using a resonant 1550 nm photodiode in reflection of the crystal. The frequency-doubled light still carried the frequency modulation, such that the PDC cavity could be stabilized with the sidebands on the 775 nm light, when the cavity was pumped to generate squeezed states. For this purpose a resonant photodiode in reflection of the coupling mirror was used.

5 The Sensitivity Enhancement of Interferometric Measurements with Internally Produced Squeezed States

As signals caused by classical radiation pressure forces are quite weak, the sensitivity enhancement of interferometric measurements for gravitational-wave detectors and other optomechanical experiments is a meaningful matter. The application of signal-recycling or power-recycling cavities results in a signal increase, but is accompanied by a bandwidth decrease. Different techniques using nonlinear media and squeezed states can be used to overcome the following standard sensitivity-bandwidth limit. In this chapter the approach of internally produced squeezed states will be demonstrated [24]. The concept for the presented measurements was developed by Mikhail Korobko, with whom I executed the experiment, using my setup presented in chapter 4. The results were published in [33].

5.1 The Standard Sensitivity-Bandwidth Limit

In many current interferometric measurements, such as gravitational-wave detectors, cavities for power-recycling and signal-recycling are implemented. Such signal-enhancing techniques are applied as the phase-modulation signals on the light field are very weak and therefore challenging to detect. The consequence of such cavities is a reduction of the detection bandwidth depending on the cavity's finesse.

According to [76] the standard sensitivity-bandwidth limit is set by the product of the peak sensitivity S and a detection bandwidth B for a defined light power P inside a resonator using coherent states:

$$S \cdot B \leq \frac{8\pi P}{\hbar \lambda l} \ . \tag{5.1}$$

Here l is the resonator length, λ is the wavelength of the light and $\hbar$ is the reduced Planck constant. [77]

5.2 The Concept of Internal Squeezed-Light Generation

Different approaches to improve the sensitivity of an interferometer with a cavity are discussed and in usage. One of them is the so called *white-light-cavity* effect as

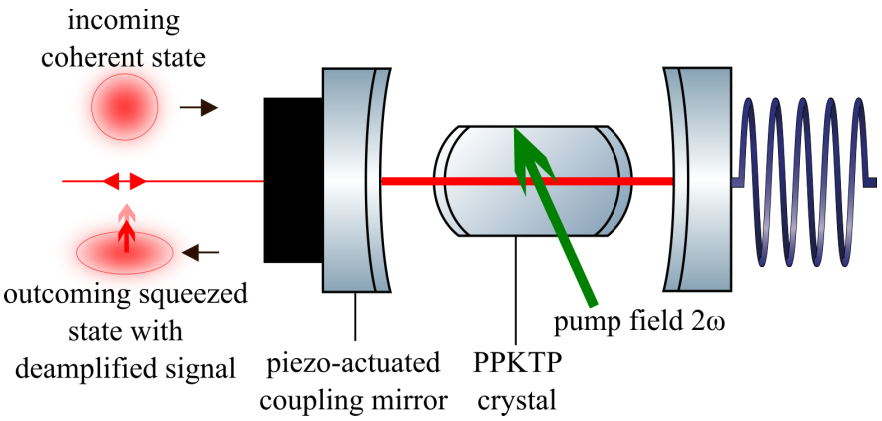

Figure 5.1: Illustration of the internal squeezing approach: The Fabry-Perot cavity has a nonlinear crystal inside, which is pumped with frequency-doubled light to induce the degenerate parametric down-conversion. In addition a field with the fundamental frequency is used to measure a phase-modulation signal caused by a force on the mirror. Squeezed states are produced and the generated signal is deamplified. As this deamplification is limited, the sensitivity-bandwidth product is enhanced.

for example described in [23]. It is suggested to place a nonlinear medium between the mirrors of the signal-recycling or power-recycling cavity, that can cancel out the frequency-dependent change of the wavelength. The realization however requires to find a suitable medium with the desired properties and a high-power laser system, that is very stable in amplitude and frequency. A second approach is the injection of squeezed states produced by an external source as suggested in [40] and applied in [78] to decrease the noise of the light field in the phase quadrature. This technique was also applied on the presented Michelson-Sagnac interferometer and will be discussed further in section 6.3.

In contrast to the injection of externally produced squeezed states, it is suggested to produce them directly inside a cavity of a detector by placing a nonlinear medium between its mirrors and inducing the squeezed-state generation with pump light [24]. As the squeezing happens inside the linewidth of the cavity, not only the noise but also the signal is degraded. For an improvement, the phase noise shall be reduced, which results in an increase of the amplitude noise. With this approach the sensitivity-bandwidth product can be increased. Mikhail Korobko and I performed a proof-of-principle experiment, that is presented here.

The starting point of the setup is a Fabry-Perot cavity to measure a phase modulation caused by a weak force onto one end mirror using a field with the fundamental fre-

quency. The concept is illustrated in figure 5.1. A nonlinear crystal within is pumped with frequency-doubled light to induce the degenerate parametric down-conversion for the squeezed-state generation. Inside the cavity the squeeze factor is limited to 6 dB (compare 4.3.1) at the resonance frequency. Because of the destructive interference of the squeezed field with the bright coherent light, the squeeze factor of the outgoing field is not limited, such that higher squeeze factors can be reached for the vacuum noise. In contrast, the signal is generated inside the resonator, such that the 6 dB limit for its deamplification can not be overcome. The fact, that the noise squeezing is not limited but the signal deamplification is, leads to a gain of the ratio between them and therefore to an enhanced displacement spectral density. As the sensitivity increase due to the squeezed states only occurs inside the cavity linewidth, the measurement bandwidth is reduced. Nevertheless, the amplification of the amplitude uncertainties inside the resonator causes an enhancement of the sensitivity-bandwidth product.

5.3 The Modified Squeezed-Light Source for the Demonstration of Internal Squeezed-Light Generation

To test the described concept, the squeezed-light source from figure 4.9 was modified as illustrated in figure 5.2. The same PDC resonator was used, but in this case it did not only have the purpose of squeezing vacuum states, but also to act as a Fabry-Perot cavity comparable to a signal-recycling or power-recycling cavity of an interferometer. With a broadband fiber-coupled electro-optic modulator, a signal was generated on a 1550 nm field, that was sent through the back of the resonator. This way, a phase-modulation signal produced by a weak mechanical force on an end mirror was imitated. The advantage of an externally produced signal was the option of tuning its frequency and therefore the observation of the resulting change in the detection bandwidth. The PDC resonator was pumped with frequency-doubled light with a wavelength of 775 nm produced by the SHG resonator.

The length of the resonator was stabilized with the Pound-Drever-Hall technique [75] as described in section 4.3.2. With a free space EOM the therefore needed sidebands were generated on the initial beam. Two options were given in the experiment to generate the error signal. The length could be stabilized with the pump field by measuring the backreflected 775 nm light with a resonant photodiode and demodulating the photocurrent. When the pump field was blocked, the backreflected 1550 nm beam with sidebands at the same frequency was detected in reflection on the other side. The

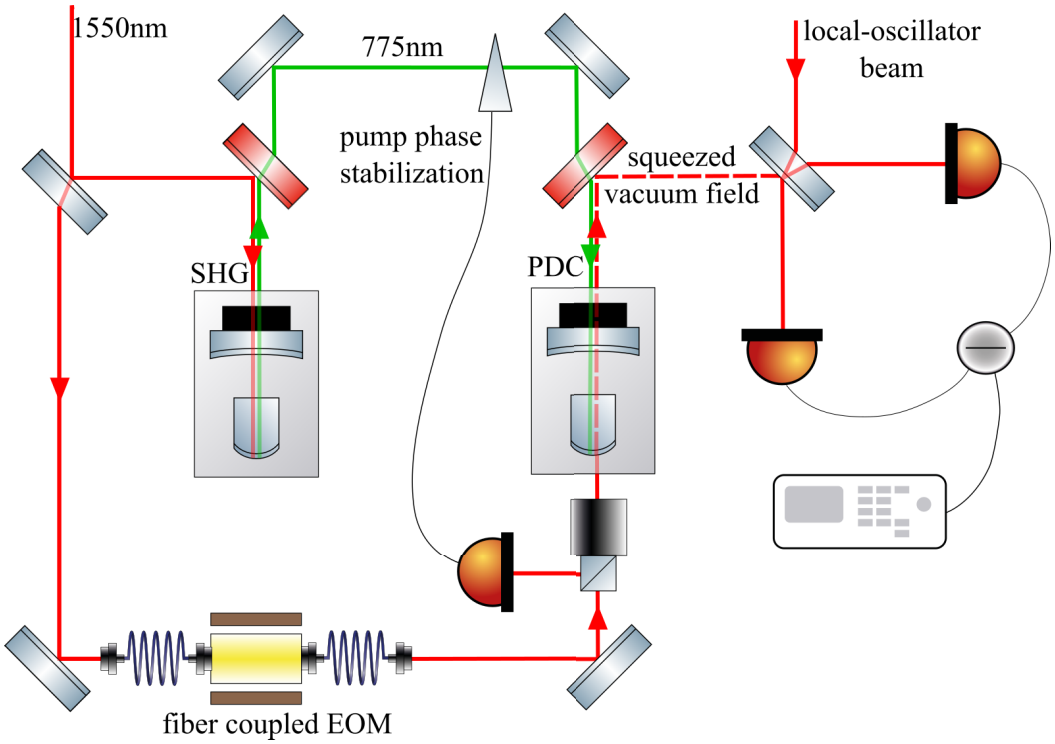

Figure 5.2: The modified squeezed-light source for internally generated squeezing: A fiber-coupled EOM was added to the setup. The modulated light with wavelength 1550 nm was injected from the back of the PDC resonator to simulate an optomechanical signal. Simultaneously the frequency-doubled pump light with wavelength 775 nm entered the cavity through the coupling mirror. The phase of the signal field was stabilized to the phase of the pump light using the backreflected signal light. In contrast to the setup in section 4.3.2, now a bright light field of the fundamental wave length was inside the resonator while squeezed states were generated.

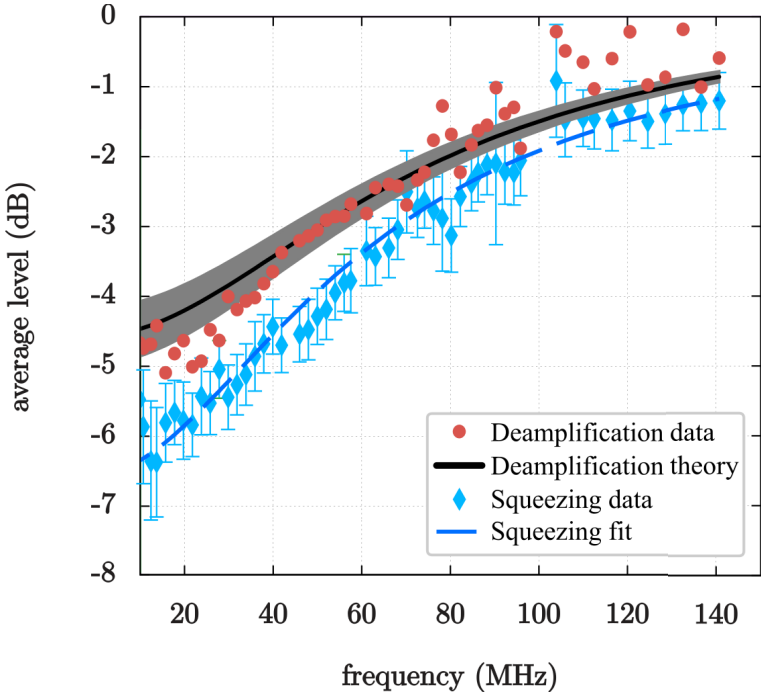

Figure 5.3: Using internally produced squeezed states to overcome the standard sensitivity-bandwidth limit: The squeezing and deamplification was plotted against the measurement frequency. The detection efficiency for the shown data series was $\eta^2 = 0.82$. The squeezing model was fitted to the measured frequency dependent squeeze factor. The signal deamplification was above the corresponding squeezing over the whole frequency range. The theoretical deamplification calculated from the squeezing values is given by the black line. Its error estimated from the data is shown by the grey area. This data was published in [33].

phase between the two fields inside the resonator was stabilized with another feedback control loop. For this purpose an error signal was generated by detecting the reflected signal light. The phase was controlled with a piezo-actuated mirror in the pump field path.

The output signal of the cavity was detected with a highly efficient broadband balanced homodyne detector. The electronics were designed and built by Stefan Ast in his PhD thesis [79]. In the frequency range of the presented measurements from 10 MHz to 140 MHz it showed a dark noise clearance of ≈ 13 dB.

5.4 Beating the Standard Sensitivity-Bandwidth Limit with Internally Produced Squeezed Light

To measure the impact of the internally produced squeezed states over the measurement bandwidth, a series of spectra was recorded. Using the fiber-coupled electro-optic modulator, signals at different frequencies between 10 MHz and 140 MHz were generated. For each frequency initially the resonator was stabilized with the 1550 nm light and the output signal of the resonator was measured with the balanced homodyne detector without pump light. Then the pump light was added, the resonator was stabilized with the 775 nm light and the output signal was measured again. This approach allowed to compare the signal and the noise without and with internal squeezing directly. The resulting values for the squeeze factor and the deamplification are plotted against the signal frequency in figure 5.3.

By analyzing the squeezed and antisqueezed noise in the spectrum the coupling mirror power transmission, the internal loss L and the detection efficiency η^2 were calculated. The simulations in [33] resulted in an upper bound for the eternal loss of $L \leq 0.23\,\%$ and a corresponding roundtrip-loss bandwidth of

$$\gamma_l = \frac{cL}{4l} \leq 2\pi \cdot 743\,\mathrm{kHz} \tag{5.2}$$

with l being the cavity length. This value conforms to absorption measurements for PPKTP [80] and to the transmission values for the coupling mirror and the antireflective coating of the crystal as specified by the manufacturers. The following fitted squeezing model given as blue dashed line is in agreement with the data. The experimental parameters were used to estimate the theoretically expected deamplification of the signal, that is given in by the black line. The grey area around it shows the estimated error bar following from the measurement. Over the whole frequency range the deamplification was above the squeeze factor. For the shown data set followed a detection efficiency of $\eta^2 = 0.824$.

The experiment was performed four times with varying detection efficiencies η^2. The measured reached squeeze factors are plotted against the resulting enhancement in figure 5.4. In addition the theoretical models of this dependence are given for the different detection efficiencies. It shows that for each detection efficiency, there exists an optimum squeeze factor for a maximum enhancement.

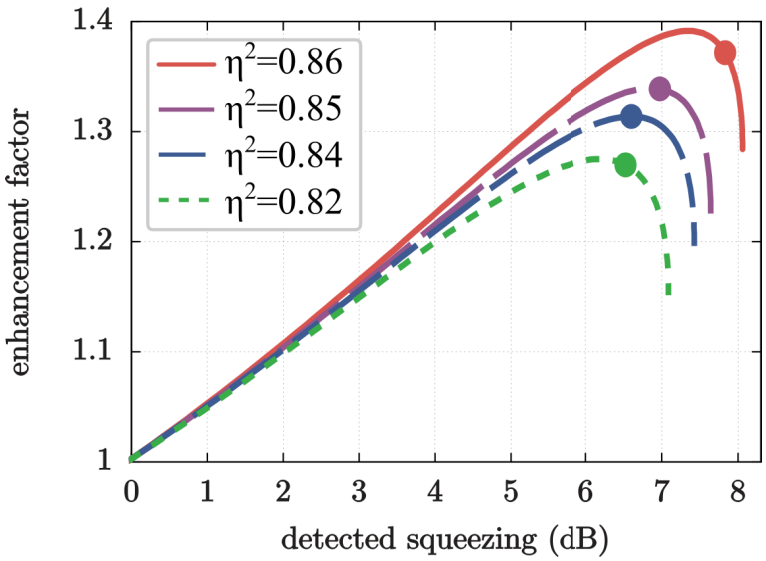

Figure 5.4: The detection-efficiency dependent enhancement factor: Four data series like the one shown in figure 5.3 with different detection efficiencies η^2 were recorded. The values for the detection efficiencies followed from the squeeze and anti-squeeze factor reached for the measurements. The dots show the reached enhancement factors depending on the detected squeezing value. The theoretical curves demonstrate the existence of an optimum squeeze factor for each η^2 to reach the enhancement maximum. The maximal measured enhancement was 36 %. This data was published in [33].

The measured data of noise squeezing and signal deamplification showed a maximal enhancement of the sensitivity-bandwidth product of 36 %. Considering the error of the measured values for the squeezing and deamplification, the experimental results are consistent with the theoretical estimations. An explanation for discrepancies could be observed electronic resonances of the homodyne-detector electronics and the used wires.

The concepts of the white-light-cavity effect and the injection of externally produced squeezed states have been proven to enhance interferometric measurements in the past. The results of the presented experiment demonstrate the possible enhancement of laser interferometers with cavities using a third approach, the application of internal squeezed states. Because of the accompanying deamplification of the signal when the squeezed states are produced internally, the injection of externally produced states is still the more efficient concept to improve the signal-to-noise ratio. But it should be noted, that the sensitivity to intra-cavity loss is lower for the internal-squeezing approach. Nevertheless, in principle the maximum improvement could be reached by applying all three techniques in one interferometer.

The Michelson-Sagnac interferometer, which is the main focus of this dissertation, has currently no cavities, which could allow an enhancement by producing internal squeezed states. In section 6.3 the injection of externally produced states is presented, the results are shown in section 7.4. The plan of implementing a signal-recycling cavity in the future is described in section 8.4.

6 The Realization of a Michelson-Sagnac Interferometer at Low Temperatures with Injected Squeezed States

The topology of the Michelson-Sagnac interferometer was introduced in section 3.2. In this chapter the actual table top experiment will be presented. The contributions of the thermal noise to the total noise were estimated in section 3.4.1. It showed that the aspired radiation-pressure-noise dominated sensitivity of the Michelson-Sagnac interferometer can only be observed when it is cooled. For this reason the setup was placed inside a cryostat, whose functionality is described. The interferometer needed to be designed and built such, that it can be operated at low pressure and low temperatures.

By optimizing the interferometer contrast, the impact of technical laser amplitude noise and optical losses were minimized. This was required to enhance the sensitivity by injecting squeezed states into the interferometer through the output port [34][38][39][81][67].

6.1 Operating the Interferometer at Low Temperatures

6.1.1 The Cryogenic System

Because of the high impact of the thermal noise on the sensitivity of the Michelson-Sagnac interferometer, the experiment needed to be cooled to observe radiation pressure noise in the future. The cryostat and the interferometer were set up by Andreas Sawadsky during his PhD thesis [34] at the AEI Hannover. Afterward we moved the experiment to the ILP Hamburg where I continued the work with the help of Pascal Gewecke, who wrote his master thesis [81] on this project.

At first, a vacuum system was installed. At atmospheric pressure, an effect of gas damping the oscillations of the membrane occurs. With a pressure of below 10^{-6} mbar in the used vacuum system this could be neglected [44]. Also the later presented room temperature measurements were taken under vacuum. A scroll pump provided a pre-vacuum pressure of 10^{-2} mbar. A turbo pump was used to reach the end pressure of 10^{-6} mbar at room temperature. Residual gas inside a vacuum chamber increases the heat transfer from its outer surfaces to the components inside. Thus, by operating the system at low pressures, lower temperatures could be reached with the cryogenic

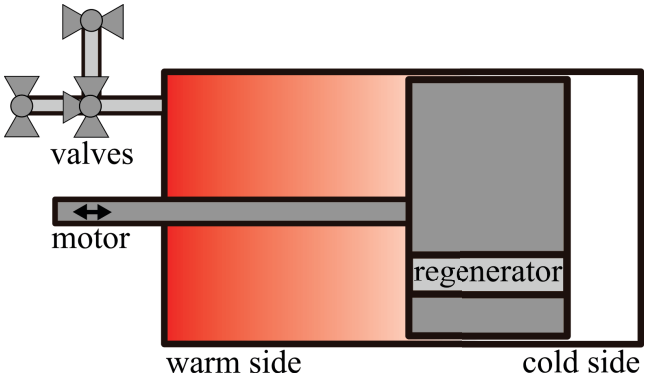

Figure 6.1: Functionality of the regenerator for the Gifford McMahon cycle: The volume is divided into a cold and a warm side, separated by a piston with a passage, that the gas inside can flow from one side to the other. Through the valves warm gas leaves the cycle and new gas enters for the cooling process.

system. At cryogenic temperatures an end pressure of 10^{-7} mbar was reached.

The used cryogenic system, a CCS-xg-CH204N by *Janis Research company Inc*, was designed to achieve a temperature of 10 K. The cryostat worked with the Gifford McMahon principle, which is a regenerative process. It bases on the flow of a gas through a regenerative heat exchanger, a material with high specific thermal capacity, which separates the cold and the warm side of a volume. The basic setup is shown in figure 6.1. The gas is compressed by the regenerator and the produced heat is let into the warm side of the volume. Flowing through a passage in the regenerator, the gas emits its heat. On the other side, the cold part of the volume, it expands and thus detracts warmth from the environment. Afterward it flows back through the passage, absorbing the previously emitted heat and leaving the volume though one of the valves. Through the other valve new gas enters the volume. By repeating the described steps, more and more warmth is carried out of the cold part of the volume [82].

This specific refrigerator system functioned with a closed cycle between a helium-4-compressor and a cold head, which had two cooling stages. The process happened in a cylindrical volume with a piston inside, that was driven by a motor and contained the regenerator. The helium, which acted as exchange gas, did not leave the volume of the cylinder. The cold head was connected to the compressor with a high and a low pressure side, that could be opened and closed separately to periodically repeat the steps of the Gifford McMahon cycle. The chamber contained the so called *cold finger*, which made the contact to the experiment, that was hanging upside down from the lid

of the chamber. Additionally a polished heat shield formed a second layer between the experiment and the vacuum tank to avoid heat radiation from the outside warming up the setup. The cooling happened in two steps. On the first stage a temperature of 77 K was reached, the second stage cooled the sample holder down to 10 K. A more detailed description can be found in [70] and [34].

When an experiment is cooled down, residual moisture from the air condenses on the surfaces of the optics, decreasing their quality and leading to optical losses and in this case to a lower interferometer contrast. Condensed water on the surface of the membrane reduces its quality factor. To avoid such effects, it was necessary to reach a low vacuum pressure before starting the cooling process. By heating the interferometer with an internal heater during the beginning of the cooling, it was assured, that any remaining moisture condensed on the surface of the heat shield in the cryostat instead of on the interferometer parts.

6.1.2 The Interferometer Design for Low Temperatures

The concept of the Michelson-Sagnac interferometer (MSI) with silicon nitride membrane was introduced in section 3.2. The spacer for the MSI was designed by Andreas Sawadsky. Its development process is described in his PhD thesis [34]. Several requirements had to be met for a successful performance at low temperatures. The membrane's linear position in the propagation direction of the beam needed to be tunable to switch between the bright and the dark fringe of the interferometer. To achieve a good adjustment at low temperatures, the used materials should ideally have a low thermal expansion coefficient. Nevertheless, experiences have shown that even using a material with low deformation, the contrast could not be kept high enough during the cool-down. In consequence not only the membrane's linear position, but also its orientation and both steering mirrors needed to be adjustable at low temperatures. For high precision interferometric measurements, avoiding mechanical vibrations was crucial. Therefore it needed to be assured, that the resonance frequencies of the used components were not within the measurement range and that the experiment was isolated from acoustic noise from the outside as good as possible. Besides the mentioned points, also a minimization of the heat exchange with the environment needed to be considered.

The membrane was glued onto a holder. Its material of choice was copper because of its good heat conductance to avoid a heating of the membrane. Additional copper

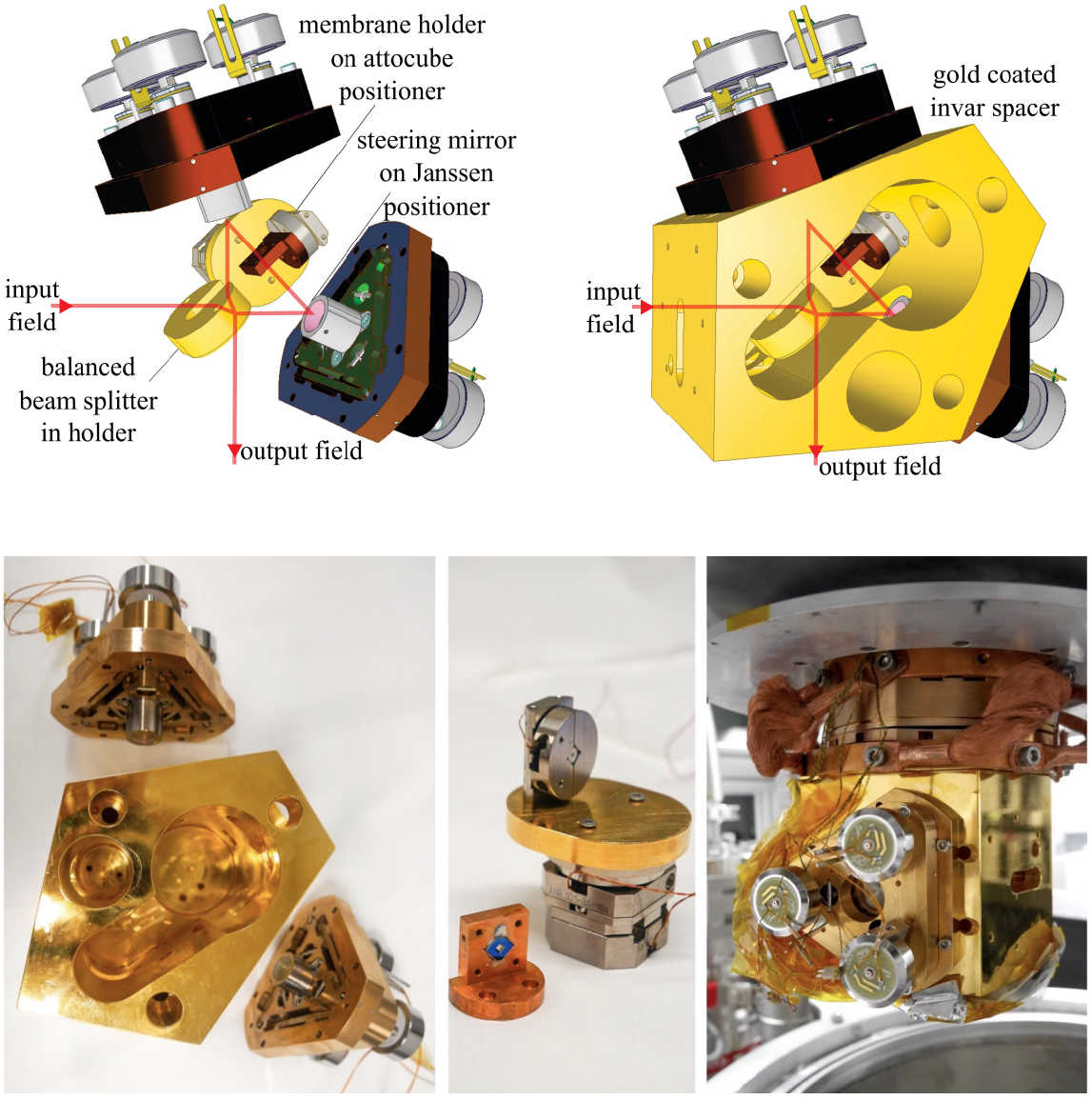

Figure 6.2: Realization of the Michelson-Sagnac interferometer for cryogenic temperatures: The membrane was glued onto a copper holder, that was screwed onto a stack of positioners by the company *attocube* [83]. They allowed an adjustment of the membrane in the xy-plane as well as a linear shift along the beam axis via an electric controller. The steering mirrors were attached to triangular positioners by the company *Janssen Precision Engineering* [84]. The screws on the three edges of these devices could be also controlled via an electric controller, such that the mirrors could be adjusted. All components were screwed onto a spacer made of Invar. To increase the reflectivity of the setup for heat radiation, the spacer was coated with gold. The complete setup hung upside down from the vacuum chamber lid. An additional damping stage reduced vibrations coupling into the experiment from the outside. Copper braids bridged the spacer and the cold plate to avoid a thermal isolation due to the damping stage.

wires connecting the copper holder to the cold plate increased the heat transfer even further. The holder was attached to a stack of three cryogenic positioners by the company *attocube*. These allowed the adjustment of the linear position in propagation direction of the beam and of the vertical and horizontal angle of the membrane. In figure 6.2 the stack with the membrane attached to the holder is visible in the middle of the setup.

The beamsplitter was not adjustable. The steering mirror holders were attached to the so called *Cryo Linear Actuators* by the company *Janssen Precision Engineering*. In figure 6.2 they are shown with the mirrors as part of the interferometer setup. These positioners were designed to be stiff and insensitive to vibrations as resonance frequencies of mirror holders have been an issue in previous interferometer designs as described in [34]. The three screws to adjust the mirrors in the xy plane could be operated with step sizes of down to 5 nm at 4 K. The total range was ± 1.5 mm. The monolithic triangular main body was made of bronze to guarantee the reset force of the springs. The sockets holding the mirrors were made of Invar. Because of its very low thermal expansion coefficient, Invar was the material of choice to minimize deformation during the cooling to cryogenic temperatures. As the fused silica mirrors had a very low contraction when they were cooled, using a material with similar properties, minimized stress on them [34].

The mentioned components were all screwed onto a spacer as shown in figure 6.2. The chosen material for the block was again Invar due to its very low thermal expansion coefficient. The shape was designed as symmetric as possible to reduce deformation during the cooling. It was based on the concept by Morten Steinecke for a monolithic Michelson-Sagnac Interferometer design. He simulated the low thermal deformation in his bachelor thesis [85]. To avoid a warming due to heat radiation from the environment, the reflectivity of the block and of the beamsplitter holder was increased by coating them with gold. The design provided the option to attach a third *Janssen* positioner to implement a signal-recycling mirror in the future. Two thermometers, one at the cold plate and one at the copper membrane holder, were implemented.

The interferometer was screwed upside down to the sample holder of the cryostat. To reduce vibrations from the outside coupling into the interferometer, an additional damping stage by the company *Janssen Precision Engineering*, the *Cryo Vibration Isolation Platform*, was implemented. It was made of bronze which acts well as a

spring material for low temperatures. The stage was designed to reduce vibrations coupling into the experiment with a low cut-off frequency. Simulations described in [34] estimated a suppression of $-40\frac{\mathrm{dB}}{\mathrm{decade}}$ above the cut-off frequency of 41 Hz for the vertical direction. A disadvantage of the stage was its thermal isolation between the interferometer spacer and the cryostat. To bridge the heat flow, soft copper braids leading to the cold plate were attached to the interferometer. On the bottom right of figure 6.2 the damping stage and the copper braids are visible.

6.1.3 The Impact of the Heat Flow through the Wires

The original vacuum chamber was replaced by a bigger one, as its original volume turned out to be too small. To cool a bigger volume with the same cooling power, the heat flow into the cryostat needed to be kept as low as possible.

The *attocube* and *Janssen* positioners were adjustable from the outside of the interferometer using controllers from the companies. The cables for the connections needed to be suitable for cryogenic temperatures and have a resistance below $10\,\Omega$ over the whole length to assure that the positioners work properly. In total 12 wires were used for the steering mirror positioners, 6 for the membrane positioners and 4 for the two thermometers. The electric feedthroughs of the cryostat provided to route 45 cables into the cryostat. In the beginning, copper cables were used, but due to their good heat conductance properties, too much warmth got led to the experiment. For an empty cryostat without cables, a minimum temperature of 8.5 K could be reached within 7-8 hours. After implementing the cables, it took 3 days to reach a temperature of 13 K. As a consequence the cryostat could not provide enough cooling power to reach low temperatures anymore [34].

The copper cables had a thermal conductivity of $\lambda_{\mathrm{Cu293-77}} = 417\frac{\mathrm{W}}{\mathrm{mK}}$ for the temperature range of the first cooling stage from 293 K to 77 K and a thermal conductivity of $\lambda_{\mathrm{Cu77-10}} = 974\frac{\mathrm{W}}{\mathrm{mK}}$ for the temperature range of the second cooling stage from 77 K to 10 K. Each cable had had a cross section of $0.032\,\mathrm{mm}^2$. According to [34] the heat flow for a solid bar from one surface with the area A to the opposite surface is

$$\dot{Q}_{\mathrm{cond}} = \lambda(T) A \frac{dT}{dx} \tag{6.1}$$

with the temperature-dependent thermal conductivity $\lambda(T)$. The temperature difference to the first cooling stage compared to room temperature was $300\,\mathrm{K} - 77\,\mathrm{K}$ and

the length of the wire in this stage was $dx = 20\,\mathrm{cm}$. The resulting value for the heat flow per wire for the first cooling stage calculated as

$$\dot{Q}_{\text{cond, Cu},293-77} = 14.4\,\mathrm{mW}\ . \tag{6.2}$$

A length of $dx = 80\,\mathrm{cm}$ of the wire led through the second stage. Accordingly the heat flow was:

$$\dot{Q}_{\text{cond, Cu},77-10} = 2.6\,\mathrm{mW}\ . \tag{6.3}$$

To reduce the heat flow to the sample holder, the copper cables were exchanged with bronze-phosphor cables, the so called *Duo-Twist* cryogenic wires by the company *Lake Shore Cryotronics Inc.* The cross section of each wire was $0.032\,\mathrm{mm}^2$. The value for the cooling to the first stage was assumed to conform to the specified value for the thermal conductivity at room temperatures, such that $\lambda_{\mathrm{PB}293-77} = 417\frac{\mathrm{W}}{\mathrm{mK}}$. This was a very conservative estimation as the thermal conductivity decreases with decreasing temperatures. For the second stage the specified value for 77 K was used: $\lambda_{\mathrm{PB}77-10} = 25\frac{\mathrm{W}}{\mathrm{mK}}$. For the same cable length of 1 m with 20 cm in the first and 80 cm in the second stage, the heat transfer per cable for the first stage was

$$\dot{Q}_{\text{cond, PB},293-77} = 1.7\,\mathrm{mW} \tag{6.4}$$

and for the second stage

$$\dot{Q}_{\text{cond, PB},77-10} = 0.27\,\mathrm{mW}\ . \tag{6.5}$$

Due to this strong heat flow reduction, the cooling performance could be improved and again a temperature of 8.5 m K was reached for an empty chamber with cables leading inside.

6.2 The Setup, Adjustment and Readout of the Michelson-Sagnac Interferometer

6.2.1 The Experimental Setup

The described Michelson-Sagnac interferometer in the cryostat formed the core of the table top experiment. The adjustment was mostly done from the outside when the tank was closed. It was aspired to reach a contrast as high as possible to reduce optical losses and to minimize the impact of laser amplitude noise. In the experiment as shown in figure 6.3, the laser light transmitted through a triangular mode-cleaning resonator to provide a clean TEM_{00} mode. The resonator is from now on called *pre*

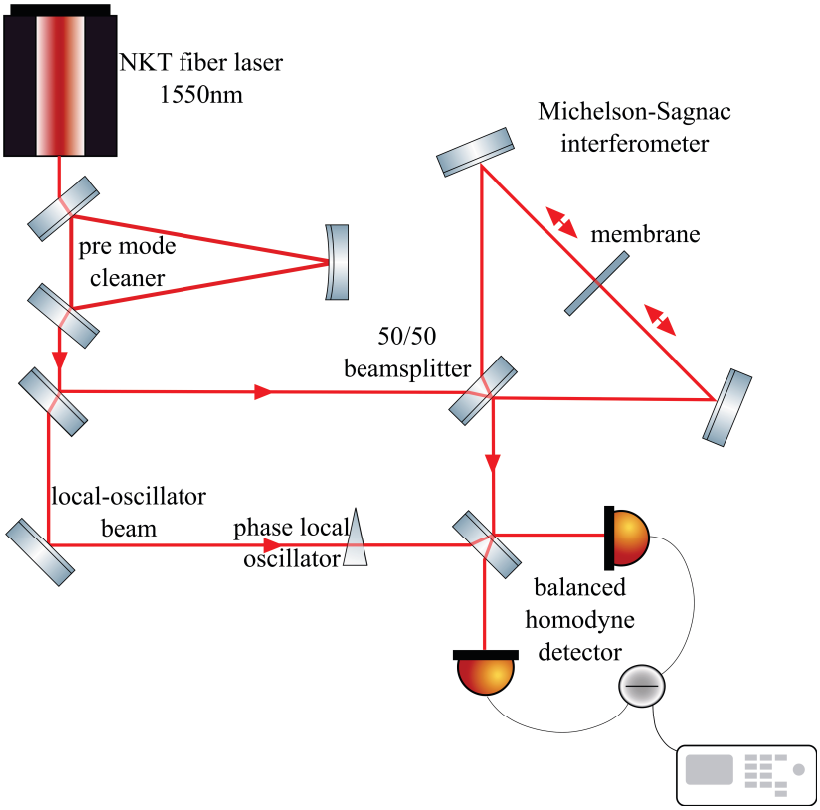

Figure 6.3: The Michelson-Sagnac setup in the table top experiment: The laser beam was filtered by the pre-mode-cleaner cavity to provide a clean TEM_{00} mode. With a beamsplitter, the light was split up into the input light for the interferometer and the local-oscillator light. The output field of the interferometer interfered with the local oscillator at the homodyne detector, which is described in section 4.2.1. The phase between the fields determined the readout angle.

mode cleaner (PMC). The outcoming beam was split up into the interferometer input beam and the local oscillator. On the beamsplitter of the homodyne detector the output beam of the interferometer and the local-oscillator beam interfered and the two resulting fields hit the two photodiodes. The principle of balanced homodyne detection is explained in section 4.2.1. A mirror attached to a piezo-electric actuator served as a phase shifter to control the phase between the two fields. The output of the homodyne detector, the subtraction of the two photocurrents, was measured with a spectrum analyzer.

6.2.2 Optimizing the Michelson-Sagnac Interferometer Contrast

As the influence of the laser amplitude noise on the total-noise spectral density of the interferometer depended on the output power, an optimization of the contrast was crucial for a quantum-noise dominated sensitivity. The higher the contrast of the modes was, the lower was P_{out} at the dark fringe. As the interferometer was inside the vacuum tank, the beam paths could not be checked by eye and the transmitted and back reflected light was the only reference point. All components relevant for the adjustment process are shown in figure 6.4.

The first step before assembling the whole interferometer was to determine the angle of the beamsplitter for the optimum balancing. For this purpose only the beamsplitter was attached to the interferometer spacer. With a powermeter the reflected power and the transmitted power for a straight incoming beam were measured and the spacer was rotated to achieve the ideal position. For an angle of 45.5° a perfect balancing of $\Delta_{\mathrm{bs}} = |r_{\mathrm{bs}}^2 - t_{\mathrm{bs}}^2| = 0 \pm 0.01$ was achieved. The error was caused by the powermeter.

Afterward the positioner stack with the membrane holder and the membrane, as well as one steering mirror with its positioner were mounted. Using the two mirrors in front of the vacuum tank and the steering mirror positioner, the beam was adjusted such, that the reflected beam hit the membrane in the middle and exited the spacer through the hole for the missing mirror in the center. Then the second steering mirror was mounted to complete the interferometer. With a ccd camera four spots became visible in the output. By moving the positioners for the membrane and the steering mirrors, these modes were overlapped.

For the further adjustment of the contrast, two photodiodes were used. One was placed at the output to measure the transmission, one behind the pre-mode-cleaner

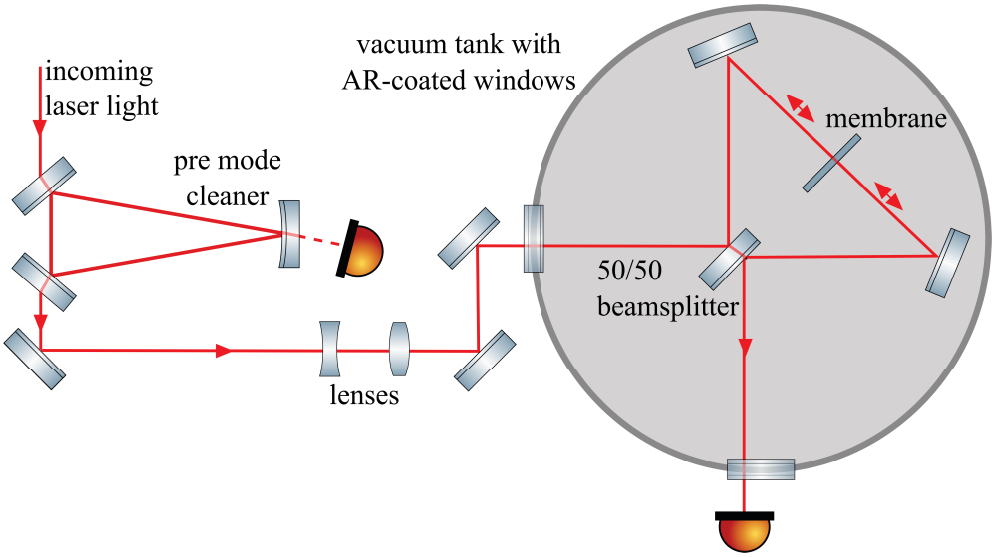

Figure 6.4: The components for the interferometer adjustment process: Two lenses determined the incoming beam's waist size and linear waist position. The two mirrors in front of the vacuum tank were used to adjust the beam's position and orientation. Two photodiodes, one behind the pre-mode-cleaner cavity, one at the interferometer output, were used to measure the reflected and transmitted power. The two steering mirrors inside the tank and the membrane were adjustable with electronic controllers. The position of the beamsplitter was fixed, its angle could only be adjusted by turning the whole interferometer.

cavity to measure the reflection of the interferometer. During the adjustment process, the membrane position was scanned by applying a triangular voltage on the linear membrane positioner with a function generator. The ratio between the maximum and minimum voltage measured with the output photodiode

$$C = \frac{V_{\max} - V_{\min}}{V_{\max} + V_{\min}} \tag{6.6}$$

determined the contrast.

At first the overlap of the Sagnac mode was optimized. To measure the Sagnac mode separated from the Michelson mode, the membrane was slightly tilted with its positioner, such that the photodiodes only detected the light transmitted by the membrane. In the case of a perfect Sagnac interferometer, the output photodiode should measure zero. All the light would be reflected back to the pre-mode-cleaner cavity, such that a maximum on the photodiode behind is reached. This could only be realized when the waist of the beam was exactly in the middle of the interferometer. The positions for the needed lenses were calculated with the software *JamMt* by André Thüring and Nico Lastzka. The chosen waist size had to be much smaller than the membrane to avoid hitting the membrane frame. A waist diameter of 270 μm was measured with a beam analyzer.

By shifting the lenses, by tilting the steering mirrors inside the interferometer and by adjusting the mirrors in front of the vacuum tank, the reflection signal was maximized. When the membrane was tilted back afterward, the Michelson mode was added to the signal again and a sinusoidal signal appeared on top of the Sagnac signal in reflection. In transmission almost only the Michelson signal was measured. After optimizing the contrast of the Michelson mode with the two steering mirrors, the residual Sagnac mode showed as flat signal.

For a good Michelson contrast the beam waist needed to be positioned on the membrane. Thus, for an already well adjusted Sagnac mode, the membrane was shifted linearly with its positioner to the point where the highest contrast could be achieved.

During the process several challenges and limitations occurred. When the membrane was tilted to measure only the Sagnac mode, the path was slightly misaligned due to the refraction in the material. When the Sagnac overlap was only adjusted with tilted

membrane, the reached contrast was not optimal. Therefore the fine adjustment had to be done when both modes were overlapping.

To avoid clipping on the membrane frame, the waist size needed to be much smaller than the membrane. But the consequence was high divergence and a bigger beam size on the steering mirrors, the beamsplitter and the vacuum tank windows. The waist size had to be chosen such, that clipping at these other components was avoided. Therefore a trade-off between a small waist on the membrane and too high divergence causing clipping of the beam at other optics had to be made.

The minimum power reflection of the antireflective coating of the beamsplitter was 170 ppm (parts per million) for an angle of 45°. For the angle of best balancing of 45.5° it was 260 ppm [34]. It followed that the power of the light reflected by the coating could not be neglected. It left the interferometer as a low power beam next to the signal beam and could be cut off using a pinhole.

As the frame of the membrane was also transmissive for the used wavelength, it was not always obvious in the adjustment process if the beam hit the frame or the membrane. To verify that the beam hit the membrane, the ratio between the light power in the Sagnac mode and in the Michelson mode turned out to be a good indicator. As the silicon frame acted as a resonator, its reflectivity and transmission were dependent on the wavelength. When the wavelength was shifted and the heights of the signals stayed constant, the light hit the membrane. When they changed, it hit the frame.

Figure 6.5 shows the resulting interference fringes of the optimized contrast for an in linear direction scanned membrane displacement. On the left the measured signal of the photodiode in reflection is shown. The Sagnac mode appeared as a flat signal, the sinusoidal signal on top shows the Michelson mode. From the ratio between these two, it followed a power reflectivity of the membrane of

$$r_{\mathrm{m}}^2 = 0.19 \pm 0.005 \ . \tag{6.7}$$

By taking the ratio of the input power P_{in} and the maximum output power at the bright fringe, both measured with a powermeter, this reflectivity could be confirmed. This experimental value was slightly lower than the theoretical value of $r_{\mathrm{m,theo}}^2 = 0.23$ calculated with equation (3.1). The value strongly depends on the refractive index which may vary depending on the pureness of the silicon nitride. The used membrane

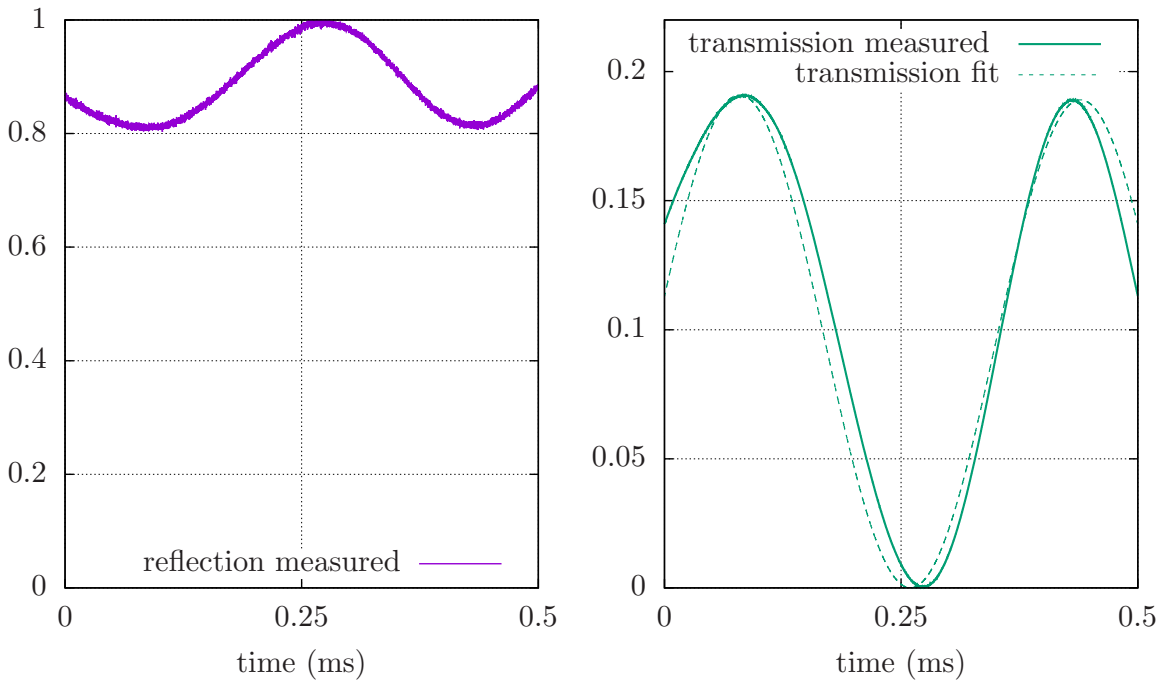

Figure 6.5: Interferometer signal for a scanned membrane displacement in reflection (left) and in transmission (right): The graphs show the measured signals of both photodiodes, that were used for the contrast adjustment. The reflected signal showed the sum of the Sagnac mode as flat signal and the Michelson mode as sinusoidal signal. Their ratio determined the experimental value for the membrane power reflectivity $r_{\mathrm{m}}^2 = 0.19 \pm 0.005$. On the right the transmission signal is shown. The Sagnac mode interfered deconstructively and almost only the Michelson mode fringes are measured. The height difference between the maxima could be explained with a non perfect balancing of the beamsplitter. Fitting the data with the squared function for the output amplitude given in equation (3.13) resulted in a mismatch of $\Delta_{\mathrm{bs}} = |r_{\mathrm{m}}^2 - t_{\mathrm{m}}^2| = 0.0012$. The reached contrast was $C = 0.997$.

was a stochiometric membrane. The additional tension on the material had an additional influence on its refractive index. Also the thickness might not have been exact due to its production process, which caused another error. Considering these points, the discrepancy between the theoretical and the experimental value was reasonable.

On the right of figure 6.5 the measured transmission of the interferometer is shown. As the Sagnac mode interfered almost completely constructively for an optimized setup, this signal mainly showed the Michelson mode as a sinusoidal signal cause by the scanned displacement of the membrane. The maxima had different heights as predicted by the theory for the interferometer fringe for a non perfect beamsplitter balancing. The theoretical function given in equation (3.13) was plotted in figure 3.3 for different splitting ratios. As the positioner of the membrane did not react perfectly linearly to the applied voltage, the resulting fitted curve of the signal did not overlap exactly. Nevertheless, it provided a value for the unbalancing of the beamsplitter. With the applied adjustment techniques, a minimum unbalancing of

$$\Delta_{\mathrm{bs}} = |0.5006 - 0.4994| = 0.0012 \tag{6.8}$$

and a maximum contrast of

$$C = 0.997 \tag{6.9}$$

was reached.

6.2.3 The Influence of Laser Amplitude Noise

The laser amplitude noise and its contribution to the total noise of the interferometer output needed to be considered for the goal to reach the quantum regime with the displacement spectral density. The used laser in this experiment was a *Koheras BoostiK system* by *NKT Photonics*, consisting of a seed laser and an amplifier with fiber output. The system had a maximum output power of 5 W at a wavelength of $\lambda = 1550\,\mathrm{nm}$. The relative intensity noise (RIN) was measured with a single photodiode and a spectrum analyzer for a power of 2 mW for the direct output of the laser and for the output of the pre-mode-cleaner cavity, which filtered the mode to provide a clean TEM_{00} mode as shown in the setup in figure 3.2. The results are given in figure 6.6. The high peak at 1.3 MHz showed the relaxation oscillation of the laser. The peak at 330 kHz was caused by the amplifier of the laser system. The lower frequency peaks were caused by resonances of the electronics of the measurement photodiode. At 400 kHz close to the expected resonance frequency of the of the mem-

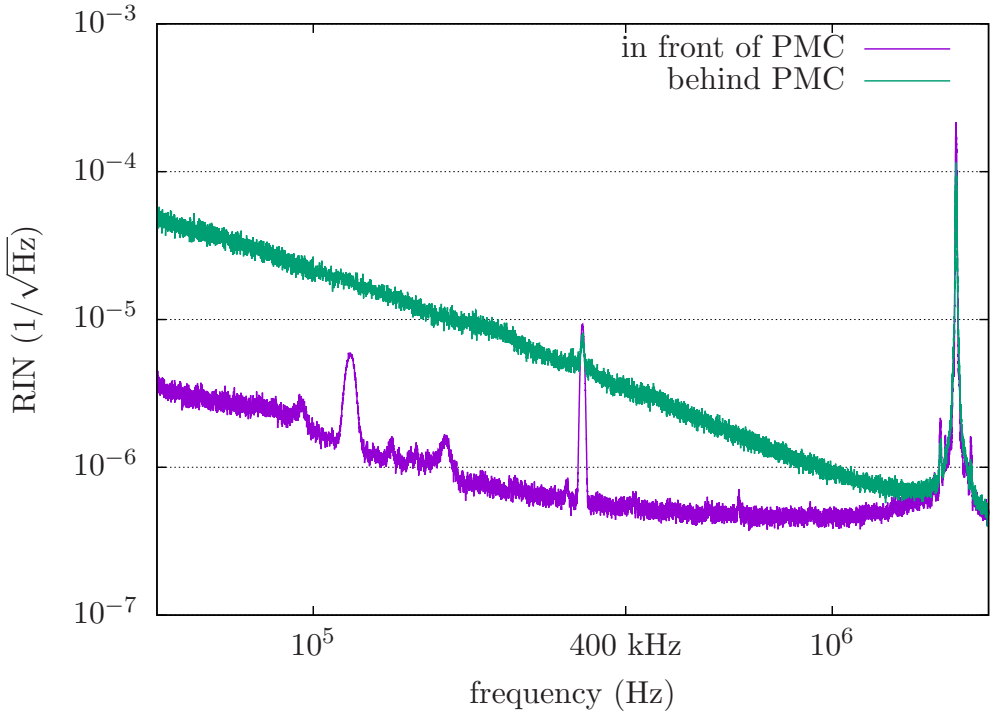

Figure 6.6: Measured relative intensity noise (RIN) of the laser system: The measured power with a single photodiode was 2 mW, the resolution bandwidth was RBW = 5 kHz, the video bandwidth VBW = 1 kHz and the sweep time ST = 7.7 s. The data was averaged 20 times. The RIN was measured in front of and behind the pre-mode-cleaner cavity with the same broadband photodiode. The phase noise of the laser was converted to amplitude noise in the cavity and therefore increased the RIN for the transmitted light. The highest peak at 1.3 MHz was caused by the laser relaxation oscillation. The peak at 330 kHz was caused by the amplifier of the laser system. The peaks at lower frequencies showed resonances of the used photodiode.

brane's fundamental mode, the relative intensity noise was $\mathrm{RIN}_{\mathrm{las}} = 5 \cdot 10^{-7} \frac{1}{\sqrt{\mathrm{Hz}}}$ before and $\mathrm{RIN}_{\mathrm{PMC}} = 4 \cdot 10^{-6} \frac{1}{\sqrt{\mathrm{Hz}}}$ behind the resonator. This result shows that the laser had high phase noise that was transformed into amplitude noise by the resonator. For the future it might be interesting to deliberate whether the increased amplitude noise or the ellipticity of the laser mode before filtering it has a stronger negative effect and if it might make sense to remove the pre-mode-cleaner cavity.

In section 3.4.2 the impact of the laser amplitude noise on the displacement spectral density was discussed. With the measured RIN, the input power limits for equal technical laser amplitude noise and shot noise could be calculated. The first limit follows from the impact of the laser amplitude noise because of the imperfect beamsplitter balancing. To perform a quantum-noise dominated measurement, unequation (3.44) had to be fulfilled. For the determined unbalancing of the beamsplitter given in equation (6.8) the input power limit for dominating shot noise calculates as

$$P_{\mathrm{in}} < 11\,\mathrm{mW}\ . \tag{6.10}$$

The second limit occurred during the measurement with the photodiodes and was calculated with unequation (3.45) for an output power in the dark fringe $P_{\mathrm{out,df}} = r_{\mathrm{m}}^2(1-C)P_{\mathrm{in}}$. Using the measured values for the contrast from equation (6.9) and the membrane reflectivity from equation (6.7) the corresponding limit for the input power was

$$P_{\mathrm{in}} < 28\,\mu\mathrm{W}\ . \tag{6.11}$$

In consequence, a quantum-noise limited sensitivity measured with a single photodiode could only be reached for interferometer input powers below this value. However, in the presented work a balanced homodyne detector as described in section 4.2.1 was used. Due to its functionality, correlated amplitude noise, that is evenly distributed on the two photodiodes, cancels out. In an ideal case, the splitting ratio of the homodyne detector beamsplitter would be perfectly balanced for the local-oscillator light as well as for the signal field and both photodiodes would have exactly the same quantum efficiency and dark currents. In reality, the splitting ratio is adjusted by minimizing the difference of the photocurrents for the local-oscillator field and in consequence differences in the parameters of the photodiodes are compensated by beamsplitter unbalancing. Therefore the common mode rejection for the signal field entering the balanced homodyne detector from the other port of the beamsplitter is expected to be imperfect. A realization of a maximum common mode rejection of 75.2 dB by

parameter compensation of the photodiodes is described in [86]. Without this technique the impact of the laser amplitude noise of the signal is expected to dominate the sensitivity of the presented Michelson-Sagnac interferometer for high laser powers. Nevertheless, it is assumed that a quantum-noise limited displacement spectral density can be reached for higher powers than the limit given in equation (6.11).

An improvement of the contrast would increase the second limit. The first limit could only be improved with a better beamsplitter balancing or a more stable amplitude of the input light.

6.3 Squeezed States in the Michelson-Sagnac Interferometer

6.3.1 The Experimental Injection of Squeezed States

After a high contrast for the Michelson-Sagnac-interferometer modes was reached, the squeezed-light source could be implemented into the optomechanical experiment. In figure 6.7 the whole setup is shown. At different beamsplitters, the light coming out of the pre-mode-cleaner cavity was split up into the input light for the Michelson-Sagnac interferometer, the light for the SHG resonator, the adjustment field entering the PDC resonator from the back and the local-oscillator field for the balanced homodyne detector. The squeezed-light source was described in section 4.3.2, the Michelson-Sagnac interferometer in section 3.2 and the balanced homodyne detection in section 4.2.1.

The field produced by the squeezed-light source was injected into the interferometer through the output port. All light fields were initially polarized perpendicularly to the optical table. The output field of the Michelson-Sagnac interferometer passed a $\lambda/2$ waveplate and a Faraday rotator, each rotating the polarization by 45°. The light with the resulting parallel polarization transmitted through a polarizing beamsplitter (PBS). The perpendiculary polarized squeezed states coming from the PDC resonator were reflected by the same PBS and transmitted the Faraday rotator and waveplate in the opposite direction. Their polarization was rotated by 45° in the rotator, but due to the Faraday effect in the reverse direction compared to the interferometer signal. Therefore the squeezed light was again perpendicularly polarized after passing the $\lambda/2$ waveplate. As a consequence both fields inside the interferometer had the same polarization and interfered. When the dark fringe condition was fulfilled, the squeezed light was reflected by the interferometer and propagated with the dark signal field to the balanced homodyne detector.

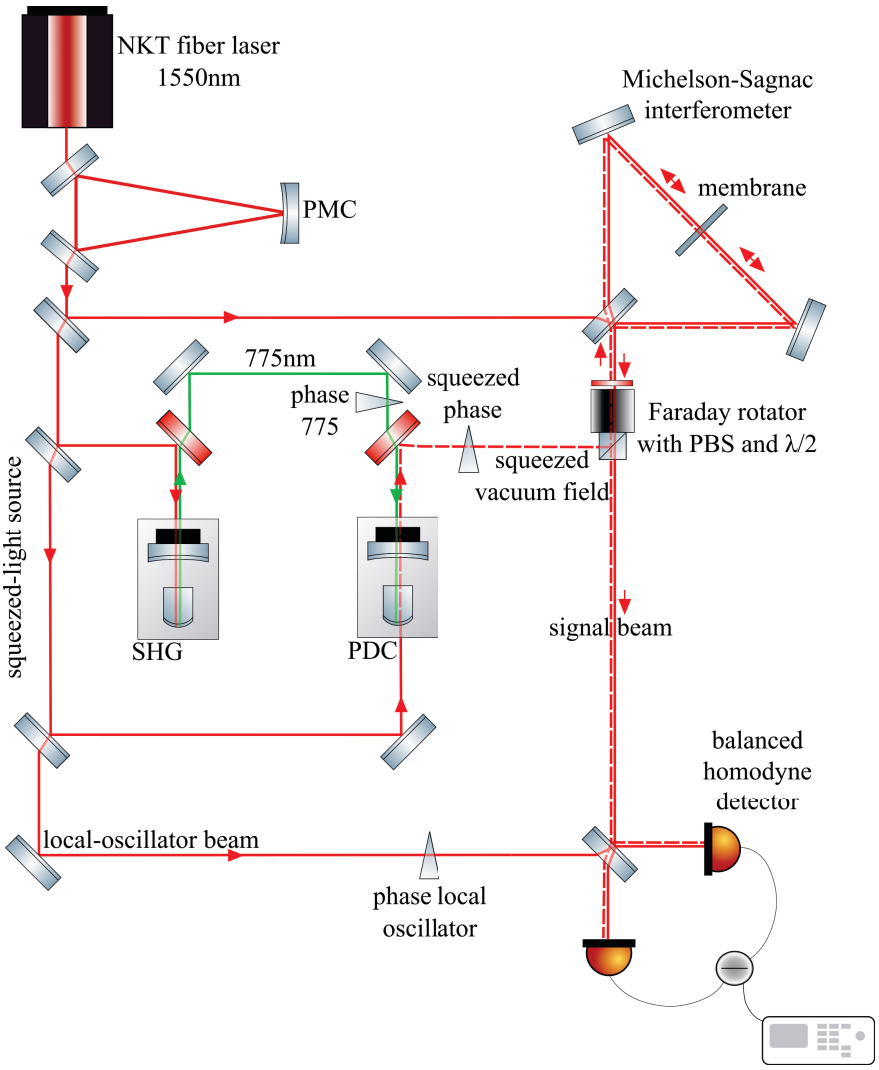

Figure 6.7: The complete optomechanical experiment with implemented squeezed-light source: At first the 1550 nm field from the NKT fiber laser was filtered by the pre-mode-cleaner cavity to provide a clean TEM_{00} mode. The transmitted beam was split up into the incoming field for the Michelson-Sagnac interferometer (see section 3.2), the field for the squeezed-light source (see section 4.3.2) and the local-oscillator field for the balanced homodyne detector (see section 4.2.1). The perpendicularly polarized squeezed vacuum field produced in the PDC was injected into the output port of the interferometer via a polarizing beamsplitter (PBS) and a Faraday rotator in combination with a $\lambda/2$ waveplate. Inside the interferometer it interfered with the bright signal field. The resulting perpendicularly polarized field coming out of the interferometer passed the waveplate and the rotator and transmitted the PBS with a parallel polarization. It overlapped with the local-oscillator beam on the balanced beamsplitter of the balanced homodyne detector.

As optical losses had to be minimized to measure squeezed states as explained in section 4.2.2, an optimization of the overlap of the squeezed vacuum field, the interferometer signal and the local oscillator on the beamsplitter of the balanced homodyne detector was crucial. To achieve a good mode matching, a triangular resonator was installed as a mode reference, the so called *diagnose mode cleaner* (DMC). For the mode matching procedure a flip mirror was placed in front of one of the homodyne detector photodiodes. The local-oscillator light was reflected to the resonator and the transmission was measured with a photodiode.

Using two lenses in the path, the mode of the local-oscillator light was optimized for a maximum transmission of the TEM_{00} mode through the DMC resonator. Subsequently this light was blocked and the interferometer output field was sent to the same resonator. With two lenses in front of the homodyne detector beamsplitter, its mode was also matched to the DMC and thus as well to the local-oscillator field. The third step was to adjust the mode of the squeezed vacuum field with the other two fields blocked. For this purpose the 1550 nm adjustment beam transmitting through the PDC cavity from the back was used. Two lenses between the squeezed-light source and the interferometer allowed the optimization of the mode reflected by the interferometer to the resonator. The mode matching of the three fields to the diagnose-mode-cleaner cavity gave an indication for the visibility between the fields on the beamsplitter of the balanced homodyne detector.

Using this technique, a mode matching of the local oscillator to the resonator of 99.8 % was reached. The mode matching of the bright interferometer output was 98.2 %, the mode matching of the adjustment field in reflection of the interferometer was ≈ 98.5 %.

In addition, a path with flip mirrors between the PDC resonator and the balanced homodyne detector was set up for the option to measure the squeezed states directly before they entered the interferometer. With an additional lense set the adjustment field was mode matched to the diagnose-mode-cleaner cavity to optimize the detection efficiency. Here a mode matching of ≈ 99.5 % was reached.

6.3.2 The Feedback Control Loops for the Phase Stabilization

Three feedback control loops for the phase relations between the different light fields in the setup had to be implemented. The phase between the interferometer output

light and the local-oscillator light defined the readout quadrature. When the squeezed vacuum states were injected, their phase in respect to the field in the interferometer needed to be stabilized as well. For this purpose a single-sideband field was used, which entered the PDC cavity from the back. Its phase in relation to the pump field and the local-oscillator light was controlled for a stable phase relation between these two.

Stabilization of the MSI readout quadrature: To adjust the phase between the signal beam and the local-oscillator field, a piezo-actuated mirror was placed in the local-oscillator path. A constructive interference with $\Delta\phi = \pi$ of the fields corresponded to a readout in amplitude quadrature, a destructive interference with $\Delta\phi = \frac{\pi}{2}$ corresponded to a readout in phase quadrature. For a lock in phase quadrature the DC output of the balanced homodyne detector served as error signal as it occurred in its zero transient.

For a measurement in the amplitude quadrature, the derivative of the DC signal was required to lock on the maximum of its amplitude. The therefore necessary components are shown in figure 6.8. The local-oscillator beam passed an electro-optic modulator, that generated sidebands at $\Omega_{\mathrm{EOM}} = 25\,\mathrm{MHz}$. The DC output of the balanced homodyne detector was high-pass filtered and demodulated with Ω_{EOM}. The result was low-pass filtered and provided the error signal, which had its zero transient at the maximum of the DC output. It was used to actively stabilize the phase by regulating the voltage on the piezo-actuated mirror. Positioning this mirror close to the homodyne detector minimized pointing.

Stabilization of the squeeze angle: When squeezed states were injected into the interferometer, their phase relative to the light in the interferometer and therefore to the local-oscillator field had to be stabilized as well. The applied technique of a single-sideband lock was developped by Henning Vahlbruch [39]. As the squeezed vacuum field didn't have an amplitude itself, a coherent control field was used, which was phase stabilized in respect to the 775 nm pump field and to the local-oscillator field. For this purpose, the single sideband with a frequency shift of $\Omega_{\mathrm{AOM}} = 27\,\mathrm{MHz}$ to the carrier

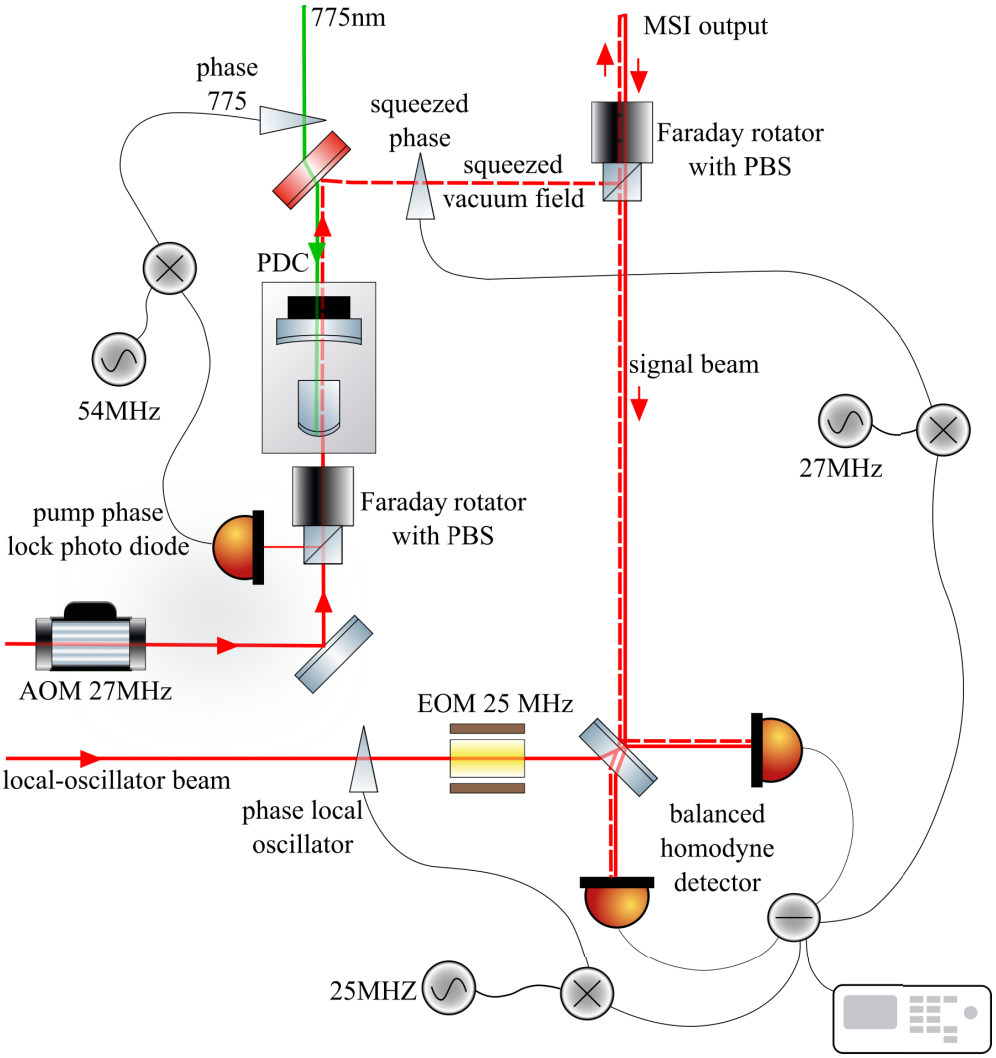

Figure 6.8: Schematics of the control loops for the stabilization of the read-out and squeeze angle: Using an electro-optic modulator (EOM), side bands at a frequency of 25 MHz were generated on the local oscillator. When the interferometer signal and the local-oscillator field interfered at the balanced homodyne detector, filtering its output signal and mixing it down at the modulation frequency delivered a sinusoidal error signal with a zero crossing for a stabilization in the amplitude quadrature. As the squeezed states didn't have an amplitude, a frequency-shifted control field at 27 MHz was generated with an acoustooptic modulator (AOM) and sent through the PDC cavity. With two feedback loops its phase relations to the 775 nm pump field and to the local-oscillator field were stabilized. For the first one the signal of a photodiode in reflection of the PDC cavity was demodulated with double the frequency. The balanced homodyne detector signal was demodulated with the original frequency to generate an error signal for the second control loop to determine the phase between the control field and the local oscillator.

frequency ω was created by modulating light of the fundamental frequency ω with an acousto-optic modulator (AOM). The first order sideband beam was diffracted under an angle to the fundamental beam and could be separated from it with a pinhole. It entered the PDC resonator from the back through the high-reflective coated crystal as illustrated in figure 6.8. Inside the crystal it induced a parametric down-conversion process, which generated a second sideband with a frequency shift of $-27\,\mathrm{MHz}$. The resulting field

$$E_{\mathrm{ss}}(t) \propto \frac{1+e^{2r}}{\sqrt{e^{2r}}}\alpha_\Omega \cos\Big((\omega+\Omega_{\mathrm{AOM}})t\Big) - \frac{1-e^{2r}}{\sqrt{e^{2r}}}\alpha_\Omega \cos\Big((\omega-\Omega_{\mathrm{AOM}})t-2\theta\Big) \quad (6.12)$$

with single sideband amplitude α_Ω, squeeze parameter r and squeeze angle θ left the resonator on both sides. To adjust the phases to the pump field and to the local oscillator, piezo-actuated mirrors were placed in the pump field path in front of the PDC resonator and in the path of the squeezed field right before the injection into the interferometer via the Faraday rotator.

Behind the PDC resonator another Faraday rotator was placed, such that the polarization of the reflected single sideband was orthogonal to the polarization of the incoming light. It was separated with a polarizing beamsplitter and detected with a resonant photodiode. Its voltage was demodulated with the frequency difference $2\Omega_{\mathrm{AOM}} = 54\,\mathrm{MHz}$ of the two sidebands. After low-pass filtering, the result was a sinusoidal error signal for the phase between the pump beam and the control beam. It was used to actively stabilize their phase relation by sending a voltage to the piezo-electric mirror in the pump field path.

The second step was the stabilization of the phase of the control field to the local oscillator. In the case of a simple squeezed-states measurement this phase determined the readout angle. In the case of squeezed states injected into the interferometer it determined the squeeze angle of the light in relation to interferometer signal. For this control loop the balanced homodyne detector DC signal was used. The fields measured by the two photodiodes

$$\begin{aligned} E_{\mathrm{PD}\pm} \propto & \frac{1}{\sqrt{2}}\Big[\alpha_{\mathrm{LO}} e^{-i(\omega t+\phi)} \pm \Big(\frac{1+e^{2r}}{\sqrt{2e^{2r}}}\alpha_\Omega \cos((\omega+\Omega_{\mathrm{AOM}})t) \\ & - \frac{1-e^{2r}}{\sqrt{2e^{2r}}}\alpha_\Omega \cos((\omega+\Omega_{\mathrm{AOM}})t-2\theta)\Big)\Big] \end{aligned} \quad (6.13)$$

with readout angle ϕ, the amplitude of the local-oscillator α_{LO} and the amplitude of the single sideband α_{Ω} induced photocurrents, that were subtracted from each other. This signal was high-pass filtered and demodulated with Ω_{AOM} to receive an error signal depending on the squeeze angle θ and the readout phase ϕ. θ was already fixed by the pump phase control loop. ϕ was stabilized by using this error signal to send a voltage to the piezo-actuated mirror in the path of the squeezed field. In the case of a simple squeezing measurement, the squeezed field propagated directly to the balanced homodyne detector and only a stable relation between ϕ and θ was relevant. In the case of injecting squeezed states into the interferometer, θ had to be chosen relative to the readout quadrature of the interferometer.

7 The Performance of the Squeezed Cryogenic Michelson-Sagnac Interferometer

This chapter presents the data, that was measured with the previously described optomechanical setup. It includes a determination of the membrane resonance frequencies followed by a characterization of the fundamental mode. The spectra were measured at room temperature and at 100 K to examine the influence of the temperature on the noise contributions and on the quality factor. To receive the displacement spectral density, the data was calibrated with the theoretical shot noise. It was firstly aimed for a shot-noise limited interferometer sensitivity to demonstrate the enhancing effect of squeezed states. In the next step the squeezed-light source was characterized. In the beginning the states were measured directly with the balanced homodyne detector, secondly they were injected into the interferometer.

7.1 Measurement of the Membrane Resonance Frequencies

For the characterization of the membrane in the Michelson-Sagnac interferometer, an input field with a power of $P_{\mathrm{in}} = (50 \pm 5)\,\mu\mathrm{W}$ was used. The displacement of the membrane was chosen such, that the dark fringe condition from section 3.2 was fulfilled and the output power was in its minimum $P_{\mathrm{out}} = r_{\mathrm{m}}^2(1-C)P_{\mathrm{in}}$ with C being the contrast of the MSI and r_{m}^2 being the membrane power reflectivity. The signal was measured with the balanced homodyne detector as shown in figure 6.3. It was fed into a spectrum analyzer to receive the noise spectral density. All spectra were recorded for a pressure of $< 10^{-6}$ mbar in the vacuum chamber. At first a broad spectrum was measured to determine the membrane's resonance frequencies. The result is plotted in figure 7.1.

The fundamental resonance peak, the (1,1) mode, was found at $f_{\mathrm{res}}^{1,1} = 414.72\,\mathrm{kHz}$. The deviation from the theoretical value calculated in equation (3.4) is 1 %. This discrepancy is reasonable considering the unknown error for the thickness and tension of the membrane and the purity of the material. The frequencies of the higher-order modes were calculated with

$$f_{\mathrm{res}}^{m,n} = \frac{\Omega_{\mathrm{res}}^{m,n}}{2\pi} = \frac{f_{\mathrm{res}}^{1,1}}{\sqrt{2}}\sqrt{m^2+n^2}\ . \tag{7.1}$$

This equation followed directly from equation (3.4) for a perfectly square membrane with $l_x = l_y$. The calculated and measured resonance frequencies in the range of

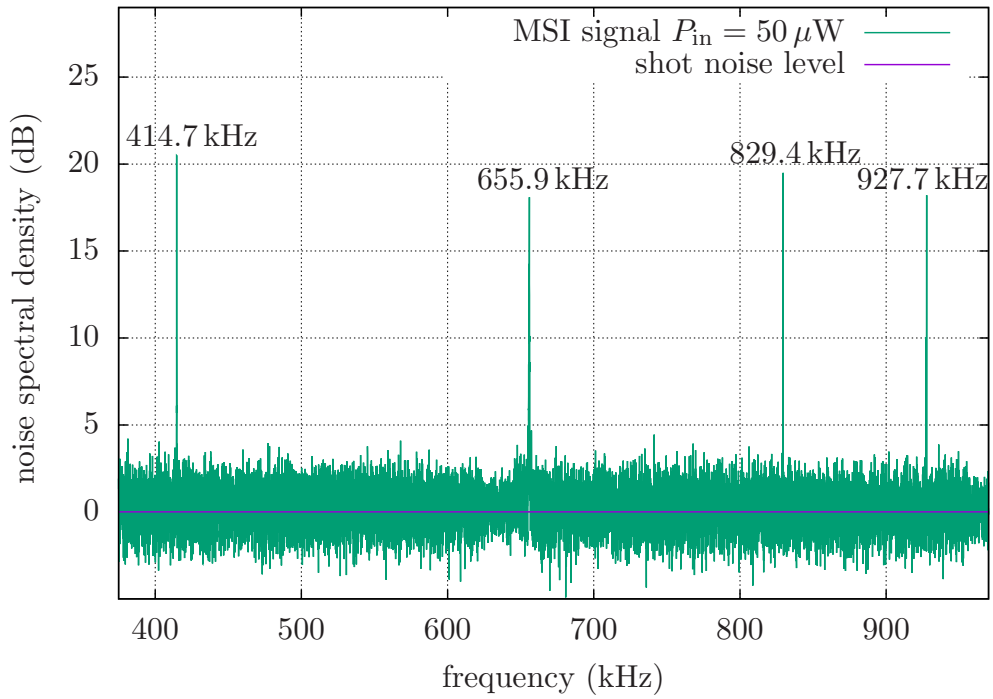

Figure 7.1: Broad spectrum of the Michelson-Sagnac interferometer noise spectral density: The data was recorded for an input power of $(50 \pm 5)\,\mu$W and a local-oscillator power of 11 mW. It was normalized to the vacuum shot-noise level of the local oscillator, which was measured by taking a spectrum without signal light from the MSI. The resolution bandwidth of the spectrum analyzer was RBW = 2 Hz, the video bandwidth RBW = 500 Hz and the sweep time ST = 10 s. The shown curve was averaged 20 times. Within the frequency range, the resonance peaks $f_{\mathrm{res}}^{1,1}$, $f_{\mathrm{res}}^{1,2}$, $f_{\mathrm{res}}^{2,1}$, $f_{\mathrm{res}}^{2,2}$, $f_{\mathrm{res}}^{1,3}$ and $f_{\mathrm{res}}^{3,1}$ were detected, the frequency differences between the (1,2) and the (2,1) mode, as well as between the (1,3) and the (3,1) mode were too small to be visible in this graph's scale.

	$f_{\mathrm{res}}^{1,1}$	$f_{\mathrm{res}}^{1,2}$	$f_{\mathrm{res}}^{2,2}$	$f_{\mathrm{res}}^{1,3}$
measured	414.72 kHz	655.9 kHz	829.5 kHz	927.7 kHz
calculated		655.7 kHz	829.4 kHz	927.3 kHz

Table 2: Measured higher-order resonance frequencies of the membrane and corresponding values calculated via equation (7.1) from the fundamental mode.

the measured noise spectrum are given in table 2. The frequencies of the (1,2) and the (2,1) mode only differed by 0.2 kHz and the resonances were therefore not visible as separate peaks on the shown scale. For the (1,3) and the (3,1) only one peak was detected. Thus, the assumption of an almost perfectly square membrane was reasonable. The calculated values for the higher-order resonance frequencies confirmed that the measured peaks were all caused by the membrane and not by other noise sources as for example technical laser noise or electronic noise.

7.2 The Measurement and Calibration of Shot-Noise Dominated Spectra at T = 293 K and T = 100 K

For an enhancement of the interferometer's sensitivity by injecting squeezed states, the spectrum must be quantum-noise limited. Concluding from the evaluations of the relevant noise contributions in sections 3.3 and 3.4, the measurement of radiation pressure noise was not possible with the current setup. Therefore it was aimed for a shot-noise dominated displacement spectral density off resonance with a peak caused by thermal noise.

In section 6.2.3 the *relative intensity noise* (RIN) of the laser was measured to quantify the impact of laser amplitude noise. An input power limit of $P_{\mathrm{in}} < 28\,\mu\mathrm{W}$ was calculated in equation (6.11) for lower laser amplitude noise $\sqrt{S_{\mathrm{ln}}}$ than shot noise $\sqrt{S_{\mathrm{SN}}^{\mathrm{MSI}}}$ for the detection with a single photodiode. Due to the expected common noise rejection of the correlated laser amplitude noise in the balanced homodyne detector, it was examined if a shot-noise limited sensitivity can be reached for higher input powers.

Figure 7.2 shows the resonance peak of the fundamental mode for different input powers P_{in} between 30 μW and 2 mW measured at the dark fringe. To receive the displacement spectral density, the data series were calibrated with the corresponding shot noise. The theoretical shot noise levels for the used input powers calculated via

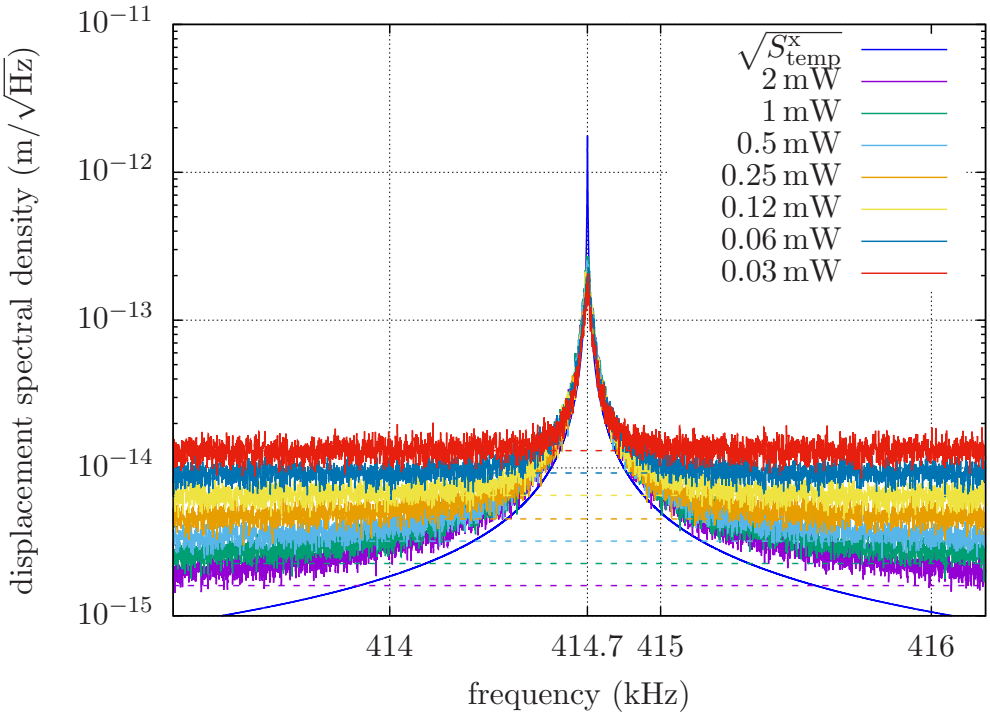

Figure 7.2: Displacement spectral density around the (1,1) mode for different input powers at room temperature: The data around the resonance frequency of $f_{res}^{1,1} = 414.7\,\text{kHz}$ measured with the balanced homodyne detector was recorded for powers from $30\,\mu\text{W}$ to $2\,\text{mW}$ and calibrated to the calculated vacuum shot noise with equation (7.2). The shot-noise levels from table 3 are given by the dashed lines. For the lowest three powers the slopes approached the vacuum shot noise. For higher powers the curves stayed above the shot noise level and could not be fitted with a theoretical sum of shot noise and thermal noise, which could be explained by the impact of the laser amplitude noise. The data for each power was recorded for a resolution bandwidth of $\text{RBW} = 1\,\text{Hz}$, a video bandwidth of $1\,\text{Hz}$ and a sweep time of $\text{ST} = 1.9\,\text{s}$ and was averaged 20 times. The curve for the thermal noise $\sqrt{S^{x}_{temp}}$ is a theoretical model of the thermal noise given in equation (3.38) for the temperature $T = 293\,\text{K}$, the effective mass $m_{eff} = (71 \pm 5)\,\text{ng}$ and a quality factor $Q = 2.7 \cdot 10^5$. It is shown for reference and will be discussed further in section 7.3.2.

P_{in} (mW)	$\sqrt{S^{\text{MSI}}_{\text{SN,x}}}\left(\frac{\text{m}}{\sqrt{\text{Hz}}}\right)$
2 ± 0.05	$(1.60^{+0.02}_{-0.02}) \cdot 10^{-15}$
1 ± 0.03	$(2.26^{+0.04}_{-0.03}) \cdot 10^{-15}$
0.5 ± 0.01	$(3.20^{+0.35}_{-0.33}) \cdot 10^{-15}$
0.25 ± 0.005	$(4.53^{+0.33}_{-0.31}) \cdot 10^{-15}$
0.12 ± 0.005	$(6.54^{+0.14}_{-0.13}) \cdot 10^{-15}$
0.06 ± 0.005	$(9.24^{+0.41}_{-0.36}) \cdot 10^{-15}$
0.03 ± 0.005	$(1.31^{+0.12}_{-0.10}) \cdot 10^{-14}$

Table 3: Calculated shot-noise levels following from equation (3.23) for different input powers P_{in}.

equation (3.23) are given in table 3. The relative error of the powermeter to measure the input power was higher for low light powers. The other used parameters were the membrane power reflectivity $r_{\text{m}}^2 = 0.19 \pm 0.005$ and the wavelength $\lambda = 1550\,\text{nm}$. With the spectrum analyzer the shot-noise level $P_{\text{dB, SN}}$ of the local-oscillator field in dB was measured. Converted into power, this value scaled linearly with the squared calculated shot-noise level $S^{\text{MSI}}_{\text{SN,x}}$. The data points of the spectra, measured as noise spectral density P_{dB}, were transformed using the resulting relation

$$\sqrt{10^{\frac{1}{10}(P_{\text{dB}} - P_{\text{dB, shot}})} S^{\text{MSI}}_{\text{SN,x}}} = \sqrt{S^{\text{MSI}}_{\text{x}}}\,. \tag{7.2}$$

All measured spectra show the same shape of the oscillator transfer function caused by the thermal noise. For reference the theoretical curve $\sqrt{S^{\text{x}}_{\text{temp}}}$ following from equation (3.38) is given for the temperature $T = 293\,\text{K}$, the effective mass $m_{\text{eff}} = (71 \pm 5)\,\text{ng}$ and a quality factor of $Q = 2.7 \cdot 10^5$. Its analysis will be discussed further in section 7.3.2. For the powers P_{in} between $30\,\mu\text{W}$ and $125\,\mu\text{W}$, the slopes went down to the corresponding vacuum shot-noise level. The noise floor of the spectra for $P_{\text{in}} = 250\,\mu\text{W}$ and higher stayed above shot-noise level and their shape could not be fitted with the theoretical sum of shot noise and thermal noise given in equation (7.5) as it will be described in section 7.3.2. The explanation is the increasing impact of laser amplitude noise. A shot-noise limited sensitivity could therefore be reached for powers $P_{\text{in}} \leq 125\,\text{mW}$. In comparison to the power limit following from the RIN, the measurement shows that the common noise rejection of the balanced homodyne detector increased the maximum input power for a shot-noise limited sensitivity by a factor of ≥ 5.

In the next step, the cryostat was used to cool the interferometer down to 100 K. The temperature was measured with the thermometer attached to the membrane holder. Despite choosing Invar as spacer material because of its low thermal expansion and minimizing the deformation in the design, the contrast decreased to below 50 % when the interferometer was cooled down. With the same adjustment procedure described in section 6.2.2, a contrast of $C = 99.7\,\%$ could be achieved again at 100 K. With the installed system a minimum temperature of 15 K could be reached, however the high contrast at this temperature could not be reproduced because the positioner for the vertical membrane angle could not be moved anymore.

At a temperature $T = 100\,\mathrm{K}$ the resonance frequency of the (1,1) mode was decreased to $f_{\mathrm{res}}^{1,1} = 406.0\,\mathrm{kHz}$. Figure 7.3 shows the displacement spectral density around the resulting peak for different input powers at the dark fringe as in figure 7.2 at room temperature. The data series were calibrated to the same corresponding theoretical shot-noise levels given in table 3 using equation (3.38). The theoretical curve of the on resonance dominating thermal noise $\sqrt{S_{\mathrm{temp}}^{\mathrm{x}}}$ following from equation (3.38) is given for the temperature $T = 100\,\mathrm{K}$, the effective mass $m_{\mathrm{eff}} = (71 \pm 5)\,\mathrm{ng}$ and a quality factor of $Q = 1.6 \cdot 10^6$. Its analysis will be discussed further in section 7.3.2. For the input powers P_{in} from $30\,\mu\mathrm{W}$ to $125\,\mu\mathrm{W}$ the slopes again went down to the vacuum shot noise levels shown as dashed lines. For higher powers the laser amplitude noise was dominating the spectrum off resonance. Therefore the reached common noise rejection of ≥ 5 from the room temperature measurement could be reproduced. For both operating temperatures a quantum-noise limited displacement spectral density could be reached for input powers $P_{\mathrm{in}} \leq 125\,\mu\mathrm{W}$.

7.3 The Characterization of the Silicon Nitride Membrane

7.3.1 The Evaluation of the Measured Noise Spectral Density

The main focus of the presented work lays on the enhancement of the interferometer sensitivity by injecting squeezed states. When this technique will be applied in the future to measure and reduce radiation pressure noise, the signal-to-noise ratio and therefore reaching high quality factors will become a matter of interest. For this reason the membrane in the Michelson-Sagnac interferometer should be characterized. Currently the option of a ring-down measurement as described in section 8.2 was not given, as no mechanical excitement of the membrane mode was possible. Hence, the

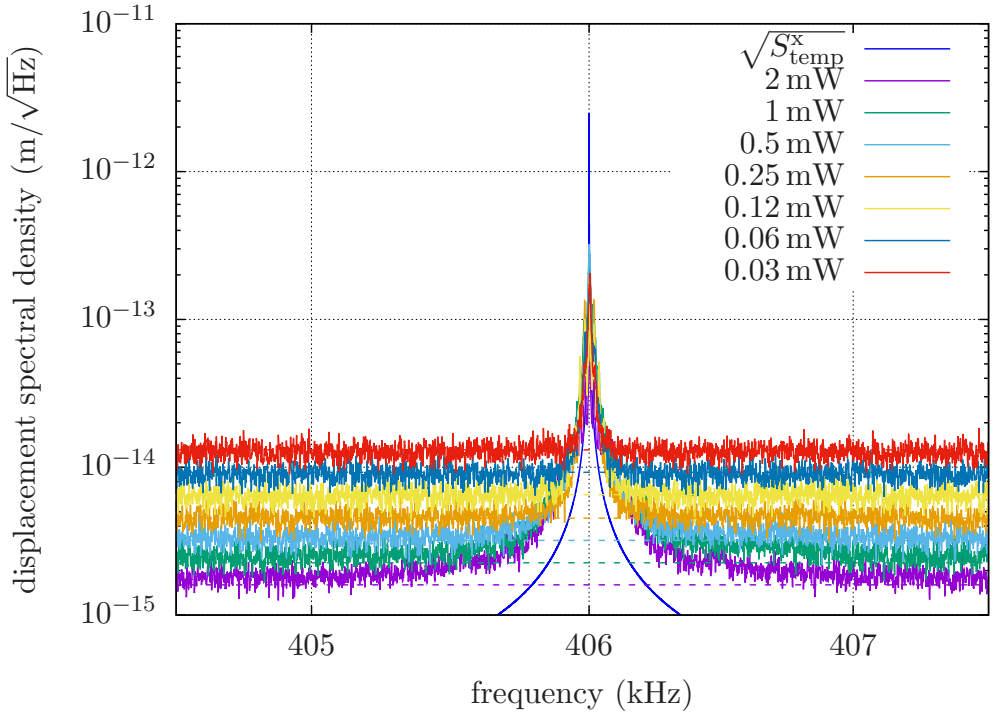

Figure 7.3: Displacement spectral density around the (1,1) mode for different input powers at 100 K: The data measured with the balanced homodyne detector was recorded for powers from 30 μW to 2 mW and calibrated to the vacuum shot noise as in figure 7.6 with equation (7.2). The shot-noise levels from table 3 are given by the dashed lines. Again for the three lowest powers P_{in} the slopes approached the vacuum shot noise, for higher powers the curves stayed above the shot-noise level. Compared to the data at room temperature the peak became smaller and narrower. The data for each power was measured with a resolution bandwidth of RBW = 1 Hz, a video bandwidth of VBW = 1 Hz and a sweep time of ST = 1.9 s and was averaged 20 times. The curve for the thermal noise $\sqrt{S^{x}_{\text{temp}}}$ is a theoretical model of the thermal noise given in equation (3.38) for the temperature $T = 100\,\text{K}$, an effective mass $m_{\text{eff}} = (71 \pm 5)\,\text{ng}$ and a quality factor $Q = 1.5 \cdot 10^6$. It is shown for reference and will be discussed further in section 7.3.2.

spectra recorded with the spectrum analyzer were evaluated. This section addresses three effects impacting the measurement, that need to be considered to interpret the results: The functionality of the spectrum analyzer, the fluctuations of the peak height and the instability of the readout quadrature.

The resolution bandwidth of the spectrum analyzer: For a proper understanding of the data measured with a spectrum analyzer, its functionality needs to be taken into account. The presented spectra were recorded in the frequency domain. In this case the spectrum analyzer measures how much power is present for one frequency. Realistically in such a measurement every data point gives the power in a defined frequency band during a finite time interval. The resolution bandwidth (RBW) determines the frequency band, over which one data point is measured. The video bandwidth (VBW) has the effect of an adjustable low pass filter. If the cut off frequency is below the RBW, the response to quick fluctuations is affected, resulting in a smoothing of the spectrum. Thus, to measure narrow features, a video bandwidth VBW $\leq$ RBW should be chosen [87].

Each measured data point is not the exact value of the noise power for a certain frequency f, but the integral over a frequency interval $[f - \frac{\mathrm{RBW}}{2}, f + \frac{\mathrm{RBW}}{2}]$. The spectrum analyzer, that was used to record the presented spectra, had a minimum resolution bandwidth of RBW = 1 Hz. Figure 7.4 illustrates its influence for the example of two resonance peaks. The shown displacement-spectral-density functions of the thermal noise in the experiment at a temperature $T = 100\,\mathrm{K}$ were modeled with equation (3.38) for a resonance frequency $f_{\mathrm{res}}^{1,1} = 406.0\,\mathrm{kHz}$ and an effective mass $m_{\mathrm{eff}} = 71\,\mathrm{ng}$. Two different quality factors were assumed. The left curve corresponds to a quality factor of $Q = 0.5 \cdot 10^5$ and a full width half maximum of FWHM = 8 Hz. In a measured spectrum with RBW = 1 Hz, the recorded data represents the actual noise quite well. The data point on resonance given by the integral over $[f_{\mathrm{res}} - \frac{\mathrm{RBW}}{2}, f_{\mathrm{res}} + \frac{\mathrm{RBW}}{2}]$ only has a discrepancy of $< 0.5\,\%$ to the theoretical noise power on the peak tip. The right curve shows the function with a quality factor $Q = 50 \cdot 10^5$ and a full width half maximum of FWHM = 0.08 Hz. Using the same resolution bandwidth RBW = 1 Hz an integral on resonance over $[f_{\mathrm{res}} - \frac{\mathrm{RBW}}{2}, f_{\mathrm{res}} + \frac{\mathrm{RBW}}{2}]$ would result in a data point that is 3 times smaller than the actual noise. It shows that the height of a membrane peak narrower than the resolution bandwidth is impossible to be resolved with a spectrum analyzer. Next to the peak tip the slopes decrease. Thus, the integrals over a bandwidth of 1 Hz off resonance, as pictured in the right model, conform to the actual

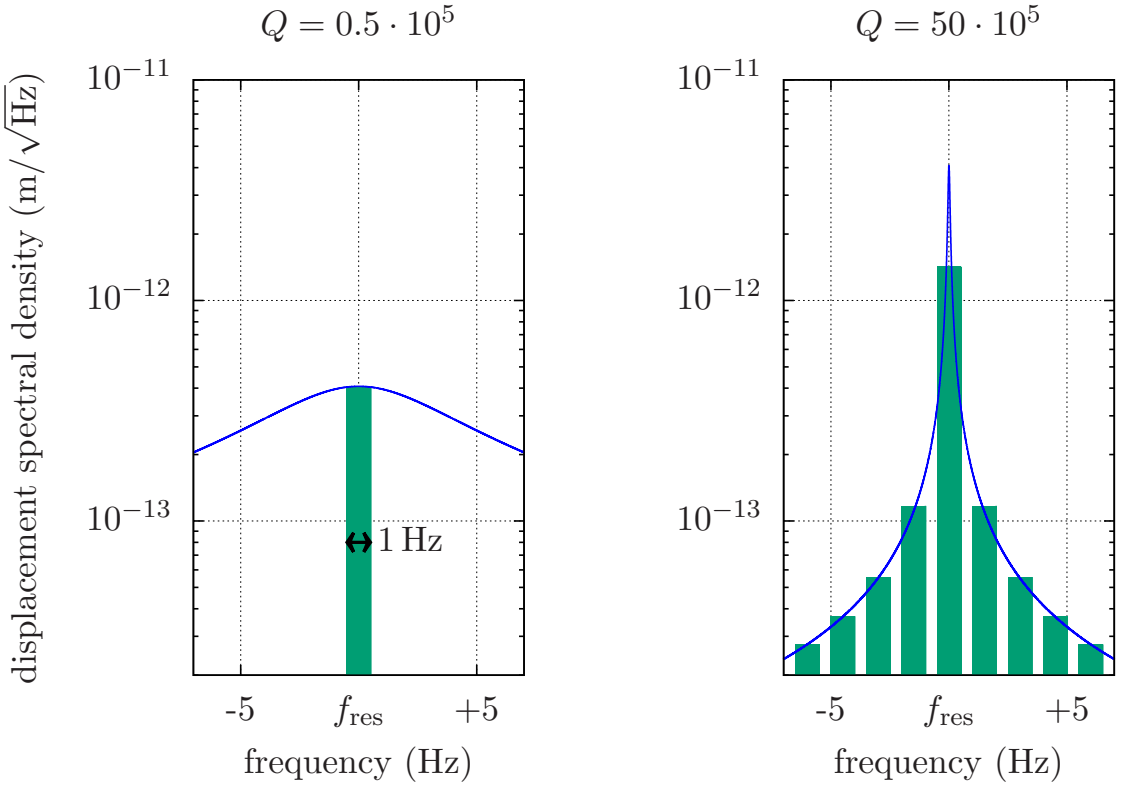

Figure 7.4: The influence of the resolution bandwidth of the spectrum analyzer on the measured data: The graphs show two theoretical displacement spectral sensitivites caused by thermal noise for a resonance peak of the membrane with $f_{\text{res}}^{1,1} = 406.0\,\text{kHz}$ and $m_{\text{eff}} = 71\,\text{ng}$ at a temperature of 100 K, assuming two different quality factors. A measurement point of the analyzer is the integral over the frequency band of the resolution bandwidth, in this case RBW = 1 Hz. The peak on the left has a quality factor of $Q = 0.5 \cdot 10^5$ and a full width half maximum of FWHM = 8 Hz. The integral over 1 Hz around the resonance matches with the maximum of the curve with a deviation of $< 0.5\,\%$. On the right a peak for a quality factor of $Q = 50 \cdot 10^5$ and a full width half maximum of FWHM = 0.08 Hz is pictured. In this case the actual signal on resonance is three times higher than the measured integral. On the slopes however the measured power values conform with the actual peak shape.

signal. In conclusion, the shape of the peak slopes have more significance for the data evaluation than the points on resonance for a peak narrower than the RBW.

One can also take advantage of measurements with resolution bandwidths broader than the peak. For example in [88] a high RBW was chosen on purpose to assure that the data point on resonance is an integral over the whole peak width. Therefore the measured value could be used to calculate the temperature directly with equation (3.40) instead of determining the area under the peak from all measured data points as it was done in the presented work in section 7.3.2.

The instability of the readout quadrature: In section 6.3.2 the feedback control loop to stabilize the phase between the local-oscillator field and the interferometer output field is described. This technique allowed to keep the readout angle stable in the amplitude quadrature. To change the phase, one mirror in the local-oscillator path was attached to a piezo-electric actuator, such that the path length could be controlled by applying a voltage. The interference of the sidebands on the local oscillator and the signal field resulted in a sufficient error signal. Unfortunately for the chosen low input power, the error signal was not strong enough for a stabilized phase. In consequence the voltage on the piezo-electric actuator could only be adjusted manually during the measurements.

In figure 7.5 a zero-span measurement for an input power of $P_{\mathrm{in}} = 1\,\mathrm{mW}$ at the resonance frequency $f_{\mathrm{res}}^{1,1} = 414.7\,\mathrm{kHz}$ is shown. For a stabilized readout amplitude quadrature, such a measurement would result in a line on the level of the peak height with the fluctuations of the thermal noise. In the shown graph, a triangular voltage was applied on the actuator. As the thermal noise peak is measured as an amplitude modulation, the spectral density was maximal in the amplitude quadrature. In the phase quadrature, the peak completely disappeared and the spectral density reached the shot-noise level. The measurement demonstrates the strong dependency of the peak height on the readout angle. For the record of a proper resolved peak tip, it is required to stay on the maximum of the curve for the sweep time of $\mathrm{ST} = 1.9\,\mathrm{s}$. As this stability was not given, a resulting error in the data needs to be considered.

The fluctuations of the peak height: As the readout angle in the experiment was not stabilized, a minimal measurement time had to be chosen for the presented spectra. Every data point recorded by the spectrum analyzer therefore was the representation

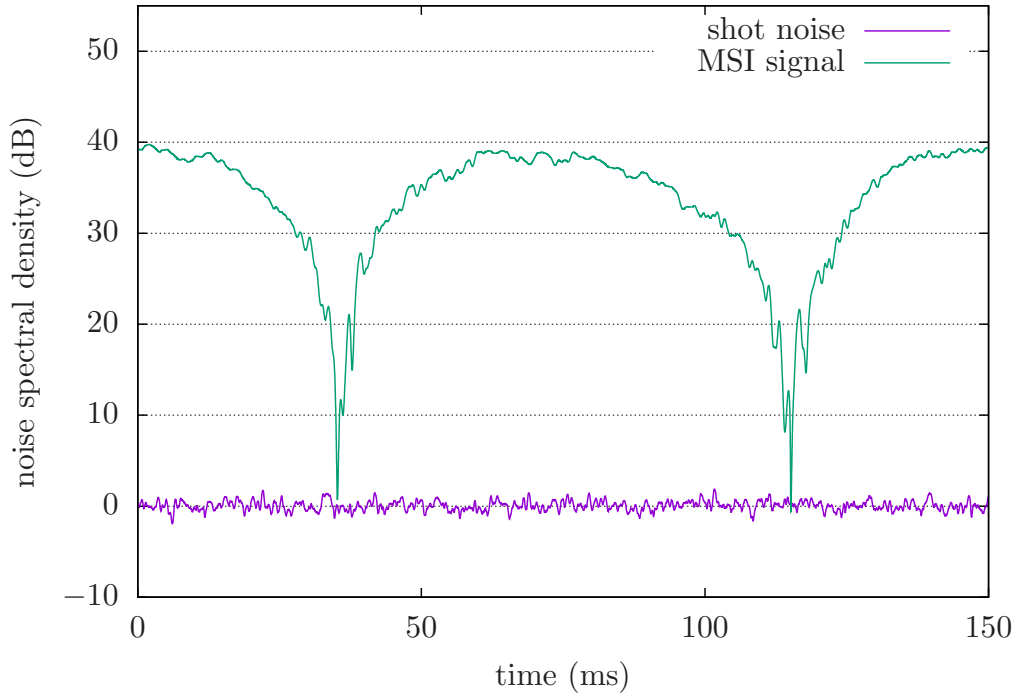

Figure 7.5: Zero-span measurement of the noise spectral density at the membrane resonance frequency $f_{\mathrm{res}}^{1,1} = 414.7\,\mathrm{kHz}$: This data was recorded with an input power of $P_{\mathrm{in}} = 1\,\mathrm{mW}$, a local-oscillator power of 11 mW, a resolution bandwidth RBW = 10 kHz, a video bandwidth VBW = 10 kHz and a sweep time of ST = 150 ms. It was normalized to the vacuum shot noise. The phase between the local oscillator and the signal field was scanned by applying a triangular voltage on a piezo-actuated mirror in the local-oscillator path. In the phase quadrature the curve reached the shot noise. The membrane resonance peak only contributed to the noise in the amplitude quadrature which corresponded to the maximum of the curve.

of one short time interval. The peak is caused by the Brownian thermal noise. As the Brownian motion inside the membrane is a stochastic process, the motion of the particles is completely random. It induces fluctuations in the stress, the thickness and the optical properties of the material [89]. Thus, a measurement of the noise on resonance in a short time window is not representative for the maximum on a larger time scale. Averaging the data over a longer time scale might allow a measurement of better resolved peak tips. An alternative could be to choose a longer sweep time (ST) of the analyzer to increase the time window for a single data point. The sweep time determines the time for one measurement. It depends on how long a mixing product stays in the bandpass of the intermediate-frequency filter of the analyzer. The ST is directly connected to the resolution bandwidth via

$$\mathrm{ST} = \frac{k(\mathrm{span})}{\mathrm{RBW}} \tag{7.3}$$

with a span-dependent proportionality constant k(Span). For Gaussian filters k(span) has typical values in the 2 to 3 range [87]. Usually spectrum analyzer couple the setting of the ST directly to the RBW and VBW. By increasing the automatic value, the accuracy of the measurement could be improved.

7.3.2 The Quality Factor and the Mode Temperature of the Membrane

For the measurements presented in the following parts, an input power of $P_{\mathrm{in}} = (50 \pm 5)\,\mu\mathrm{W}$ was chosen to assure that the laser amplitude noise stayed below the vacuum shot-noise level and that the effect of the injected squeezed states was measurable later on. To determine the quality factors and the mode temperatures, spectra around the fundamental frequencies $f_{\mathrm{res}}^{1,1} = 414.7\,\mathrm{kHz}$ at a temperature $T = 293\,\mathrm{K}$ and $f_{\mathrm{res}}^{1,1} = 406.0\,\mathrm{kHz}$ at a temperature $T = 100\,\mathrm{K}$ were recorded at the dark fringe. With the measured membrane power reflectivity $r_{\mathrm{m}}^2 = 0.19 \pm 0.005$ from section 3.1 and the wavelength $\lambda = 1550\,\mathrm{nm}$, the theoretical shot-noise level according to equation (3.23) for the input power $P_{\mathrm{in}} = (50 \pm 5)\,\mu\mathrm{W}$ was:

$$\sqrt{S_{\mathrm{SN,x}}^{\mathrm{MSI}}} = (1.01^{+0.09}_{-0.07}) \cdot 10^{-14}\ \frac{\mathrm{m}}{\sqrt{\mathrm{Hz}}}\ . \tag{7.4}$$

With this value the measured noise spectral density was calibrated via equation (7.2). The resulting displacement spectral density for $T = 293\,\mathrm{K}$ is shown in figure 7.6. To fit the theoretical data, the contributions of the thermal noise and the shot noise needed

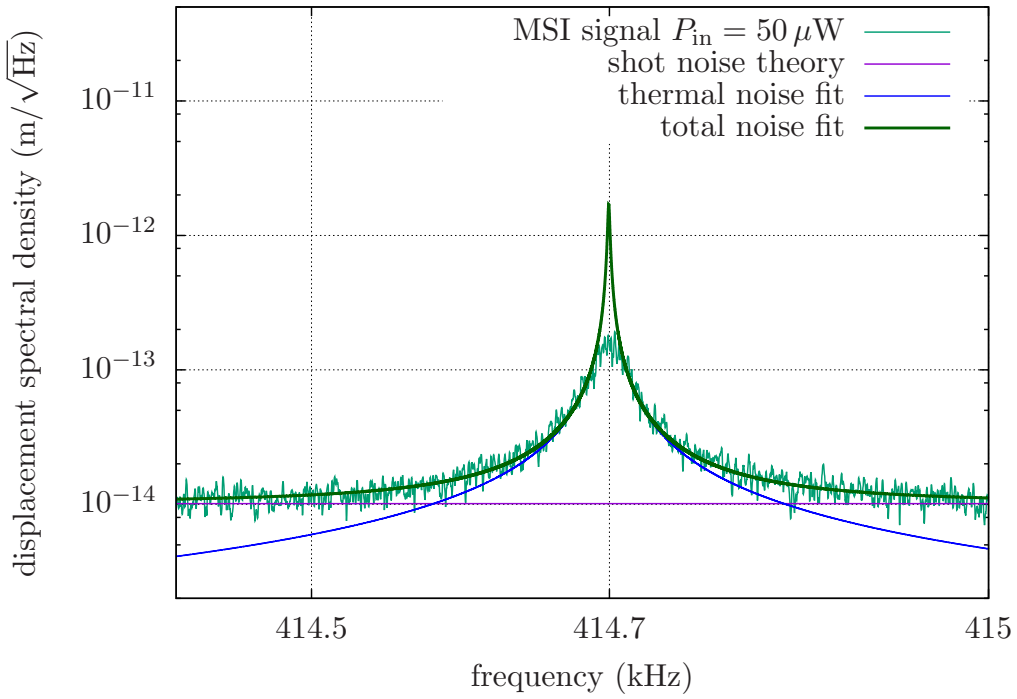

Figure 7.6: Displacement spectral density around the (1,1) resonance peak of the membrane at room temperature: The used input power was $(50 \pm 5)\,\mu$W. The resolution bandwidth was RBW = 1 Hz, the video bandwidth VBW = 1 Hz and the sweep time ST = 1.9 s. The shown data was averaged 20 times. The shot-noise level was calculated from a 20 times averaged measurement without signal. The data measured with the balanced homodyne detector was calibrated via equation (7.2) with the theoretical value for the vacuum shot-noise level given in equation (7.4) to receive the displacement spectral density in m/$\sqrt{\text{Hz}}$. For the shown model of the total noise in green with the effective mass $m_{\text{eff}} = (71 \pm 5)$ ng and the temperature $T = 293$ K, the data was fitted with the quality factor as free parameter, yielding to the value $Q_{293} \approx 2.7 \cdot 10^5$. In the frequency range of $\approx \pm 50$ Hz around the peak, the thermal noise given by equation (3.38) and shown in blue was dominating.

to be considered. The total noise calculated as:

$$\sqrt{S^{\mathrm{MSI}}_{\mathrm{tot,x}}} = \sqrt{S^{\mathrm{MSI}}_{\mathrm{SN,x}} + S^{\mathrm{x}}_{\mathrm{temp}}} \tag{7.5}$$

with the shot noise $S^{\mathrm{MSI}}_{\mathrm{SN,x}}$ given by equation (7.4) and the thermal noise $S^{\mathrm{x}}_{\mathrm{temp}}$ given by equation (3.38). To fit the model to the measured data with the quality factor Q_{293} as free parameter, the calculated effective mass $m_{\mathrm{eff}} = (71 \pm 5)\,\mathrm{ng}$ and the measured temperature $T = 293\,\mathrm{K}$ with the thermometer on the membrane holder were used. For the resulting function shown in green, a quality factor of the membrane of

$$Q_{293} \approx 2.7 \cdot 10^5 \tag{7.6}$$

was determined, which corresponded to a full width half maximum of

$$\mathrm{FWHM}_{293} = \frac{f_{\mathrm{res}}}{Q_{293}} \approx 0.7\,\mathrm{Hz}\ . \tag{7.7}$$

The slopes of the model fit well to the shape of the data, whereas the height of the measured peak of $\sqrt{S^{\mathrm{MSI}}_{\mathrm{max,\,293}}} = (2.5 \pm 0.3) \cdot 10^{-13}\,\frac{\mathrm{m}}{\sqrt{\mathrm{Hz}}}$ was 6 times lower than the one of function. The integral over $[f_{\mathrm{res}} - \frac{\mathrm{RBW}}{2}, f_{\mathrm{res}} + \frac{\mathrm{RBW}}{2}]$ with $\mathrm{RBW} = 1\,\mathrm{Hz}$ for the model would result in a value only 1 % below the theoretical maximum. The influence of the resolution bandwidth explained in section 7.3.1 should therefore not be high. Therefore it is assumed that the also discussed fluctuations of the peak height and the instability of the readout quadrature caused this discrepancy. The pure theoretical thermal noise $S^{\mathrm{x}}_{\mathrm{temp}}$ given by equation (3.38) is shown for the determined quality factor in the blue curves in figure 7.6 and 7.2. Its slopes off resonance fit to all the measured spectra at room temperature for different input powers in the thermal noise dominated regime.

For the model it was assumed, that absorptions in the material didn't induce a major heating, such that the temperature measured at the membrane holder was valid for the membrane as well. The mode temperature of the membrane is proportional to the integral of the thermal displacement spectral density $S^{\mathrm{x}}_{\mathrm{vis}}(\Omega)$. It was calculated by equation (3.40), which is independent of the quality factor and therefore could be applied directly on the measured data. From the area under the measured spectrum in the frequency range of $\pm 75\,\mathrm{Hz}$ around the resonance frequency and the calculated effective mass $m_{\mathrm{eff}} = (71 \pm 5)\,\mathrm{ng}$ followed a mode temperature of

$$T^{\mathrm{MSI}}_{\mathrm{mode,293}} = (341^{+129}_{-87})\ \mathrm{K}. \tag{7.8}$$

The error bars result from the mass density of the membrane given in [54] and the squared shot noise given in equation (7.4) that was used to calibrate the data. In addition an error of 10 % was assumed due to the unstable readout quadrature as explained in section 7.3.1. Within the error bars the determined mode temperature conforms to the temperature measured with the thermometer. This result confirms that the applied calibration method was valid.

The measurement was repeated at a temperature of 100 K. Figure 7.7 shows the displacement spectral density around the fundamental mode for an input power of $(50 \pm 5)\,\mu$W calibrated with the same transformation given in equation (7.2) for the theoretical shot-noise level given in equation (7.4). Two additional side peaks on the slopes with a difference to the carrier frequency of $\approx \pm 20$ Hz were visible. An explanation could be so called *satellite modes*, modes of other components in the setup, that were excited by acoustic vibrations coupling in. The resulting oscillations at much lower frequencies beat with the membrane resonance and show as upper and lower side bands distorting the peak's shape. A probable origin of such modes could be the stack of *attocube* positioners, onto which the membrane holder was attached. These devices contained springs for the stepping mechanism, which made them possible candidates for the occurrence of oscillations. An older interferometer design described in [34] had comparable positioners for its steering mirrors, that also were causing satellite modes. During the measurement the turbo pump was running, which could be a source of vibrations exciting the satellite modes. In addition oscillations of the membrane silicon frame, induced by light hitting it on the edge, could have had an influence.

The shown model for the sum of the relevant noise sources $\sqrt{S_{\mathrm{tot,x}}^{\mathrm{MSI}}}$ given in equation (7.5) was fitted to the slopes for a temperature $T = 100$ K and an effective mass $m_{\mathrm{eff}} = (71 \pm 5)$ ng, which resulted in a quality factor of the membrane of

$$Q_{100} \approx 1.5 \cdot 10^6 \ , \tag{7.9}$$

which corresponded to a full width half maximum of

$$\mathrm{FWHM}_{100} = \frac{f_{\mathrm{res}}}{Q_{100}} \approx 0.3\,\mathrm{Hz} \ . \tag{7.10}$$

One expects an increase of the quality factor for lower temperatures [90], which could also be observed in this case. For the fitted models, the quality factor was almost an order of magnitude higher than at room temperature. In the measured data the

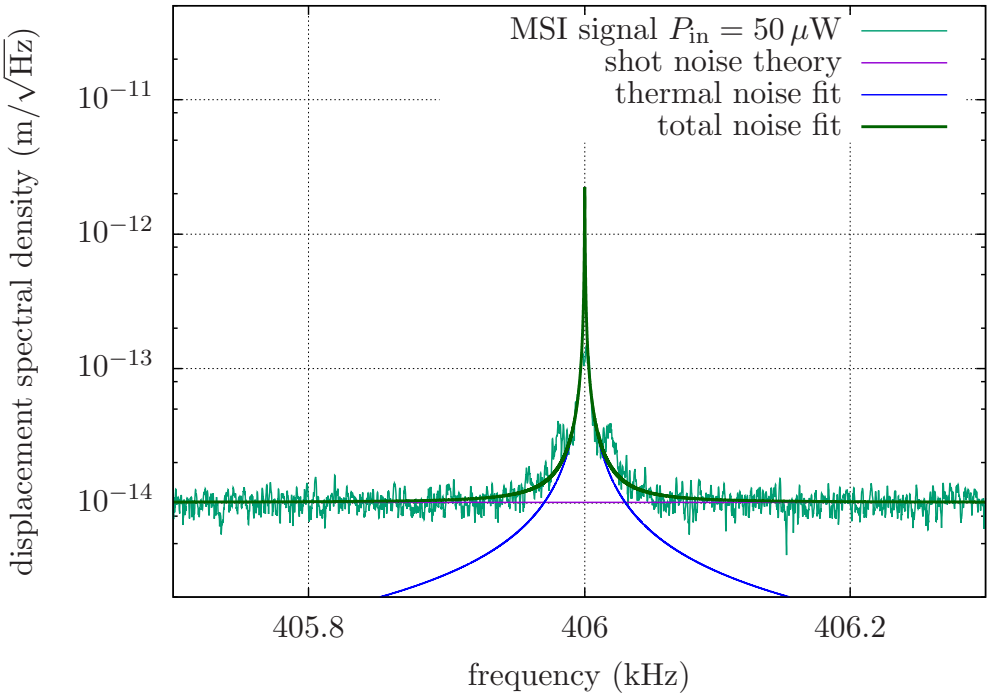

Figure 7.7: Displacement spectral density around the (1,1) resonance peak of the membrane at 100 K: The used input power was $(50 \pm 5)\,\mu$W. The resolution bandwidth was RBW = 1 Hz, the video bandwidth VBW = 1 Hz and the sweep time ST = 1.9 s. The shown data was averaged 20 times. The shot-noise level was calculated by averaging the data points off resonance. The data measured with the balanced homodyne detector was calibrated via equation (7.2) with the theoretical value for the vacuum shot-noise level given in equation (7.4) to receive the displacement spectral density in m/$\sqrt{\text{Hz}}$. For the shown model of the total noise in green with the effective mass $m_{\text{eff}} = (71 \pm 5)$ ng and the temperature $T = 100$ K, the data was fitted with the quality factor as free parameter, yielding to the value $Q_{100} \approx 1.5 \cdot 10^6$. In a frequency band of $\approx \pm 15$ Hz the total noise was dominated by the thermal noise given by equation (3.38) and shown in blue. At $\approx \pm 20$ Hz satellite modes were visible on the slopes.

increase showed as a narrower peak at $T = 100\,\mathrm{K}$. However the measured height of the peak $\sqrt{S^{\mathrm{MSI}}_{\mathrm{max},\,100}} = (1.6 \pm 0.4) \cdot 10^{-13} \frac{\mathrm{m}}{\sqrt{\mathrm{Hz}}}$ was a factor of 15 lower than the value from the corresponding fit and therefore even smaller than the one at $T = 293\,\mathrm{K}$.

The integral over $[f_{\mathrm{res}} - \frac{\mathrm{RBW}}{2}, f_{\mathrm{res}} + \frac{\mathrm{RBW}}{2}]$ of the given total noise function yields to a value a factor of 2 below the theoretical maximum. Therefore the limited RBW is an explanation why the peak tip at the lower temperature was resolved even worse than the one at room temperature as explained in section 7.3.1.

The blue curves in the figures 7.6 and 7.2 show the impact of the thermal noise $S^{\mathrm{x}}_{\mathrm{temp}}$ given by equation (3.38) for the determined quality factor. For a frequency band of $\pm 50\,\mathrm{Hz}$ around the resonance frequency, the area under the measured displacement spectral density was calculated from the data points. Using the effective mass $m_{\mathrm{eff}} = (71 \pm 5)\,\mathrm{ng}$, equation (3.40) yielded to a mode temperature of

$$T^{\mathrm{MSI}}_{\mathrm{mode},100} = (81^{+38}_{-23})\ \mathrm{K}\ . \tag{7.11}$$

For the narrower peak a manual adjustment of the readout quadrature was more inaccurate and therefore an error of 20 % was assumed because of the missing stabilization as described in section 7.3.1. Combined with the errors for the mass and the scaling factor given in equation (7.4), this results in the given uncertainty of the determined mode temperature.

In conclusion, quality factors of $Q_{293} \approx 2.7 \cdot 10^5$ and $Q_{100} \approx 1.5 \cdot 10^6$ were determined at the temperatures $T = 300\,\mathrm{K}$ and $T = 100\,\mathrm{K}$ from calibrating and fitting the data measured with the spectrum analyzer. The mentioned influences show, that the measurement of quality factor values with this method is possible with a limited accuracy.

7.4 The Enhancement of the Interferometer Sensitivity using Squeezed States

7.4.1 The Detection of the Produced Squeezed States

Off resonance the displacement spectral density of the Michelson-Sagnac interferometer was limited by the vacuum shot noise around the resonance frequencies of $f^{1,1}_{\mathrm{res}} = 414.7\,\mathrm{kHz}$ at room temperature and $f^{1,1}_{\mathrm{res}} = 406\,\mathrm{kHz}$ at $T = 100\,\mathrm{K}$ for an input

power of $(50 \pm 5)\,\mu$W. Thus the condition to detect an enhancing effect of injected squeezed states was fulfilled. But before taking this step, the squeezed-state source was characterized. To measure the maximum detectable squeeze factor in the relevant frequency range, the squeezed states were sent at first directly to the balanced homodyne detector as illustrated in figure 4.9. The phase between the squeezed vacuum field and the local oscillator was stabilized with a feedback loop using the frequency-shifted control field described in section 6.3.2.

As explained in section 4.3.2, stabilizing the temperature of the PDC cavity was crucial for the squeezed-state generation. In this case of a doubly-resonant PDC cavity, the temperature had to be chosen such, that it could be resonant for the fundamental and the doubled frequency for the same length. The closer this temperature was to the phase matching temperature of the crystal, the higher was the efficiency as explained in section 4.1.4. Within the range of the used temperature controller, this was possible for the three temperatures 25.3 °C, 37.8 °C and 49.6 °C. In [38] I characterized the performance of the source for all three temperatures. For this work the temperature of 37.8 °C was chosen, for which the highest squeezing could be reached.

The second important parameter was the pump power of the frequency-doubled light. This power was varied to determine the power of the highest reachable shot-noise reduction for a sideband frequency of 400 kHz close to the fundamental mode of the membrane. The homodyne detector signal was fed into the spectrum analyzer and zero-span measurements were recorded to examine the performance. The reached squeeze and antisqueeze factors are plotted against the pump power in figure 7.8. The values were normalized to the vacuum shot noise of the local oscillator. As expected the antisqueeze factors were higher than the squeeze factors for all pump powers due to optical loss. Above a pump power of 11.8 mW, the detected squeezing did decrease, but the antisqueezing still increased.

Using equation (4.31) an average detection efficiency of

$$\eta^2_{\text{direct}} = 0.878 \pm 0.013 \tag{7.12}$$

was reached for the data for the pump powers up to 11.8 mW. The optical losses appeared at various points. An unavoidable loss was caused by the limited quantum efficiency of the photodiodes for the homodyne detection. For a good adjustment the

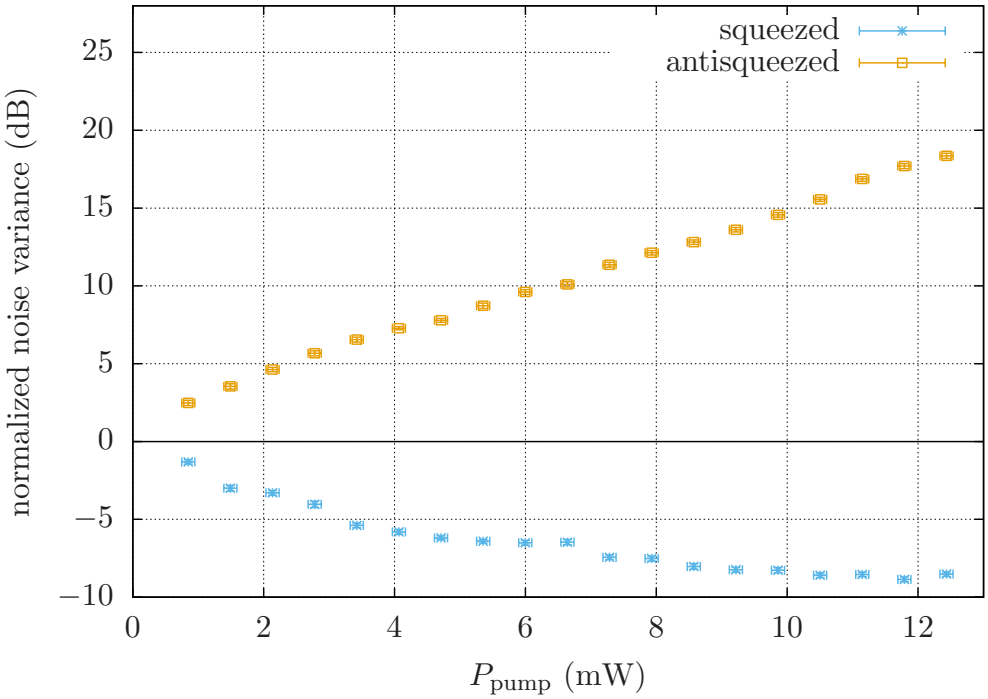

Figure 7.8: Measured squeeze and antisqueeze factor depending on the pump power resulting from zero-span measurements at 400 kHz: The resolution bandwidth for the zero-span measurements was RBW = 50 kHz, the video bandwidth VBW = 5 kHz and the sweep time ST = 0.2 s. The data measured with the balanced homodyne detector was averaged 20 times. The local-oscillator power was 20.5 mW, which resulted in a vacuum shot-noise level of 21.9 dB over dark noise at this frequency. The data was normalized to the shot noise and the electronic dark noise of the detector was subtracted. For different pump powers of the 775 nm light, the reached squeeze and antisqueeze value were determined.

loss was estimated to be $\leq 2\,\%$. For the adjustment beam of the PDC cavity to the diagnose mode-cleaner cavity a mode matching of $99.5\,\%$ was reached, for the local oscillator $99.9\,\%$. According to equation (4.34) this determined an upper limit for the loss due to imperfect mode overlap of $1 - 0.994^2 \approx 1.2\,\%$. All optics in the path were superpolished and had high reflective coatings. The beamsplitter was made of suprasil3001, a material with absorption in the order of magnitude of 1 ppm [91]. Thus, the propagation loss given by equation (4.33) was assumed to be $< 0.5\,\%$. The escape efficiency given by equation (4.36) depended on the transmission of the coupling mirror and the round trip loss inside the PDC cavity. According to the specifications given by the coating company *Laseroptik GmbH*, the losses at the antireflective coating on the plane side of the crystal and the transmission at the high reflective curved side summed up to $\approx 0.1\,\%$. Following from the power transmission $t_{\mathrm{m}}^2 = 0.15$ of the coupling mirror the calculated escape efficiency was $\eta_{\mathrm{escape}}^2 \approx 0.99$, which corresponded to a loss of $1\,\%$.

The estimated sum of optical losses $L_{\mathrm{tot}} \approx 5\,\%$ could not explain the experimentally determined loss of $(12.2 \pm 1.3)\,\%$. Therefore one could assume the presence of phase jitter, an unstable phase relation between the local oscillator and the signal field degrading the detected squeezing as described in section 4.2.3. Two other indications for this effect were observed. The first was the decrease of the detected squeeze factor for pump powers above 11.8 mW. The second was, that a shot-noise reduction of $-10.2\,\mathrm{dB}$ was measured with the same PDC cavity in [38] at a sideband frequency of 1 MHz and a pump power of 15 mW. As a consequence, the detection of higher squeezing with higher pump powers was possible at higher frequencies with the setup. Another cause for lower detected squeezing for higher pump powers was the reliability of the control loop for the readout quadrature. The narrower the squeezing ellipse became, the more fragile was the stabilization of the phase.

The maximum squeezing was detected for a pump power of 11.8 mW. A squeeze factor of $(-8.7 \pm 0.2)\,\mathrm{dB}$ and an antisqueeze factor of $(17.9 \pm 0.2)\,\mathrm{dB}$ were achieved. In the error bars a maximum fluctuation of $5\,\%$ of the local-oscillator power was considered, that could have caused a shift of the vacuum shot-noise level over time. Subtracting the electronic dark noise of the homodyne detector resulted in a squeeze factor of $(-8.9 \pm 0.2)\,\mathrm{dB}$. The corresponding zero-span measurement without dark-noise correction is pictured in figure 7.9. Besides the squeezing and antisqueezing data for a stabilized phase, a measurement for a varying readout phase is shown. A triangular voltage was applied to the piezo-electric mirror resulting in a rotation of the squeezing

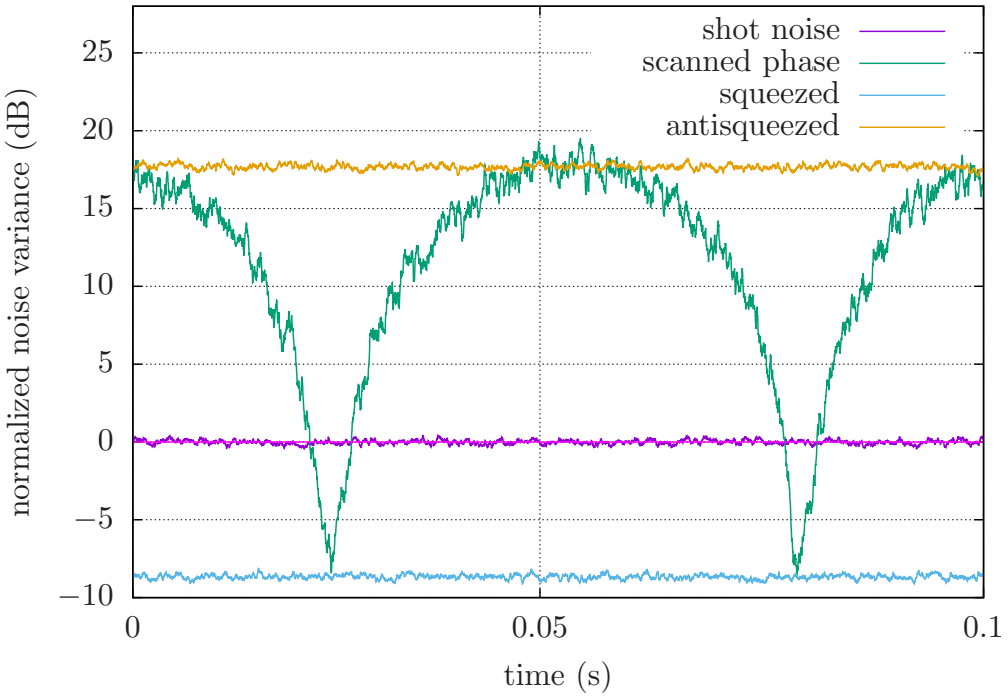

Figure 7.9: Zero-span measurement of the squeezed and antisqueezed noise, measured directly on the homodyne detector at 400 kHz: The pump power of the 775 nm light in this measurement was $P_{\text{pump}} = 11.8\,\text{mW}$, the resolution bandwidth was RBW = 50 kHz, the video bandwidth VBW = 5 kHz and the sweep time ST = 0.1 s. The local-oscillator power was 20.5 mW which resulted in a vacuum shot-noise level of 21.9 dB over electronic dark noise at this frequency. The data was normalized to the shot noise. The green curve shows the measurement for a scanned phase between the local oscillator and the signal field, the other lines were averaged 20 times. The achieved squeeze factor was $(-8.7 \pm 0.2)\,\text{dB}$, the corresponding antisqueeze factor was $(17.9 \pm 0.2)\,\text{dB}$. In the graph, the electronic dark noise was not subtracted, a subtraction resulted in a squeeze factor of $(-8.9 \pm 0.2)\,\text{dB}$.

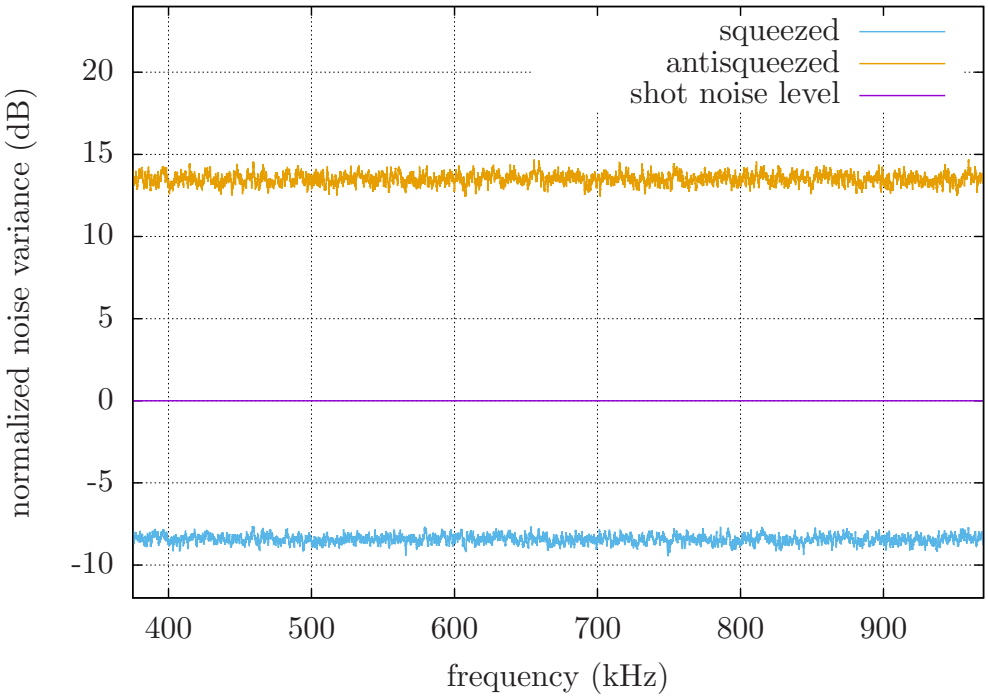

Figure 7.10: Broad-spectrum measurement of squeezed states: The shown measurements of the squeezed and antisqueezed noise were measured directly with the homodyne detector and normalized to the vacuum shot noise. The data was averaged 20 times. The local-oscillator power was 20.5 mW which resulted in a vacuum shot-noise level of ≥ 15 dB over dark noise in this range. The pump power of the 775 nm light was $P_{\text{pump}} = 9.2$ mW. The resolution bandwidth was RBW = 30 kHz, the video bandwidth VBW = 5 kHz and the sweep time ST = 0.5 s. As this spectrum of the squeezed noise shows, the reached squeezing and antisqueezing values were consistent over the frequency range of the lower-order resonance peaks of the membrane for the used pump power. As the electronic dark noise varied over this range, it was subtracted from the measurements.

ellipse in time.

As the laser amplitude noise decreased for higher frequencies, it could be an option to choose a membrane with a higher resonance frequency or to look at higher-order resonances of the current membrane in the future to be quantum-noise limited for higher laser powers. For this reason the frequency dependence of the squeeze factor was measured for the frequency range of sufficiently low electronic dark noise of the used homodyne detector. In the range of 350 kHz to 950 kHz the shot-noise level was at least 15 dB above dark-noise level for the local-oscillator power of 20.5 mW. The resulting spectrum is shown in figure 7.10. The used pump power was 9.2 mW. As

the darknoise was frequency dependent, it was subtracted.

The spectrum shows that the squeezing and antisqueezing factors were consistent for this pump power in the chosen frequency range. In average a squeeze factor of $(8.4 \pm 0.2)\,\mathrm{dB}$ and an antisqueeze factor of $(13.5 \pm 0.2)\,\mathrm{dB}$ were measured. The squeeze factor was slightly higher than the dark-noise corrected one of a zero-span measurement with the same pump power of $(8.3 \pm 0.2)\,\mathrm{dB}$. The discrepancy laid within the error bars and could also be explained with an additional error in measuring the pump power. The antisqueeze factor of the spectrum was also consistent with the measured value of $(13.6 \pm 0.2)\,\mathrm{dB}$ in the zero-span measurement at 400 kHz.

7.4.2 The Detection of the Squeezed States Injected into the Interferometer

Before sending bright input light and squeezed states into the Michelson-Sagnac Interferometer simultaneously as shown in the setup in figure 6.7, only the squeezed states injected into the interferometer were measured. The bright input light was only used to adjust the membrane displacement for the dark fringe and was blocked afterward. This step was crucial to avoid optical losses because of a too high transmission of the interferometer for the squeezed states.

Compared to the direct squeezing measurement from section 7.4.1, the phase control loops and the length of the PDC resonator were less stable. An explanation could be, that the isolation of the Faraday rotator was not perfect, such a that part of the signal was reflected back to the PDC resonator disturbing its length stabilization. This effect also showed in a reduction of the threshold power. For pump powers above 11 mW the cavity was lasing. A pump power lower than for the direct detection proved to provide a maximum squeezing value. This was an indication that additional phase noise appeared in the interferometer, causing an additional jitter of the readout phase.

Figure 7.11 shows a zero-span measurement of the detected squeezed and antisqueezed noise in reflection of the Michelson-Sagnac Interferometer with blocked input light P_{in} of the interferometer at a frequency of 400 kHz. The pump power was 9.2 mW and the phase for the squeezed and antisqueezed data series was stabilized. The green curve shows the noise for a a measurement with a scanned phase. Therefore a triangular voltage was applied on the piezo-actuated mirror. To compare the measurement with the directly detected squeezing as measured in section 7.4.1, the corresponding data for the same pump power is given by the dashed lines. When the squeezed states

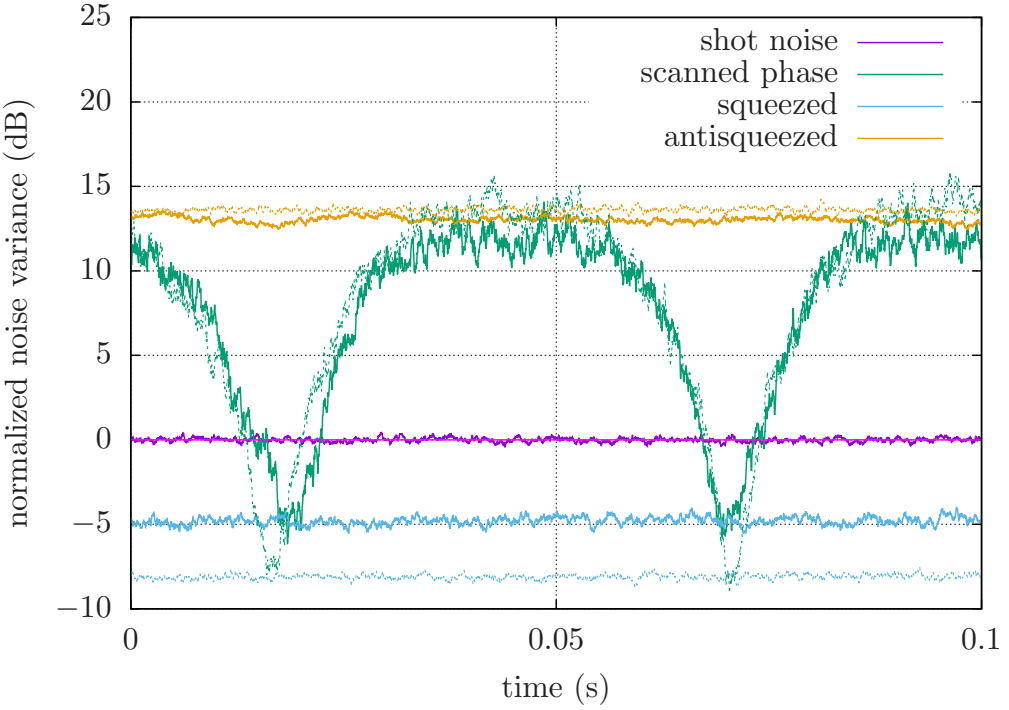

Figure 7.11: Zero-span measurement of the squeezed and antisqueezed noise after the injection into the Michelson-Sagnac interferometer at 400 kHz without bright input light: The pump power of the 775 nm light in this measurement was $P_{\mathrm{pump}} = 9.2\,\mathrm{mW}$, the resolution bandwidth was RBW = 50 kHz, the video bandwidth VBW = 5 kHz and the sweep time ST = 0.1 s. The data measured with the balanced homodyne detector was normalized to the vacuum shot noise. The local-oscillator power was 20.5 mW which resulted in a vacuum shot-noise level of 21.9 dB over the electronic dark noise at this frequency. The green curve shows the measurement for a scanned phase between the local oscillator and the signal field, the other lines were averaged 20 times. The dashed lines show the measured signals for a direct squeezing measurement without injection into the interferometer for the same pump power. In reflection of the interferometer, the antisqueezing value dropped from $(13.6 \pm 0.2)\,\mathrm{dB}$ to $(13.0 \pm 0.2)\,\mathrm{dB}$ and the squeezing from $(-8.1 \pm 0.2)\,\mathrm{dB}$ to $(-4.8 \pm 0.2)\,\mathrm{dB}$. The electronic dark noise was not subtracted.

were detected directly, a squeeze factor of $(-8.1 \pm 0.2)\,\mathrm{dB}$ and an antisqueeze factor of $(13.6 \pm 0.2)\,\mathrm{dB}$ were detected. In reflection of the interferometer these values were degraded to a squeeze factor of $(-4.8 \pm 0.2)\,\mathrm{dB}$ and an antisqueeze factor of $(-13.0 \pm 0.2)\,\mathrm{dB}$. Subtracting the electronic dark noise resulted in a squeeze factor of $(-4.9 \pm 0.2)\,\mathrm{dB}$. As a consequence the detection efficiency calculated via equation (4.31) decreased from $\eta^2_{\mathrm{direct}} = 0.878 \pm 0.013$ to

$$\eta^2_{\mathrm{MSI}} = 0.701 \pm 0.015\ . \tag{7.13}$$

In the error bars of the given values a maximum fluctuation of 5 % of the local-oscillator power was considered again, that could have caused a shift of the shot-noise level over time.

The squeezed states reflected by the interferometer experienced additional optical losses. Their path is shown in figure 6.7. The used Faraday rotator by the company *Qioptiq* was hand-selected by the distributor *soliton* to guarantee a minimum transmission of $t_{\mathrm{f}}^2 = 0.96$. My measurement of the transmission delivered a value of $t_{\mathrm{f}}^2 \approx 0.985$ for a clean TEM_{00} mode and $t_{\mathrm{f}}^2 \approx 0.98$ for a slightly elliptical beam. The used polarizing beamsplitter showed a maximum reflection of $r^2_{\mathrm{PBS,s}} \approx 0.995$ and a maximum transmission $t^2_{\mathrm{PBS,p}} \approx 0.99$ for the optimized polarizations. Considering that the squeezed vacuum states were reflected by the beamsplitter, passed the Faraday rotator twice and transmitted through beamsplitter, the loss added up to $\approx 5.5\,\%$. The imperfect contrast of the interferometer caused another $1 - 99.7\,\% = 0.3\,\%$ loss. In addition the reached mode matching of the adjustment beam to the reference cavity was 1 % lower than for the degraded case. Therefore an increase of the resulting optical loss of 2 % due to a decreased visibility was assumed.

Again the sum of additional optical losses of $\approx 8\,\%$ could not explain the observed degrading of the detection efficiency. Therefore additional phase jitter caused by components of the Michelson-Sagnac interferometer was assumed to be the cause for the lower than expected measured squeeze factor.

As in section 7.4.1 a spectrum of the squeeze and antisqueeze factor for a broad frequency range was measured with the same pump power. The data is shown in figure 7.12. As the electronic dark noise was frequency dependent, it was subtracted. The measurement shows that the achieved squeezing and antisqueezing is consistent over

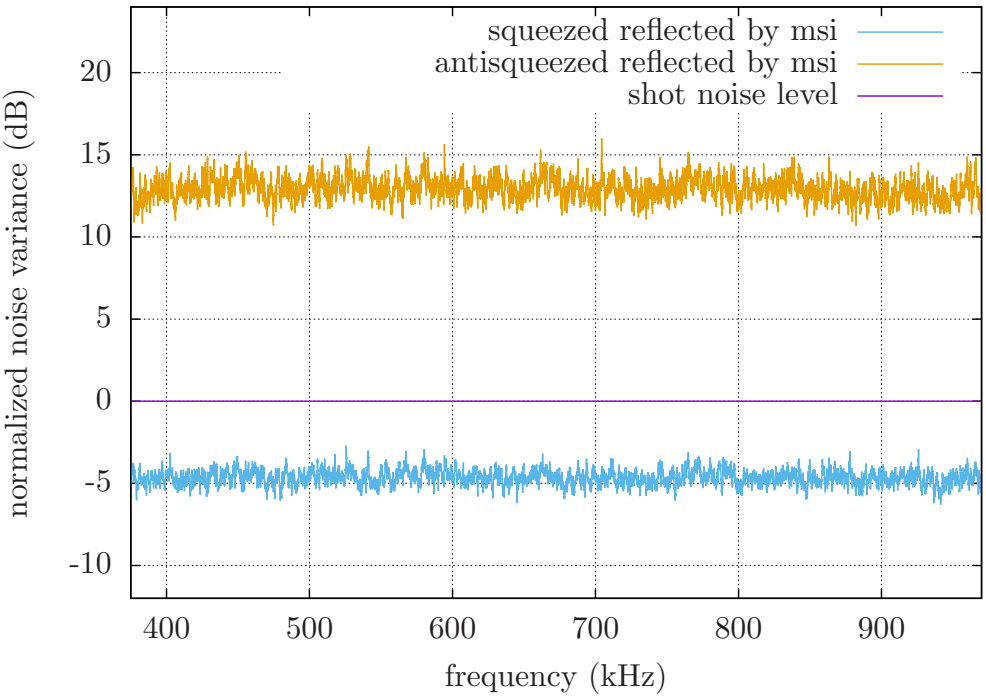

Figure 7.12: Broad-spectrum measurement of squeezed states injected into the Michelson-Sagnac interferometer without bright input light: The shown data of the squeezed and antisqueezed noise was normalized to the vacuum shot noise. The data measured with the balanced homodyne detector was averaged 20 times. The local-oscillator power was 20.5 mW which resulted in a vacuum shot-noise level of ≥ 15 dB over dark noise in this range. The pump power of the 775 nm light was $P_{\text{pump}} = 9.2$ mW. The resolution bandwidth was RBW = 30 kHz, the video bandwidth VBW = 5 kHz and the sweep time ST = 0.1 s. As this spectrum of the squeezed noise shows, the reached squeezing and antisqueezing values were consistent for this pump power in the frequency range of the lower-order resonance peaks of the used membrane. As the electronic dark noise varied over this range, it was subtracted from the measurements.

this range from 350 kHz to 950 kHz. In average an antisqueeze factor of (12.9 ± 0.2) dB and a squeeze factor of (-4.43 ± 0.20) dB were measured. These values were consistent with the results from the zero-span measurement at 400 kHz.

7.4.3 The Enhancement of the Interferometer Sensitivity

Up to this point the interferometer displacement spectral density with bright input light and the squeezed states injected into the interferometer were measured separately. The next step was to measure the displacement spectral density with bright interferometer input light and injected squeezed vacuum states. The interferometer input power at 1550 nm was $P_{\text{in}} = (50 \pm 5)\,\mu$W to assure that the signal off resonance was shot-noise limited and the results were comparable to the measurement with only coherent light in the figures 7.6 and 7.7. For the squeezed-light source a 775 nm pump power of 9.2 mW was used, as for this power the maximum squeezing was achieved in the measurement shown in figure 7.11. The membrane was placed such, that the dark fringe condition was fulfilled to achieve a minimum output power and minimum optical losses. The squeezing angle was stabilized using the feedback control loops from section 6.3.2. The power of the interferometer input field of the interferometer was too low to receive an error signal for the stabilization of its phase relation to the squeezed states and the local oscillator. Therefore this phase needed to be adjusted manually by applying a voltage to the piezo-actuated mirror in the path.

The recorded spectrum around the resonance frequency $f_{\text{res}}^{1,1} = 414.7$ kHz of the (1,1) mode at room temperature is shown in figure 7.13. The data was calibrated with the theoretically calculated shot noise with the transformation given in equation (7.2). To reduce the shot noise, the injected nonclassical states needed to be squeezed in the phase quadrature in respect to the bright light in the interferometer. By injecting states, that were squeezed in the amplitude quadrature and antisqueezed in the phase quadrature, the shot noise could be amplified. As comparison the spectrum is also shown for the initial signal with blocked PDC resonator output. This peak's slopes went down to the vacuum shot-noise level of the local oscillator. Unfortunately the electronic dark noise of the homodyne detector contained several peaks around this resonance frequency. Thus, the dark noise needed to be subtracted from the data to achieve the shown enhancement.

From the data off resonance followed a squeeze factor of (3.1 ± 0.2) dB and an antisqueeze factor of (11.8 ± 0.2) dB. The error bars were caused by a possible maximum

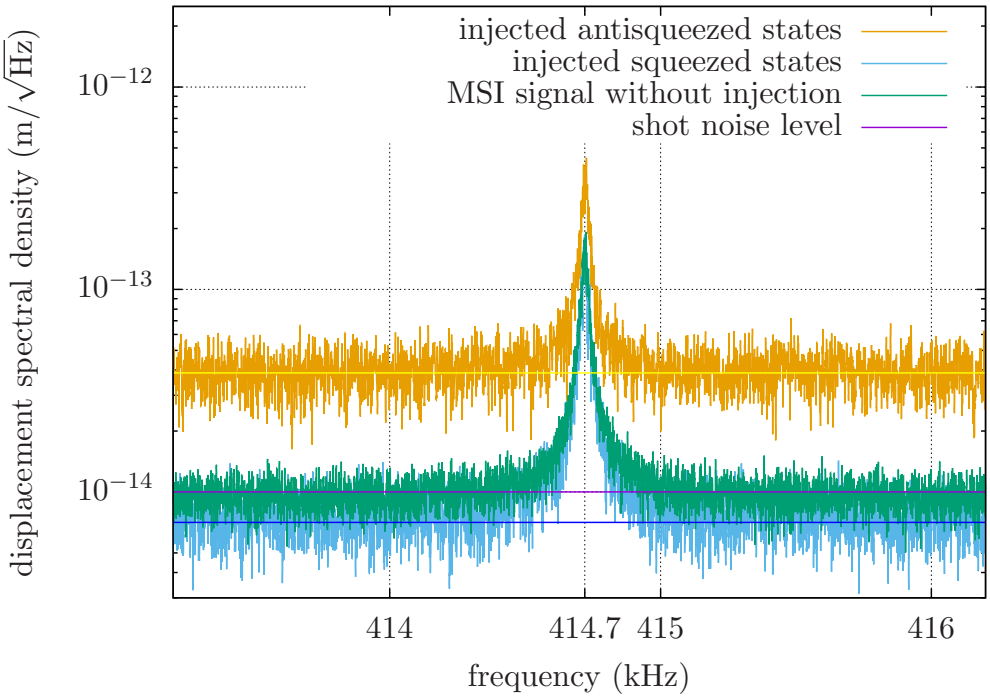

Figure 7.13: Enhanced displacement spectral density around the (1,1) resonance peak of the membrane with injected squeezed states at room temperature: The shot noise of the initial signal for an input power of $(50 \pm 5)\,\mu$W could be reduced by (3.1 ± 0.2) dB by injecting states, that were squeezed in the phase quadrature in respect to the bright light in the MSI. This corresponded to a sensitivity improvement by a factor of $\sqrt{2}$. By injecting states, that were squeezed in the amplitude and antisqueezed in the phase quadrature, the shot noise was increased by (11.8 ± 0.2) dB. The pump power of the 775 nm light was $P_{\text{pump}} = 9.2$ mW. The resolution bandwidth was RBW = 1 Hz, the video bandwidth VBW = 1 Hz and the sweep time ST = 1.9 s. The shown data was averaged 8 times for the antisqueezed and squeezed measurement and 20 times for the measurement without injection. The shot noise level was averaged 20 times and the average value is shown as reference. Because of the peaks in the electronic noise of the homodyne detector at this frequency, the dark noise was subtracted.

fluctuation of 5 % of the local-oscillator power, that could cause a shift of the shot-noise level over time. Compared to the measurement without bright input light, the squeeze factor decreased. One reason could be the laser amplitude noise, that had more impact for lower shot noise. Another explanation was the missing phase stabilization of the signal field in respect to the local oscillator during the measurement. Therefore the phase might have drifted during the sweep time of ST = 1.9 s. When bright light was sent into the interferometer, the length stabilization of the PDC resonator became more fragile because of signal light reflected by the polarizing beamsplitter due to the imperfect Faraday rotator. This effect might have caused additional phase noise. Nevertheless, the enhancement of the displacement spectral density by injecting squeezed states was successfully demonstrated with a shot-noise reduction by a factor of $\sqrt{2}$.

The same measurement was repeated at a temperature of 100 K. The resulting displacement spectral density is shown in figure 7.14. At the shifted resonance frequency of $f_{\mathrm{res}}^{1,1} = 406.0\,\mathrm{kHz}$, the homodyne detector showed a constant dark-noise clearance of 20.7 dB for the used 19.5 mW local-oscillator power, such that the electronic dark noise didn't need to be subtracted. From the data off resonance followed a reached squeeze factor of (3.1 ± 0.2) dB and an antisqueeze factor of (11.4 ± 0.2) dB. Therefore at 100 K the reached enhancement from the room temperature could be reproduced without the subtraction of electronic noise.

The presented measurements show a reduction of the shot noise of above 3 dB, which corresponds to a factor of $\sqrt{2}$. Thus the sensitivity-enhancing effect of injected squeezed states for a quantum-noise limited spectrum in an optomechanical measurement was successfully demonstrated at room temperature and at 100 K. For an optimized setup that allows the usage of higher coherent input powers for the interferometer, a stabilization of the signal-field phase in respect to the local oscillator will be possible. Then probably higher squeeze factors will be reachable. Using techniques further explained in chapter 8 in the future, a radiation-pressure-noise limited displacement spectral sensitivity might be realized. Then the total quantum noise could be reduced below the standard quantum limit by injecting squeezed states.

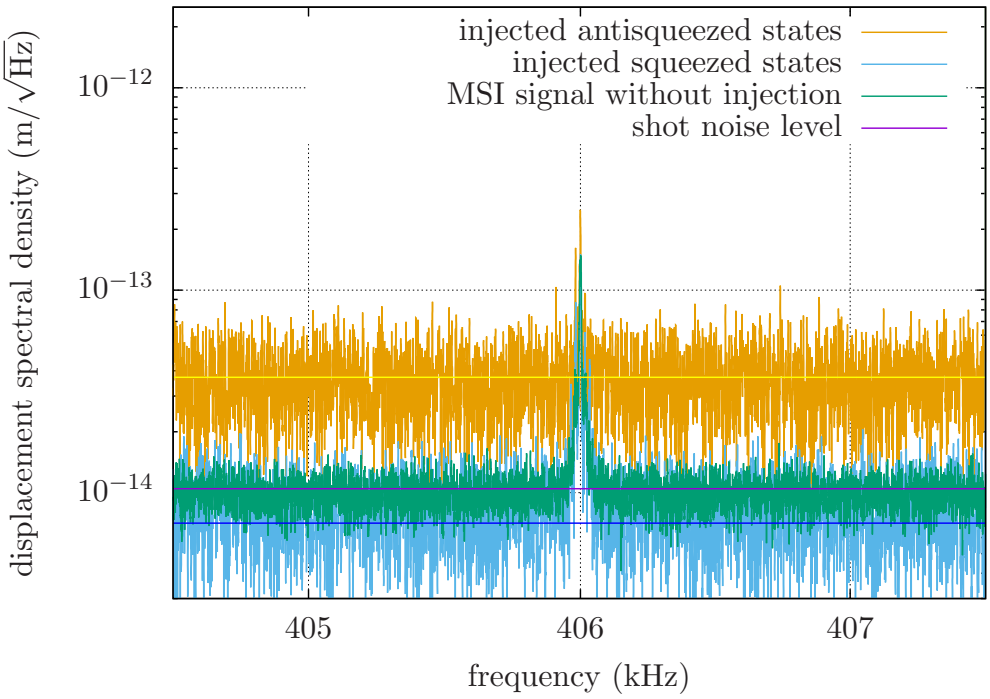

Figure 7.14: Enhanced displacement spectral density around the (1,1) resonance peak of the membrane with injected squeezed states at 100 K: The shot noise of the initial signal for an input power of $(50 \pm 5)\,\mu$W could be reduced by (3.1 ± 0.2) dB by injecting states, that were squeezed in the phase quadrature in respect to the bright light in the MSI. The sensitivity improvement by a factor of $\sqrt{2}$ from room temperature was therefore reproduced. By injecting states, that were squeezed in the amplitude and antisqueezed in the phase quadrature, the shot noise was increased by (11.4 ± 0.2) dB. The pump power of the 775 nm light was $P_{\mathrm{pump}} = 9.2$ mW. The resolution bandwidth was RBW = 1 Hz, the video bandwidth SBW = 1 Hz and the sweep time ST = 1.9 s. The shown data measured with the balanced homodyne detector is averaged 6 times for the antisqueezed and squeezed curve and 20 times for the case without injection. The shot-noise level was calculated from the signal off resonance without the injection of nonclassical states. It was 20.7 dB above the electronic dark noise for the used local-oscillator power of 19.5 mW. This data was not dark-noise corrected.

8 Next Steps

The presented results in the previous chapter demonstrate the enhancement of the sensitivity of an optomechanical experiment, the Michelson-Sagnac interferometer, by injecting externally produced squeezed states. With a few upgrades it will be possible to perform measurements at lower temperatures, to improve the contrast and to reach higher squeeze factors. In the future the quality factor of the membrane will be determined with a ring-down measurement. To take advantage of the squeezed states to reach the radiation pressure noise and to overcome the standard quantum limit, the implementation of an active laser amplitude stabilization and of a signal-recycling mirror will be required.

8.1 General Upgrades to Improve the Setup

The membrane positioner: Even though a temperature of 15 K at the membrane holder could be reached, the presented measurements were recorded at a temperature of 100 K in figure 7.7. At lower temperatures, one of the *attocube* positioners to adjust the membrane angle did not move anymore, thus no sufficient contrast could be reached. An exchange of this part will allow to perform the experiment at the minimum temperature that the cryostat provides.

The stack of *attocube* positioners for the membrane adjustment is a possible candidate for the origin of the satellite modes, that appeared in the spectrum at 100 K. If the upgrade of the positioner doesn't have a positive effect on the peak shape, it will be investigated how to stabilize the membrane holder to damp vibrations. One idea is to implement springs between the membrane holder and the interferometer spacer.

Another improvement could be achieved by screwing the membrane onto the holder using clamps instead of creating a stiff connection with glue to reduce the occurrence of stress on the frame.

The beamsplitter: During the adjustment process described in section 6.2.2 one issue was clipping of the beam inside the interferometer. To avoid hitting the frame of the membrane, a waist size much smaller than the membrane size must be chosen. However the smaller the waist is, the more the beam diverges and the probability, that it gets cut off on the edges of the steering mirrors, the beamsplitter or the vacuum tank windows, increases. The observed clipping is suspected to occur at the beam-

splitter holder due to its long distance from the waist position and the small size of the hole in the current design. In the presented work a trade-off between a small waist size on the membrane and avoiding clipping at the other components had to be made. The measured waist diameter was 270 μm. Nevertheless, the satellite modes on the detected peak might be caused by light hitting the membrane frame.

A first step to avoid this clipping is the redesign of the beamsplitter holder. The used optic had a diameter of 1 inch, but the holder only had a 0.5 inch wide opening. This size can easily be increased. As a second step, the beamsplitter will be exchanged. Even though the design angle for perfect balancing was 45°, the best balancing was reached for 45.5°. As the interferometer is designed symmetrically, this error results in a discrepancy between the configuration for hitting the optics in the middle and the configuration for perfect balancing. A new beamsplitter with 50/50 splitting ratio at 45° will solve this issue. The quality of the new beamsplitter's antireflective coating has been measured by Pascal Gewecke in [81]. Its reflective coefficient is below 100 ppm, which is lower than the reflective coefficient of the coating of the current beamsplitter of 170 ppm for 45° and 260 ppm for 45.5° [34]. Thus the exchange of the beamsplitter could allow to reach higher contrast values, such that the laser amplitude noise at the dark fringe will be reduced. In addition, the contribution of the laser amplitude noise occuring on the beamsplitter will decrease for a better balancing, such that a total reduction of the laser amplitude noise in the output signal is expected.

Reducing incoupling vibrations of the vacuum pumps: During the presented measurements the turbo pump was running to keep the low pressure in the vacuum chamber stable. Due to its functionality, it produces vibrations, that might have coupled into the experiment despite the oscillation damping by the isolation stage. Using an ion-getter pump instead could reduce the vibrations, that excite the satellite modes.

Reducing the Phase Noise of the Squeezed Light The squeezed states for the injection into the interferometer were produced with a comparably low pump power for the PDC resonator. Higher squeezing values could be detected directly with the balanced homodyne detector for higher pump powers, however the length stabilization of the resonator showed fluctuations when the states were injected into the interferometer. In figure 6.7 the setup with the injection via the Faraday rotator and a polarizing beamsplitter was shown. Due to the imperfection of these components a small fraction of the light from the interferometer was reflected to the PDC resonator and disturbed

its length stabilization. This effect will be suppressed by adding an isolator in the path of the squeezed states. In combination with a $\lambda/2$ waveplate and two polarizing beamsplitters, a second Faraday rotator will rotate the polarization of the incorrectly reflected light such, that it can be filtered out with the PBS. This isolation will improve the stability of the PDC resonator length, such that higher pump powers can be used. Thus, the squeeze factor of the injected states can probably be increased.

8.2 Determination of the Quality Factor via Ring-Down Measurement

To measure radiation pressure noise, reaching a high quality factor of the silicon nitride membrane will become of interest. As the presented evaluation of the spectra showed, a determination from the spectrum analyzer data is only possible by fitting the slopes of the peak with a theoretical model. In the future a more exact value will be required for a proper interpretation of the data. A common approach to measure the quality factor are so called *ring-down* measurements.

The membrane is excited with its known resonance frequency and the resulting fluctuation of the light power is measured with a photodetector. Depending on the decay time τ, the initial power P_0 decreases exponentially with the time t to

$$P = P_0 e^{\frac{t}{\tau}} \ . \tag{8.1}$$

From a measurement of this dependence, τ can be determined, which is directly connected to the quality factor via [88]

$$Q = \pi f_{\mathrm{res}} \tau \ . \tag{8.2}$$

The challenge occurring for the presented Michelson-Sagnac interferometer is the excitement of the silicon nitride membrane. The quality factor strongly depends on the stress induced by the clamping or gluing as well as on the attached components. Additionally it is temperature dependent and changes when the membrane is cooled to cryogenic temperatures. Therefore it is no option to perform the ring-down measurement before implementing the membrane into the interferometer.

The interferometer and therefore the membrane are isolated from incoupling vibrations with the damping stage shown in section 6.1.2, which is designed to suppress exactly

the relevant frequency band. A common approach is the attachment of a piezo-electric actuator directly to the experiment or to the vacuum tank. By applying a voltage, the membrane can be excited [92][88]. In the presented setup a vibration from outside would not couple into the experiment, thus the actuator would have to be inside the tank. However these devices are usually not suitable for a performance at low temperatures and they would be an additional component that could cause oscillations disturbing the spectrum. Therefore an attachment directly onto the interferometer or the membrane holder should be avoided.

The oscillations of the membrane could also be excited by an amplitude modulation of the incoming light, but in the case of equal light powers on both sides with the same arm lengths, the pressures would cancel each other out. Thus, this option could only be realized if one arm was blocked or misaligned on purpose. But even then the incoming light would have to be blocked to measure the decay time and an additional probe beam would be required for the readout.

As the interferometer already contains cryogenic actuators, one could consider to apply a voltage with the resonance frequency on them to excite the membrane. However, they are not designed for frequencies in this order of magnitude. The maximum frequency to apply on the *Janssen* positioners given by the company is 600 Hz, thus they can not be used for this purpose [84]. The classification of the *attocube* positioners states a maximum drive velocity of 1 $\frac{\text{mm}}{\text{s}}$ [83]. The controller by the company does not allow output frequencies in the kHz regime, however one could consider to connect self-built electronics. Because of the velocity limit, only a low amplitude could be applied after consulting the manufacturer. Nevertheless, as the membrane is directly attached to the actuator, the resulting excitement should be sufficient for a ring-down measurement.

8.3 The Laser Amplitude Stabilization

The presented measurements with the Michelson-Sagnac interferometer were taken with an input power of $P_{\text{in}} = 50\,\mu\text{W}$ to avoid a domination of technical laser amplitude noise. Besides the resulting low radiation pressure noise, the performance of the experiment at such a low power had another disadvantage. The error signal to stabilize the phase between the local oscillator and the interferometer output signal was too small to keep the readout quadrature stable. To allow measurements with higher input powers, the amplitude of the used light will be actively stabilized in the

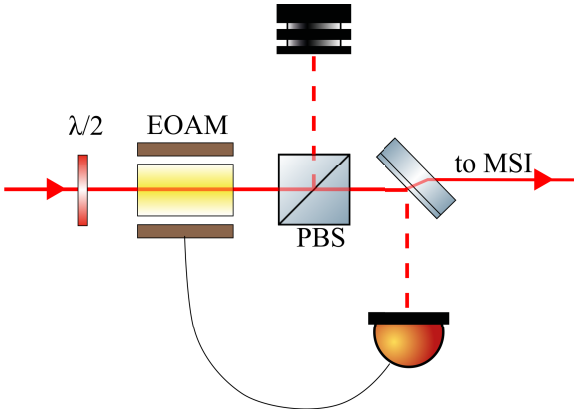

Figure 8.1: Example setup for an active laser stabilization for the interferometer input field: The electro-optic amplitude modulator (EOAM) serves as a power actuating device. The photodiode measures a fraction of the transmitted power as a reference value for an error signal. With a feedback loop the voltage on the modulator is regulated, determining the transmission through the polarizing beamsplitter.

future.

For such a scheme, a power actuating device, as for example an electro-optic amplitude modulator (EOAM), needs to be implemented as shown in figure 8.1. In transmission of the device a small fraction of the power is detected as a reference. The measured power is compared to a defined value and their difference is used as an error signal for a feedback loop regulating the voltage on the EOAM. By controlling this voltage, the transmitted light through the polarizing beamsplitter will have a more stable amplitude [35]. The successful performance of this technique was demonstrated in [93].

8.4 Signal Recycling

In section 3.3.2 the order of magnitude of the quantum radiation pressure noise in the Michelson-Sagnac interferometer was regarded theoretically. As a result, an input power in the order of magnitude of 10 kW would be required to reach the standard quantum limit over a broad frequency range for the current setup. Besides the fact, that the used laser system does not provide such a high power, several issues would occur. A high input power would cause a thermal lens in the beamsplitter, which would decrease the contrast. On the other hand the balanced homodyne detector can only handle a limited output power of the interferometer, thus the contrast of the interferometer would have to be unrealistically high to allow a measurement at the

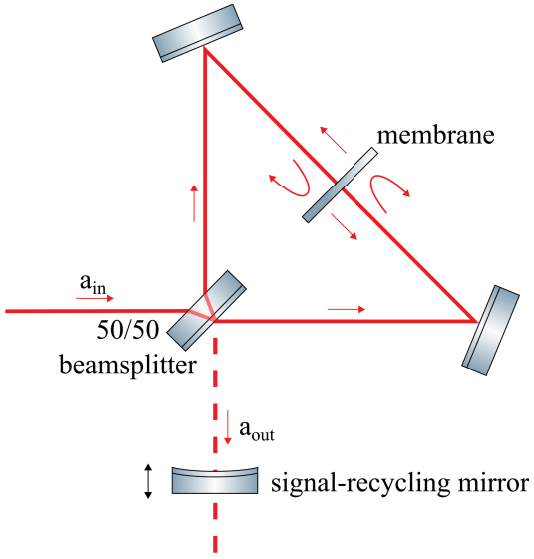

Figure 8.2: The Michelson-Sagnac interferometer with signal-recycling mirror: By placing a high-reflective mirror in the output, a signal-recycling cavity between the mirror and the membrane is formed. If the cavity is resonant for the TEM_{00} mode, the signal is amplified, such that a radiation-pressure-noise limited displacement spectral density can be realized for lower input powers. In addition other modes than the TEM_{00} mode are filtered out as they don't fulfill the resonance condition.

dark fringe. In addition the membrane would heat up because of absorption [35].

To amplify the output signal of an interferometer without increasing the input power, Meers suggested the concept of signal recycling [94]. In [31] the idea of using the signal-recycling principle for a Michelson-Sagnac interferometer was proposed and it has already successfully been applied in [30] to observe optomechanical cooling.

As illustrated in figure 8.2 a high-reflective mirror with tunable position is placed into the output of the interferometer and a high fraction of the signal is retroreflected to the membrane. The two components now form a cavity, that amplifies the output field when the resonance condition is fulfilled. The cavity length is stabilized with a feedback control loop using an additional control field. It should be mentioned, that this scheme does not work for a perfect dark fringe as in this case any output light to generate an error signal for the stabilization would be eliminated. To avoid loosing signal through the input port of the interferometer, the cavity should be undercoupled, which is the case for $r_{\mathrm{MSI}} > r_{\mathrm{SR}}$. In consequence the interferometer contrast limits the reflectivity, that can be chosen for the signal-recycling mirror.

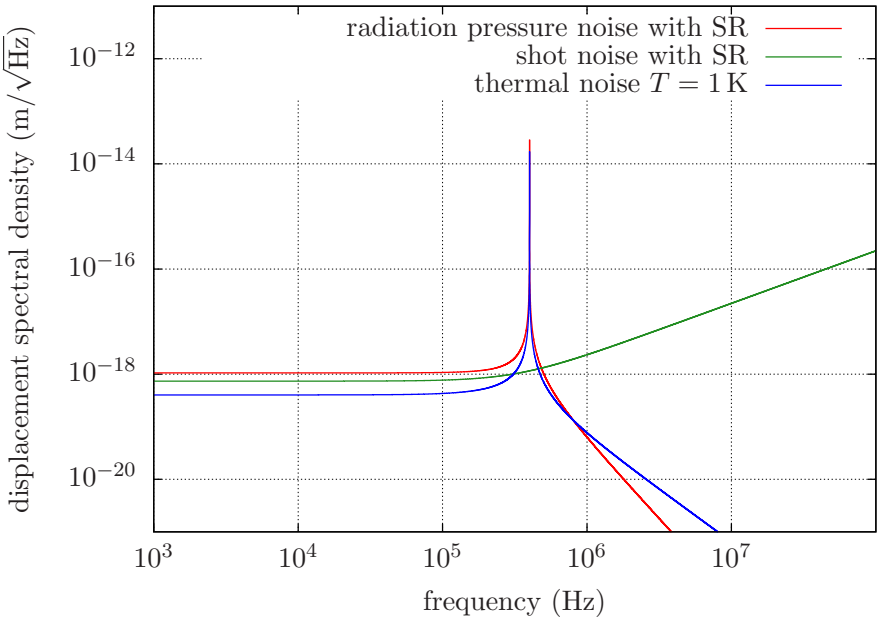

Figure 8.3: Signal recycled quantum radiation pressure noise and shot noise for $P_{\mathrm{in}} = 1\,\mathrm{W}$ and thermal noise for $T = 1\,\mathrm{K}$: The radiation pressure noise is given by equation (8.5), the shot noise by equation (8.6) and the thermal noise by equation (3.38). The signal-recycling mirror power reflectivity is $r_{\mathrm{SR}}^2 = 0.999$. The used parameters in this theoretical curves are a quality factor of $Q = 10^6$, a thickness of $d_{\mathrm{m}} = 100\,\mathrm{nm}$, an effective mass of $m_{\mathrm{eff}} = (71 \pm 5)\,\mathrm{ng}$ and a resonance frequency of $f_{\mathrm{res}} = \frac{\Omega_0}{2\pi} = 400\,\mathrm{kHz}$. Due to the amplified signal, a radiation-pressure-noise dominated displacement spectral density is reached for a 10^4 times lower input power than in figure 3.6, where an input power of 10 kW was suggested.

For a distance l between the membrane and the beamsplitter, a cavity length l_{SR} and a signal-recycling mirror with a power reflectivity r_{SR}^2 the cutoff frequency is

$$\Omega_{\mathrm{SR}} = \frac{c(1 - r_{\mathrm{SR}})}{2(l_{\mathrm{SR}} + l)} \ . \tag{8.3}$$

The factor

$$G_{\mathrm{SR}} = \frac{1 + r_{\mathrm{SR}}}{1 - r_{\mathrm{SR}}} \tag{8.4}$$

is called the recycling gain factor. The shot-noise and the quantum-radiation-pressure displacement spectral densities from equations (3.23) and (3.25) change to [31]:

$$\sqrt{S_{\mathrm{SN,x}}^{\mathrm{MSI,\ SR}}} = \sqrt{\frac{\hbar c \lambda}{16\pi G_{\mathrm{SR}} r_{\mathrm{m}}^2 P_{\mathrm{in}}}} \sqrt{1 + \left(\frac{\Omega}{\Omega_{\mathrm{SR}}}\right)^2} \ , \tag{8.5}$$

$$\sqrt{S_{\mathrm{RPN,x}}^{\mathrm{MSI,\ SR}}} = |H(\Omega)| \sqrt{\frac{16\pi\hbar G_{\mathrm{SR}} r_{\mathrm{m}}^2 P_{\mathrm{in}}}{c\lambda}} \sqrt{\frac{1}{1 + (\frac{\Omega}{\Omega_{\mathrm{SR}}})^2}} \ . \tag{8.6}$$

In figure 3.6 the quantum radiation pressure noise and shot noise without signal recycling was pictured for an input power of $P_{\mathrm{in}} = 10\,\mathrm{kW}$. Figure 8.3 shows a comparable plot for a signal-recycled interferometer with power reflectivity $r_{\mathrm{SR}}^2 = 0.999$ and an input power of $P_{\mathrm{in}} = 1\,\mathrm{W}$. Because of the cavity effect a radiation-pressure-noise limited sensitivity can be reached for an input power that is 10^4 times lower. An additional advantage is the suppression of other modes than the TEM_{00}. The reflected light of the antireflective coating of the beamsplitter or stray light most probably does not fulfill the resonance condition and does not get amplified. Therefore a signal-recycling mirror has a contrast-improving effect [35][34].

In the design for the Michelson-Sagnac-interferometer spacer presented in section 6.1.2, the implementation of a signal-recycling cavity in the future was already considered. With an additional triangular positioner by *Janssen precision engineering*, the signal-recycling mirror can be attached to the gold coated Invar block in the output port.

9 Summary and Outlook

The results of this work demonstrate, that the application of squeezed states can enhance the sensitivity of optomechanical measurements. In this context a Michelson-Sagnac interferometer with a silicon nitride membrane was presented and the principle and setup of the used squeezed-light source was described and characterized.

The squeezed states for the application in the presented work were produced via degenerate parametric down-conversion (PDC). To induce this nonlinear process, a pump field of double the frequency was required, that was produced with the inverse nonlinear process, the second-harmonic generation (SHG) [8]. For both processes crystals of periodically poled potassium titanyl phosphate were inserted into resonators to achieve a high conversion efficiency. The PDC cavity was resonant for both relevant wavelengths to generate squeezed states with a low pump power.

In contrast to the injection of externally produced states for a sensitivity enhancement, as applied in current gravitational-wave detectors, the squeezed states can also be produced directly inside a cavity of a detector by inserting a nonlinear crystal as suggested in [24]. Using the built squeezed-light source, a proof-of-principle experiment was performed to demonstrate this effect. A phase-modulation signal of an interferometer was mimicked by generating side bands on a light field at several frequencies using an electro-optic modulator. The light was sent through the PDC cavity, which was simultaneously pumped with frequency-doubled light. This way, a Fabry-Perot interferometer for optomechanical measurements with a nonlinear medium inside was imitated. As a result the noise was reduced, but also the signal was affected. However, the deamplification of the signal was lower than the squeezing of the noise, such that an improvement of the sensitivity-bandwidth product of 36 % could be demonstrated experimentally. In the future this technique could be applied in interferometric detectors in addition to the injection of squeezed states from an external source to take advantage of both effects [33].

The optomechanical experiment investigated in this work contained a silicon nitride membrane as mechanical oscillator. Such membranes have high quality factors and low masses which makes them good candidates to investigate radiation pressure noise. The 100 nm thick membrane for this experiment had a window size of 1 mm × 1 mm and an effective mass of (71 ± 5) ng. The measured power reflectivity was $r_{\mathrm{m}}^2 = 0.19 \pm 0.005$.

Therefore its transmission was too high to use it as an end mirror of an interferometer without having to deal with high optical loss. For this reason the topology of a Michelson-Sagnac interferometer as suggested in [31] was chosen. The two sides of the membrane acted as end mirrors of both arms of a Michelson interferometer, the light transmitted in both directions formed a Sagnac interferometer.

The measured total noise of the interferometer showed contributions of the thermal noise, the laser amplitude noise and the shot noise. A future goal is to reach a radiation-pressure-noise limited displacement spectral density. As theoretical estimations have shown, the membrane needs to be cooled to decrease the thermal noise beyond the radiation-pressure-noise level. Therefore the interferometer was designed for a performance at low temperatures and placed inside a cryostat. Cryogenic positioners provided the option to adjust the membrane and the steering mirrors from the outside with electronic controllers. The overlap of the outcoming modes was optimized such, that a contrast of 99.7 % with an unbalancing of the beamsplitter of $\Delta_{\mathrm{bs}} = |r_{\mathrm{bs}}^2 - t_{\mathrm{bs}}^2| = 0.12\,\%$ was achieved.

The measurements of the interferometer signal were taken at the dark fringe, the point of destructive interference of the Michelson mode and therefore the lowest output power. The fundamental mode of the inserted membrane was observed at a frequency of $f_{\mathrm{res}}^{1,1} = 414.7\,\mathrm{kHz}$ for room temperature and at $f_{\mathrm{res}}^{1,1} = 406.0\,\mathrm{kHz}$ for a temperature of $T = 100\,\mathrm{K}$. With an input power of $50\,\mu\mathrm{W}$, the laser amplitude noise was low enough to realize a shot-noise limited sensitivity off resonance. The peak at the lower temperature showed satellite modes on its slopes, that were probably caused by low frequency resonances of other interferometer components. The measured noise spectra were calibrated with the theoretical shot-noise level. By fitting the resulting displacement spectral density on the peak slopes with the theoretical models for the total noise, the quality factors of the membrane $Q_{293} \approx 2.7 \cdot 10^5$ at room temperature and $Q_{100} \approx 1.5 \cdot 10^6$ for a temperature of $T = 100\,\mathrm{K}$ were determined. The experimental mode temperatures $T_{\mathrm{mode,300}}^{\mathrm{MSI}} = (341^{+129}_{-87})\,\mathrm{K}$ and $T_{\mathrm{mode,100}}^{\mathrm{MSI}} = (81^{+38}_{-23})\,\mathrm{K}$, calculated from the area under the peaks, conformed to the temperatures measured with the thermometer within the error bars .

A characterization of the squeezed-light source was performed via balanced homodyne detection. A noise reduction of $(-8.7 \pm 0.2)\,\mathrm{dB}$ below vacuum shot noise was measured at a sideband frequency of 400 kHz with a pump power of 11.8 mW. From the

corresponding antisqueezing factor of $(17.9 \pm 0.2)\,\mathrm{dB}$ followed a detection efficiency $\eta^2 = 0.878 \pm 0.013$. The estimated efficiency considering the known optical losses of the setup was $\eta^2 \approx 0.95$. Because of this discrepancy and as the squeezing decreased for higher pump powers, it is assumed that phase noise degraded the measured squeeze factor.

The squeezed-light source was implemented into the optomechanical experiment and the produced states were injected into the Michelson-Sagnac interferometer through the output port. The squeeze angle was stabilized with feedback control loops using the signal of a bright frequency-shifted control field. At both operating temperatures $T = 293\,\mathrm{K}$ and $T = 100\,\mathrm{K}$, the shot noise of the interferometer output signal was squeezed by $(3.1 \pm 0.2)\,\mathrm{dB}$, which corresponds to a reduction by a factor of $\sqrt{2}$ in the linear displacement spectral density.

In conclusion, the shown results demonstrate a squeezed-light-enhanced optomechanical measurement. After upgrading the setup for the performance at lower temperatures and for a higher input power, the implementation of a signal-recycling mirror will allow the detection of radiation pressure noise over a broad frequency band. Then the application of squeezed states, as successfully executed in the presented work, will reduce the total quantum noise such, that an undercut of the standard quantum limit can be realized. Therefore the presented results form a crucial step to increase the sensitivity of future optomechanical experiments.

10 References

[1] A. Einstein. Über einen die Erzeugung und Verwandlung des Lichtes betreffenden heuristischen Gesichtspunkt. *Annalen der Physik*, 322(6):132–148, 1905. 1

[2] Max Planck. Ueber das Gesetz der Energieverteilung im Normalspectrum. *Annalen der Physik*, 309(3):553–563, 1901. 1, 26

[3] Peter Lebedew. Untersuchungen über die Druckkräfte des Lichtes. *Annalen der Physik*, 311(11):433–458, 1901. 1

[4] Markus Aspelmeyer, Tobias J. Kippenberg, and Florian Marquardt. Cavity optomechanics. *Rev. Mod. Phys.*, 86:1391–1452, dec 2014. 1

[5] Andreas Sawadsky, Klemens Hammerer, and Roman Schnabel. Kühlen von großen Objekten mit Laserlicht. *Physik in unserer Zeit*, 46(4):162–163, 2015. 1

[6] Jasper Chan, T. P. Mayer Alegre, Amir H. Safavi-Naein, Jeff T. Hill, Alex Krause, Simon Gröblacher, Markus Aspelmeyer, and Oskar Painter. Laser cooling of a nanomechanical oscillator into its quantum ground state. *Nature Physics*, 478:89–92, October 2011. 1

[7] W. Heisenberg. Über den anschaulichen Inhalt der quantentheoretischen Kinematik und Mechanik. *Zeitschrift für Physik*, 43(3):172–198, mar 1927. 1, 15

[8] R. Schnabel. Squeezed states of light and their applications in laser interferometers. *Physics Reports*, 684(0370-1573), apr 2017. 1, 7, 14, 15, 19, 24, 26, 30, 37, 49, 54, 129

[9] V. B. Braginskiĭ and A. B. Manukin. Ponderomotive Effects of Electromagnetic Radiation. *Soviet Journal of Experimental and Theoretical Physics*, 25:653, October 1967. 2, 3

[10] Albert Einstein. The Foundation of the General Theory of Relativity. *Annalen Phys.*, 49(7):769–822, 1916. 2

[11] K L Dooley and. Status of GEO 600. *Journal of Physics: Conference Series*, 610:012015, may 2015. 2

[12] LIGO Scientific Collaboration, J. Aasi, B. P. Abbott, R. Abbott, T. Abbott, M. R. Abernathy, K. Ackley, C. Adams, T. Adams, P. Addesso, and et al. Advanced LIGO. *Classical and Quantum Gravity*, 32(7):074001, April 2015. 2, 19

[13] F Acernese, P Amico, M Al-Shourbagy, S Aoudia, S Avino, D Babusci, G Ballardin, F Barone, L Barsotti, M Barsuglia, F Beauville, M A Bizouard, C Boccara, F Bondu, L Bosi, C Bradaschia, S Birindelli, S Braccini, and A Brillet et al. The status of VIRGO. *Classical and Quantum Gravity*, 23(8):S63–S69, mar 2006. 2

[14] P Barriga, D G Blair, D Coward, J Davidson, J-C Dumas, and E Howell et al. AIGO: a southern hemisphere detector for the worldwide array of ground-based interferometric gravitational wave detectors. *Classical and Quantum Gravity*, 27(8):084005, apr 2010. 2

[15] S Dwyer et al. Advanced LIGO status. *Journal of Physics: Conference Series*, 610:012013, may 2015. 2

[16] Gregory M Harry et al. Advanced LIGO: the next generation of gravitational wave detectors. *Classical and Quantum Gravity*, 27(8):084006, apr 2010. 2

[17] Christopher C. Gerry and Peter L. Knight. *Introductory Quantum Opticst*. Cambridge, 2005. 2, 7, 13, 15, 17

[18] R. E. Slusher, L. W. Hollber, B. Yurke, J. C. Mertz, and J. F. Valley. Observation of squeezed states generated by four-wave mixing in an optical cavity. *Phys. Rev. Lett.*, 55, 1985. 2, 37

[19] Henning Vahlbruch, Moritz Mehmet, Karsten Danzmann, and Roman Schnabel. Detection of 15 dB Squeezed States of Light and their Application for the Absolute Calibration of Photoelectric Quantum Efficiency. *Phys. Rev. Lett.*, 117, 2016. 2

[20] Carlton M. Caves. Quantum-mechanical noise in an interferometer. *Phys. Rev. D*, 23:1693–1708, apr 1981. 2

[21] C Affeldt, K Danzmann, K L Dooley, H Grote, M Hewitson, S Hild, J Hough, J Leong, H Lück, M Prijatelj, S Rowan, A Rüdiger, R Schilling, R Schnabel, E Schreiber, B Sorazu, K A Strain, H Vahlbruch, B Willke, W Winkler, and H Wittel. Advanced techniques in GEO 600. *Classical and Quantum Gravity*, 31(22):224002, nov 2014. 3

[22] J. et al Aasi. Enhancing the sensitivity of the LIGO gravitational wave detector by using squeezed states of light. *Nature Photon.*, 7:613–619, 2013. 3

[23] A. Wicht, K. Danzmann, M. Fleischhauer, M. Scully, G. Müller, and R.-H. Rinkleff. White-light cavities, atomic phase coherence, and gravitational wave detectors. *Optics Communications*, 134:431–439, February 1997. 3, 60

[24] V. Peano, H. G. L. Schwefel, Ch. Marquardt, and F. Marquardt. Intracavity squeezing can enhance quantum-limited optomechanical position detection through deamplification. *Phys. Rev. Lett.*, 115:243603, dec 2015. 3, 4, 59, 60, 129

[25] T. Corbitt, D. Ottaway, E. Innerhofer, J. Pelc, and N. Mavalvala. Temporal Beehavior of Radiation-Pressure-Induced Vibrations of an Optical Microcavity Phonon Mode. *Phys. Rev. Lett*, 94(3), 2005. 3, 19

[26] C. H. Metzger and K. Karrai. Cavity Cooling of a mirolever. *Nature Physics*, 432(3), 2004. 3, 19

[27] Min Jet Yap et al. Broadband reduction of quantum radiation pressure noise via squeezed light injection. *arXiv*, 2018. 3, 19

[28] T P Purdy, R W Peterson, P-L Yu, and C A Regal. Cavity optomechanics with Si3N4membranes at cryogenic temperatures. *New Journal of Physics*, 14(11):115021, nov 2012. 3, 19

[29] H. Kaufer, A. Sawadsky, T. Westphal, D. Friedrich, and R. Schnabel. Tomographic readout of an opto-mechanical interferometer. *New Journal of Physics*, 14(095018), 2012. 3, 19, 22

[30] A. Sawadsky, H. Kaufer, R .Moghadas Nia, S. P. Tarabrin, F. Y. Khalili, K. Hammerer, and R. Schnabel. Observation of generalized optomechanical coupling and cooling on cavity resonance. *Phys. Rev. Lett.*, 114(043601), jan 2015. 3, 19, 22, 126

[31] Kazuhiro Yamamoto, Daniel Friedrich, Tobias Westphal, Stefan Goßler, Karsten Danzmann, and Roman Schnabel. Quantum noise of a Michelson-Sagnac interferometer with translucent mechanical oscillator. *Physical Review A*, 81, 2010. 3, 19, 27, 126, 128, 130

[32] Bei-Bei Li, Jan Bílek, Ulrich B. Hoff, Lars S. Madsen, Stefan Forstner, Varun Prakash, Clemens Schäfermeier, Tobias Gehring, Warwick P. Bowen, and Ulrik L.

Andersen. Quantum enhanced optomechanical magnetometry. *Optica*, 5(7):850–856, Jul 2018. 4

[33] M. Korobko, L. Kleybolte, S. Ast, H. Miao, Y. Chen, and R. Schnabel. Beating the standard sensitivity-bandwidth limit of cavity-enhanced interferometers with internal squeezed-light generation. *Phys. Rev. Lett.*, 118, apr 2017. 4, 59, 63, 64, 65, 129

[34] Andreas Sawadsky. *Optomechanical Coupling in an Interferometer with a SiN-Membrane*. PhD thesis, Albert Einstein Institut, Hannover, 2017. 7, 19, 67, 69, 71, 72, 78, 105, 122, 128

[35] Henning Kaufer. *Opto-mechanics in a Michelson-Sagnac interferometer*. PhD thesis, Albert Einstein Institut, Hannover, 2013. 7, 8, 19, 23, 34, 35, 125, 126, 128

[36] Peter R. Saulson. *Fundamentals of Interferometric Gravitational Wave Detectors*. World Scientific, 2nd edition edition, 2017. 9, 26, 31

[37] Peter R. Saulson. Thermal noise in mechanical experiments. *Phys. Rev. D*, 42:2437–2445, oct 1990. 9, 10

[38] Lisa Kleybolte. Eine doppelt-resonante Quetschlichtquelle für optomechanische Experimente bei 1550 nm. Master's thesis, Leibniz Universität Hannover, 2016. 13, 37, 38, 45, 55, 56, 67, 108, 110

[39] Henning Vahlbruch. *Squeezed Light for Gravitational Wave Astronomy*. PhD thesis, Albert Einstein Institut, Hannover, 2008. 13, 37, 51, 52, 54, 67, 86

[40] Carlton M. Caves and Bonny L. Schumaker. New formalism for two-photon quantum optics. I. Quadrature phases and squeezed states. *Phys. Rev. A*, 31, 1885. 14, 60

[41] Hans A Bachor and Timothy C Ralph. *A Guide to Experiments in Quantum Optics*. Vieweg Teubner, 2 edition, 2008. 15

[42] Aleksandr Khalaidovski. Beyond the Quantum Limit - A Squeezed-Light Laser in GEO600. Master's thesis, Albert Einstein Institut, Hannover, 2011. 19, 37

[43] T. Corbitt, D. Ottaway, E. Innerhofer, J. Pelc, and N. Mavalvala. Measurement of Radiation-Pressure-Induced optomechanical dynamics in a suspended Fabry-Perot cavity. *Phys. Rev. A*, 74(3), 2006. 19

[44] Tobias Westphal. Opto-mechanische Kopplung in einem Michelson-Sagnac Interferometer. Master's thesis, Leibniz Universität Hannover, 2009. 19, 21, 67

[45] Yoshitomo Okawachi Kevin Luke, Michael R. E. Lamont, Alexander L. Gaeta, and Michal Lipson. Broadband mid-infrared frequency comb generation in a si3n4 microresonator. *Optics Letters*, 40(21), 2015. 20

[46] Website. www.norcada.com. 19, 21

[47] B.M. Zwickl, W.E. Shanks, A.M. Jayich, A.C. Bleszynski Jayich C. Yang, J.D. Thompson, and J.G.E. Harris. High quality mechanical and optical properties of commercial silicon nitride membranes. *Applied Physics Letters*, 92(103125), 2008. 19

[48] J. D. Thompson, B. M. Zwickl, A. M. Jayich, Florian Marquardt, S. M. Girvin, and J. G. E. Harris. Strong dispersive coupling of a high-finesse cavity to a micromechanical membrane. *Nature Physics*, 452(72), 2008. 19

[49] A M Jayich, J C Sankey, B M Zwickl, C Yang, J D Thompson, S M Girvin, A A Clerk, F Marquardt, and J G E Harris. Strong dispersive coupling of a high-finesse cavity to a micromechanical membrane. *New Journal of Physics*, 10, 2008. 19

[50] M. Karuza, C. Biancofiore, C. Molinelli M. Bawaj, M. Galassi, R. Natali, P. Tombesi, G. Di Giuseppe, and D. Vitali. Optomechanically induced transparency in a membrane-in-the-middle setup at room temperature. *Phys. Rev. A*, 88, 2013. 19

[51] Daniel Friedrich. *Laser interferometry with coating-free mirrors.* PhD thesis, Albert Einstein Institut, Hannover, 2011. 19

[52] D Friedrich, H Kaufer, T Westphal, K Yamamoto, F Ya Khalili A Sawadsky, S L Danilishin, S Goßler, K Danzmann, and R Schnabel. Laser interferometry with translucent and absorbing mechanical oscillators. *New Journal of Physics*, 13, 2011. 19

[53] M. Born and E. Wolf. *Principles of Optics: Electromagnetic Theory of Propagatin, Interference and Diffraction of Light.* Springer, 2 edition, 1964. 19

[54] Robert Huszank, László Csedreki, Zsófia Kertész, and Zsófia Török. Determination of the density of silicon–nitride thin films by ion-beam analytical techniques

(rbs, pixe, stim). *Journal of Radioanalytical and Nuclear Chemistry*, 307(1):341–346, jan 2016. 21, 105

[55] A. Zeilinger. General properties of lossless beam splitters in interferometry. *American Journal of Physics*, 49(882), 1981. 23

[56] I.N. Bronstein und K. A. Semendjajew. *Taschenbuch der Mathematik*. Harri, 29 edition, 2000. 23

[57] W. A. Edelstein, J. Hough, J. R. Pugh, and W. Martin. Limits to the measurement of displacement in an interferometric gravitational radiation detector. *Journal of Physics E - Scientific Instruments*, 11, 1978. 26

[58] V. Branginsky and S. Vyatchanin. Frequency fluctuations of nonlinear origin in self-sustained optical oscillators. *Physics Letters A*, 279(154), 2001. 31

[59] D R. M. Crooks, Cagnoli Gianpietro, M.M. Fejer, A M. Gretarsson, Gregory Harry, James Hough, N Nakagawa, S.D. Penn, R Route, S Rowan, and Peter Sneddon. Experimental measurements of coating mechanical loss factors. *Classical and Quantum Gravity*, 21, 02 2004. 31

[60] Yong-qing Li, Dorel Guzun, and Min Xiao. Sub-shot-noise-limited optical heterodyne detection using an amplitude-squeezed local oscillator. *Phys. Rev. Lett.*, 82:5225–5228, 1999. 31

[61] H. Nyquist. Thermal Agitation Of Electric Charge in Conductors. *Phys. Rev.*, 32, 1928. 31

[62] Philipp Christoph. *Feedback-assisted sympathetic cooling in a hybrid atomic-mechanical system*. PhD thesis, Universität Hamburg, 2018. 32

[63] Sebastian Steinlechner. *Quantum Metrology with Squeezed and Entangled Light for the Detection of Gravitational Waves*. PhD thesis, Albert Einstein Institut, Hannover, 2013. 37

[64] R. M. Shelby, M. D. Levenson, D. F. Walls, A. Aspect, and G. J. Milburn. Generation of squeezed states of light with a fiber-optic ring interferometer. *Phys. Rev. A*, 33, 1986. 37

[65] Ling-An Wu, H. J. Kimble, J. L. Hall, and Huifa Wu. Generation of Squeezed States by Parametric Down Conversion. *Phys. Rev. Lett.*, 57, 1986. 37

[66] Jöran Bauchrowitz, Tobias Westphal, and Roman Schnabel. A graphical description of optical parametric generation of squeezed states of light. *American Journal of Physics*, 81(10):767–771, 2013. 37, 39, 40

[67] Axel Schönbeck. *Compact squeezed-light source at 1550 nm.* PhD thesis, Universität Hamburg, 2018. 37, 38, 54, 67

[68] R. Boyd. *Nonlinear Optics.* Acamdemic Press, 2008. 37, 44

[69] Henning Vahlbruch. Gequetschtes Licht bei kleinen Seitenbandfrequenzen. Master's thesis, Albert Einstein Institut, Hannover, jan 2004. 41

[70] Ramon MoghadasNia. Highly efficient frequency doubling of 1550 nm laser light. Bachelor thesis, oct 2010. 41, 69

[71] Aiko Samblowski. *State Preparation for Quantum Information Science and Metrology.* PhD thesis, Albert Einstein Institut, Hannover, aug 2012. 47

[72] Henning Vahlbruch, Simon Chelkowski, Boris Hage, Alexander Franzen, Karsten Danzmann, and Roman Schnabel. Coherent control of vacuum squeezing in the gravitational-wave detection band. *Phys. Rev. Lett.*, 97:011101, jul 2006. 52

[73] Walls and Milburn. *Quantum Optics.* Springer, 1 edition, 2008. 54

[74] Moritz Mehmet, Stefan Ast, Tobias Eberle, Sebastian Steinlechner, Henning Vahlbruch, and Roman Schnabel. Squeezed light at 1550 nm with a quantum noise reduction of 12.3 dB. *Opt. Express*, 19(25):25763–25772, Dec 2011. 55

[75] Drever R. W. P., Hall J.L., Kowalski F.V., Hough J, Ford G.M., Munley A. J., and Ward H. Laser Phase and Frequency Stailization Using an Opical Resonator. *Applied Physics*, 31, 1983. 57, 61

[76] Jun Mizuno. *Comparison of optical configurations for laser-interferometric gravitational-wave detectors.* PhD thesis, Albert Einstein Institut, Hannover, 1995. 59

[77] A. A. Clerk, M. H. Devoret, S. M. Girvin, Florian Marquardt, and R. J. Schoelkopf. Introduction to quantum noise, measurement, and amplification. *Rev. Mod. Phys.*, 82, apr 2010. 59

[78] The LIGO Scientific Cooperation. A gravitational wave observatory operating beyond the quantum shot-noise limit. *Nature Physics*, 7, 2011. 60

[79] Stefan Ast. *New approaches in squeezed light generation - Quantum states of light with GHz squeezing bandwidth and squeezed light generation via the cascaded Kerr effect*. PhD thesis, Albert Einstein Institut, Hannover, 2015. 63

[80] Jessica Steinlechner, Stefan Ast, Christoph Krüger, Amrit Pal Singh, Tobias Eberle, Vitus Händchen, and Roman Schnabel. Absorption Measurements of Periodically Poled Potassium Titanyl Phosphate (PPKTP) at 775 nm and 1550 nm. *Sensors (Basel)*, 13(565-573), 2014. 64

[81] Pascal Gewecke. Optimierung eines Michelson-Sagnac-Interferometers für die Anwendung von gequetschtem Licht. Master's thesis, Universität Hamburg, 2019. 67, 122

[82] Jack W. Ekin. *Experimental techniques for low-temperature measurements*. Oxford University press, 1 edition, 2006. 68

[83] Website. www.attocube.com. 70, 124

[84] Website. www.janssenprecisionengineering.com. 70, 124

[85] Morten Steinecke. Entwurf und Aufbau eines monolithischen MichelsonSagnac-Interferometers. Bachelor thesis, 2014. 71

[86] X. Jin, J. Su, Y. Zheng, C. Chen, W. Wang, and K. Peng. Balanced homodyne detection with high common mode rejection ratio based on parameter compensation of two arbitrary photodiodes. *Optics Express*, 23:23859, September 2015. 83

[87] Keysight Technologies. *Spectrum Analysis Basics - Appplication note 150*. www.Keysight.com, 2005. 98, 102

[88] Tobias Wagner. Homodyne Detection of a Nanomechanical Oscillator for Thermometry and Active Feedback Cooling. Master's thesis, Universität Hamburg, 2016. 100, 123, 124

[89] Ting Hong, Huan Yang, Eric K. Gustafson, Rana X. Adhikari, and Yanbei Chen. Brownian thermal noise in multilayer coated mirrors. *Phys. Rev. D*, 87:082001, apr 2013. 102

[90] Mingyun Yuan, Martijn A. Cohen, and Gary A. Steele. Silicon nitride membrane resonators at millikelvin temperatures with quality factors exceeding 108. *Applied Physics Letters*, 107(26):263501, 2015. 105

[91] Website. www.heraeus.com. 110

[92] Fan Yang, Felix Rochau, Jana S. Huber, Alexandre Brieussel, Gianluca Rastelli, Eva M. Weig, and Elke Scheer. Spatial modulation of nonlinear flexural vibrations of membrane resonators. *Phys. Rev. Lett.*, 122:154301, apr 2019. 124

[93] P. Kwee. *Laser Charaterization and Stabilization for Precision Interferometry.* PhD thesis, Leibniz Universität Hannover, 2010. 125

[94] B. J. Meers. Recycling in Laser Interferometric Gravitational Wave Detectors. *Phys. Rev.*, D38:2317–2326, 1988. 126

11 Eidesstattliche Versicherung / Declaration on oath

Hiermit versichere ich an Eides statt, die vorliegende Dissertationsschrift selbst verfasst und keine anderen als die angegebenen Hilfsmittel und Quellen benutzt zu haben. Die eingereichte schriftliche Fassung entspricht der auf dem elektronischen Speichermedium. Die Dissertation wurde in der vorgelegten oder einer ähnlichen Form nicht schon einmal in einem früheren Promotionsverfahren angenommen oder als ungenügend beurteilt.

Hamburg, 23.08.2019

Unterschrift

12 Ackknowledgements

First of all I thank Prof. Dr. Roman Schnabel for inviting me to join his group and thus giving me the opportunity to research in such an interesting unique field, for being a helpful encouraging supervisor and for sharing his knowledge and ideas.

I could not have achieved the presented results without the previous work that has been done on this experiment. I thank Henning, Andreas and the *Optoboys* Ramon, Sacha, Mikhail and Paolo for working with me, letting me learn from them and for all the fun times, we had in and outside the laboratory. I was lucky to work in such a friendly environment beginning with the AEI in Hannover with the good old mensa crew with Steffen, Axel, Amrit, Stefan, Melanie, Vaishaly, Oliver and Katharina and then in the ILP in Hamburg with old and new collegues. Jascha, Jan G. and Jan P., What would I have done without you having an open ear when I struggled, taking your time to help me during the writing process and supplying me with coffee!

Especially I want to thank Pascal Gewecke for joining the SquMSI team, when I needed a helping hand the most, for motivating me and for encouraging me after every setback.

A special shoutout goes to all my friends who supported me through ups and downs and believed in me. You distracted me when I needed it with laughter, dances and fun trips.

Last but not least I could not be more grateful for my awesome family for accepting my moods and my busy life, for being there for me and for helping with my move to Hamburg.